# SOIL RESISTANCE AND DEFLECTION ANALYSIS OF CYCLIC LATERALLY LOADED OFFSHORE WELL CONDUCTORS FOR FATIGUE EVALUATIONS

A Dissertation

by

OLUSOLA AYANDIRE KOMOLAFE

Submitted to the Office of Graduate and Professional Studies of
Texas A&M University
in partial fulfillment of the requirements for the degree of

DOCTOR OF PHILOSOPHY

| | |
|---|---|
| Chair of Committee, | Charles Aubeny |
| Committee Members, | Jerome Schubert |
| | Marcelo Sanchez |
| | Zenon Medina-Cetina |
| Head of Department, | Robin Autenrieth |

December 2019

Major Subject: Civil Engineering

# ABSTRACT

Offshore conductors are an integral part of the oil and gas well and they support the motions from the riser, which are usually subjected to environmental loads. These structures are designed to meet requirements for Ultimate Limit States (ULS), Serviceability Limit States (SLS), and Fatigue Limit States (FLS), design conditions. This ensures that if the foundation experiences cyclic loads, during its project span, it can withstand the fatigue damage that accumulates without failure. Fatigue failure in offshore structural components, can result from accumulation of fatigue stresses, with magnitudes considerably below the ultimate design stresses. Improved accuracy in characterizating the cyclic lateral soil response is critical in fatigue assessment of well conductors and piles subjected to dynamic fatigue loads.

In this study, a phenomenological and bounding surface plasticity cyclic P-y model was discussed. Key features of the models include nonlinear load-displacement behavior with stiffness degradation during cyclic loading. These models provide full description of soil resistance during lateral loading, including an initial short-excursion monotonic loading stage, a transient stage of progressive degradation in stiffness from the first excursion, and a steady-state stage involving minimal changes in soil stiffness after a large number of load cycles. The model input parameters were obtained from calibrations to data derived from centrifuge tests on model conductors subjected to harmonic lateral loads. These models are able to simulate random load sequences which is useful in fatigue analysis. Fatigue damage in well conductors and piles arises from changes in axial and bending stresses, with the latter being more dependent on lateral soil response.

These models are evaluated based on their ability to accurately predict bending moments when the spring model is used in conjunction with a laterally loaded soil-structure interaction

model. These models successfully predict the maximum change in cyclic bending moment (change in moment during a load reversal) and the location of the maximum cyclic moment along the conductor depth approximately within a 20% range. This range is evaluated by comparing the model computations/predictions to the test data from the centrifuge program and validated within the test displacement range up to 0.15D (15 % pile diameter). The current form of the presented models do not consider consolidation effects, which may significantly affect long-term loading predictions used in fatigue life assessments.

# DEDICATION

Dedicate this is to my unborn children, to inspire them to pursue their dreams and goals to the fullest. May you achieve excellence and great heights in all you do, with the drive to make this world better than you met it.

# ACKNOWLEDGEMENTS

My enormous gratitude goes to my committee chair, Dr. Charles Aubeny for his unrelenting support, guidance, mentorship, and encouragement throughout the course of this research, and program. Most especially grateful for you giving me my room and window to grow.

My committee members, Dr. Jerome Schubert, Dr. Zenon Medina-Cetina, and Dr. Marcelo Sanchez, I am deeply grateful for all your guidance, time, expert opinions, and support throughout the course of my program.

I will love to thank Dr. Edward Clukey and Dr. Arash Zakeri for their contributions and support during the course of this research. I am truly grateful.

Thank you my colleagues, friends, and the department faculty and staff especially Laura and Chris for making my time at Texas A&M University a memorable experience.

Special thanks to my beloved Father and beloved Mother, Mr and Mrs Ilupeju; my beloved brother Adedayo; my beloved aunt Christine; my beloved cousin Comfort, and all my friends who encouraged me at different times during the course of this journey. Thank you all for your encouragement, kind thoughts, well wishes/prayers, calls, messages, and all that kept me going during tough times.

Finally, to my beloved husband and best friend, Olatunbosun (the Bos in our precious #SolieBos), I say thank you for your prayers, patience, love, and encouragement.

## CONTRIBUTORS AND FUNDING SOURCES

This work was supported by dissertation committee consisting of Professor Charles Aubeny [advisor], Professor Zenon Medina-Cetina, Professor Marcelo Sanchez, and Professor Jerome Schubert, and supervised by dissertation committee chair Professor Aubeny.

The data analyzed for Chapter V was provided by BP America Inc., with contributions from Arash Zakeri.

All other work conducted for the dissertation was completed by the student independently, with guidance and mentoring from committee chair, and improved with feedback from commitee.

Graduate study was supported by Teaching Assistantship from Civil Engineering department, Texas A&M University; Research Assistantship funded by Bp America Inc., and National Science Foundation (NSF); Endowment fellowship from Terracon through Texas A&M University; Texas Grant through Texas A&M University; Personal funds; a scholarship from the McCain Family Aggie Veteran Honor Scholarship.

TABLE OF CONTENTS

Page

LIST OF FIGURES

Page

LIST OF TABLES

Page

# CHAPTER I

# INTRODUCTION

## Energy History

An essential part of existence is energy. It is required for grand tasks (e.g. offshore platform operations, automobile running, space travel), as well as everyday activities (cooking, powering bulbs). Dating back to 2000 BC, energy generation, was provided through various sources, from animals, burning woods, coal, and so on. As energy demands increased with needs from growing population, by the 1800s, sources for energy generation, extended to crude oil exploration, dams, and nuclear plants. The future will likely tend towards clean energy generation methods in addition to existing sources of energy production. Figure 1.1 shows global energy consumption across major sources from 1990 to 2015, showing changes over this period, equally providing insights of what the future energy sources could be.

Energy produced from fossil fuels still remains the main source of meeting the global power demands of this age. Depletion of these resources with use, coupled with continuous increase in energy demands, continuously pushes the limit of exploration of oil and gas to deeper offshore environments which still houses great oil and gas reserves. However, these offshore environments present harsh environmental conditions, requiring the improvement of the current body of knowledge. This is essential not just for improving design practices and narrowing the streams of uncertainties, but also in proffering optimized design solutions, with optimized economic value.

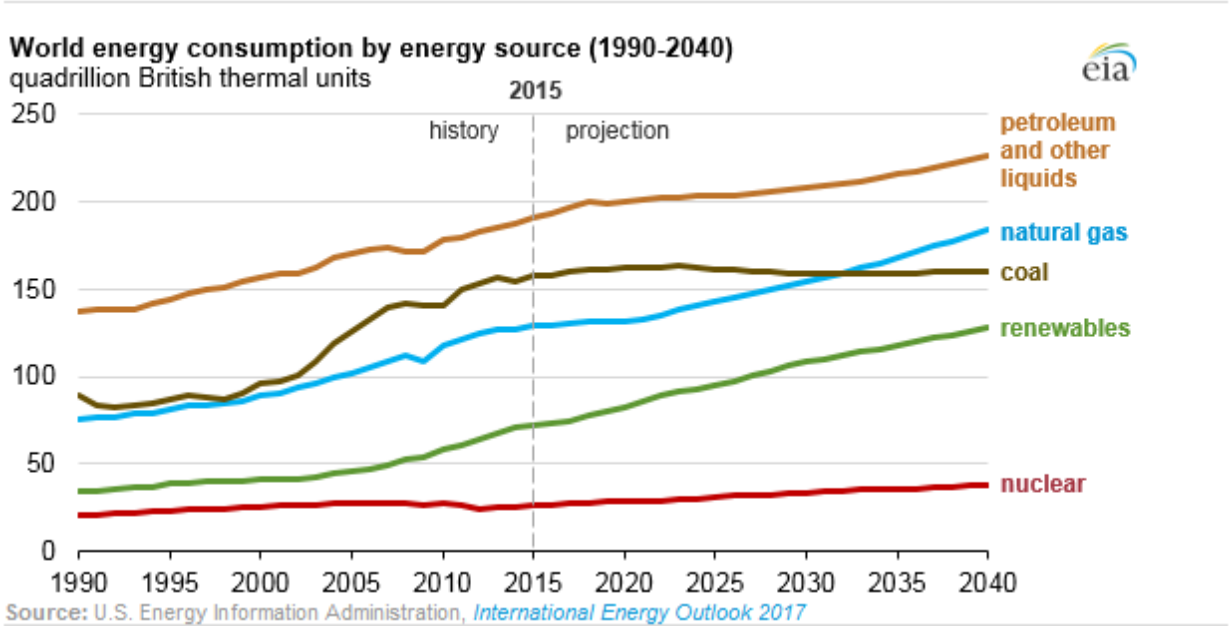


**Figure 1. 1: World energy consumption across major energy sources from 1990 to 2015, with futuristic projections (reprinted from https://www.eia.gov/todayinenergy/detail.php?id=32912).**

Offshore Field and Structures

Offshore structures are generally classified as bottom supported fixed structures or floating structures as depicted in Figure 1.2. Currently, the term offshore structures extends beyond the scope of the oil and gas industries, to renewable energy industries, such as offshore wind farms, tidal and current energy harnessing projects, with possibilities for more innovation. Figure 1.3 shows the various offshore wind turbines structures in varying water depths. These offshore structures are capital intensive and need to survive through severe environmental conditions. Use of these structures for oil and gas applications, is currently the only lucrative purpose that pays for its out-sized cost and complicated engineering (Newcomb, 2017). The quest to meet the world's increasing energy demand pushes the location of these offshore structures, into deeper and ultra-

deep waters, where more oil reserves or stronger wind loads occur. Additionally, the life of some existing projects may require extension, especially where new oil wells need to be tied to existing structures or continue well production is required beyond the design life of the structure. Improving the body of knowledge will help optimize the solutions proffered to engineering design challenges, which provides us with safe, yet economical structures.

In 2008, oil prices increased worldwide which led to commencement of many offshore projects (El-Reedy, 2012). However, in 2014, a downturn in market prices of crude oil across the globe, sparked increased interests in alternative energy sources. This has facilitated innovative ideas for delving into alternate energy generation avenues, of which the offshore farm, is receiving increased attention. In 2015, construction of the first U.S. commercial offshore wind farm off Block Island (Rhode Island) commenced, and was fully operational in May 2017. It delivers power to an island off the coast of Rhode Island. There are projections, for significant future development of offshore windfarms.

Every offshore structure requires support from foundations. These foundations are the crucial supports that eventually bear all the loads the offshore structures are subjected to, hence their importance. These transmitted loads to the foundations, are ultimately supported by the soils surrounding the foundation. The focal point of this study is the offshore well conductor, which is the topmost and largest casing in oil and gas wells.

## Offshore Environmental Loads

Offshore structures are subjected to static and dynamic loads. Loads considered as static loads, acting on these structures includes, gravity loads, deck loads, hydrostatic loads, and currents. The dynamic loads are either caused by nature and/or man-made vibrations; examples include

earthquakes, winds, waves, machines, human traffic and blasts. Loads on the structures caused by environmental phenomena such as wind, waves, current, tides, earthquakes, temperature, ice, sea bed movement, and marine growth, are referred to as Environmental loads. All these loads are ultimately transmitted to the foundation. The response of the offshore structures to motions during the structure's lifespan, could vary significantly. Some motions such as the small amplitude vibrations cause the soil to behave practically as an elastic material. Whereas, large motions acting on foundations (conductor or piles), result in the soil behavior being nonlinear. The offshore well conductors generally experience three (3) categories of loads that could induce fatigue damage. These are loads transmitted from Vessel motions, Hull Vortex Induced Motion (VIM), and Riser Vortex Induced Vibration (VIV). The Vessel motion is the effect of the vessel or platform's response to wind and wave loads. The Hull Vortex Induced Motion and the Riser Vortex Induced Vibration, are responses of the Hull and Riser respectively to ocean currents. In a study case stated in Jeanjean (2009) the Vessel motions, Hull VIM and Riser VIV caused 20%, 32%, and 48% respectively of the total fatigue damage.

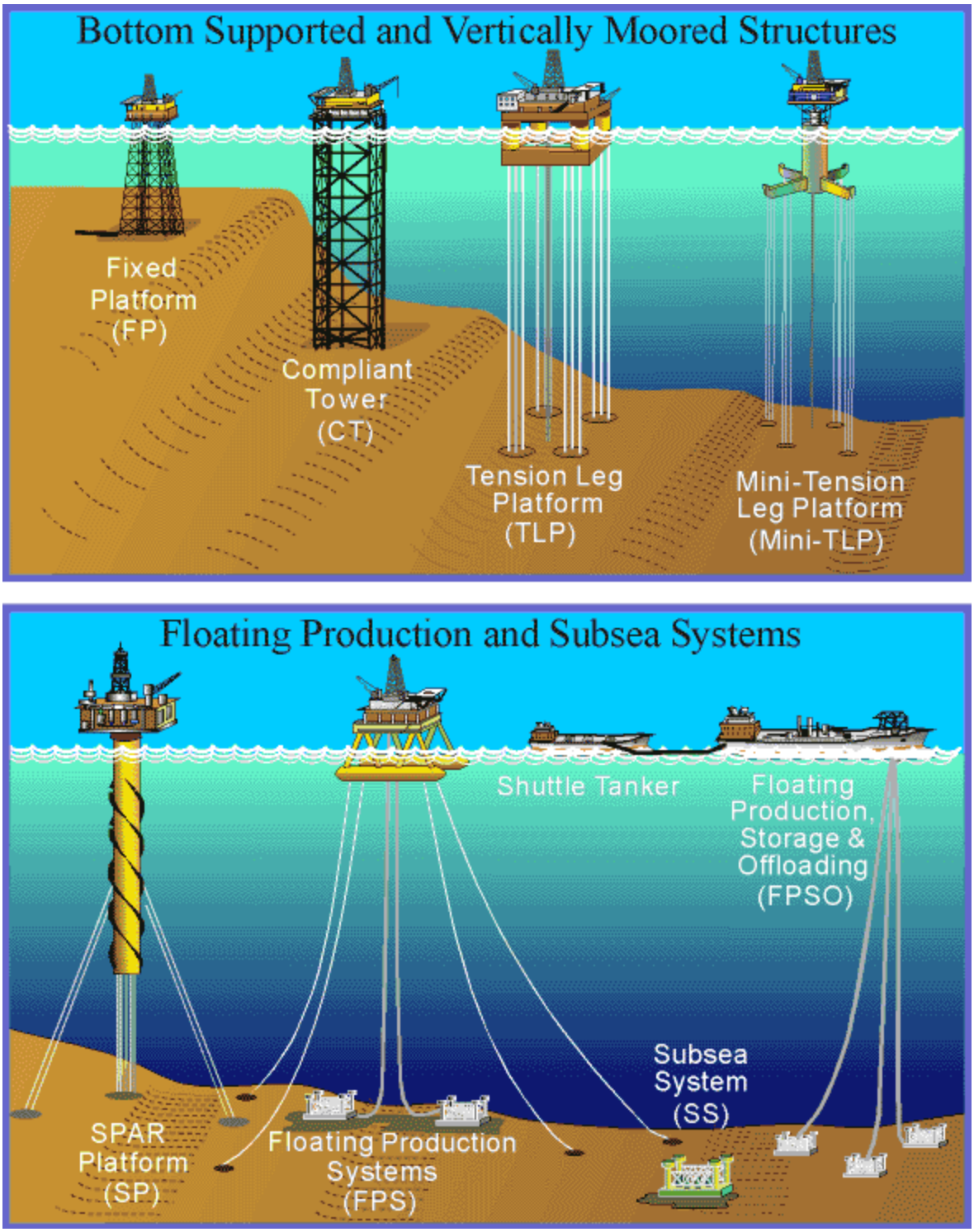


**Figure 1. 2: Different types of oil and gas offshore structures (reprinted from https://www.bsee.gov/site-page/deepwater-development-systems-in-the-gulf-of-mexico-basic-options).**

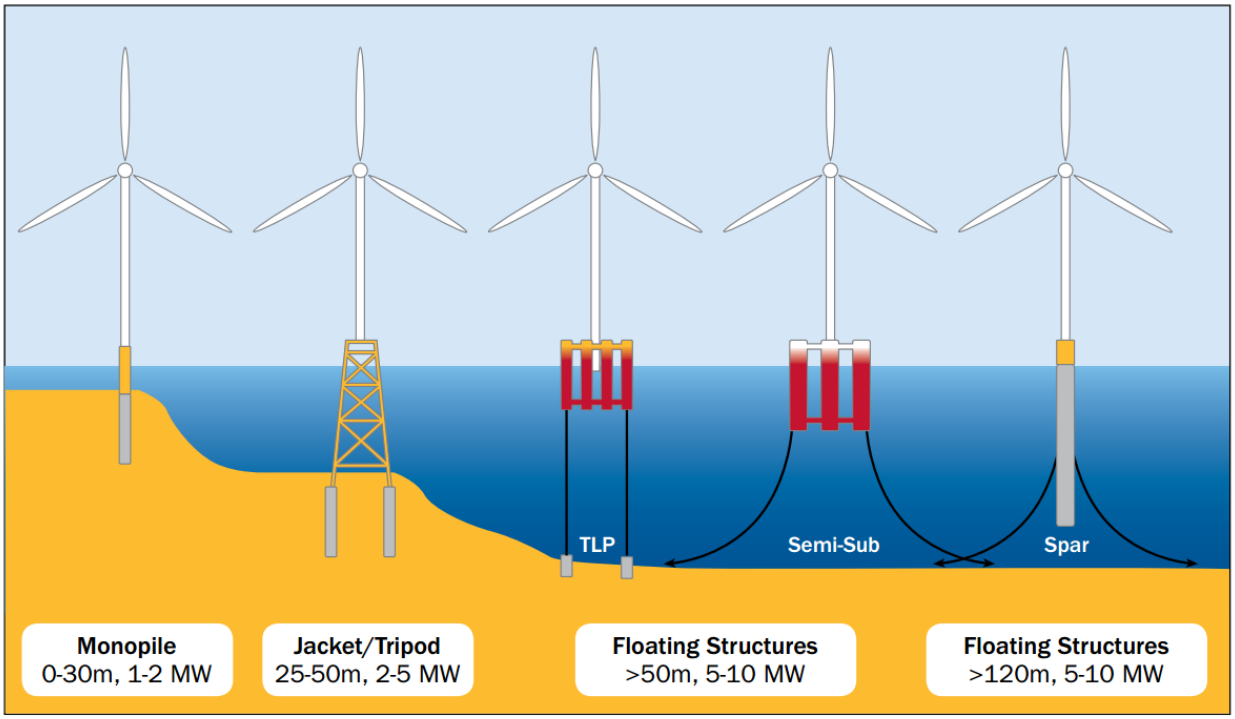


**Figure 1. 3: Different types of offshore windmill structures (reprinted from http://www.ewea.org/fileadmin/files/library/publications/reports/Deep_Water.pdf).**

Offshore Foundations

Piles are typically the common type of offshore foundations employed for supporting offshore structures which include offshore platforms, and wind turbines. They are usually tubular, open-ended and driven. Anchor systems are another type of offshore foundations used to moor buoyant structures. Anchors are divided into two types; gravity anchors or embedded anchors (anchor pile, suction caisson, drag anchor, vertically loaded anchor, and so on). Pile foundations are used extensively to support heavy loads. Another structural foundation which supports the wellhead, is the offshore conductor, the main subject in this study.

Design of offshore foundations generally follow recommendations from various standards, and recommended practice documents, developed by the American Petroleum Institute, Det Norske Veritas (DNV), British Standards, and International Society of Standardization (ISO).

Offshore foundations (conductors and piles) should generally be designed to meet requirements for Ultimate Limit States (ULS), Serviceability Limit States (SLS), and Fatigue Limit States (FLS). These foundations need to be designed to withstand extreme event, and cyclic or seismic loads, if they ever experience such. They should also be designed to accommodate the fatigue damage that accumulates in the foundation, limiting transmission to structures they support without failure (ascertain that FLS design criteria is adequate). Finite Element (FE) solutions are great tools for simulating foundation problems, however, they can be time consuming especially in solving multifaceted complex problems. Some projects are fast paced and for economic reasons, it might be practical to have approximate or simplified analytical or numerical solutions that yields reliable results within a short time. This imperative has spurred the development and implementation of empirical solutions in practice. Nevertheless, one must bear in mind that a significant limitation of empirical solutions is that they are highly dependent on the conditions from which they were generated. Stevens and Audibert (1979) reinforced the idea of scale effects being an important consideration when using empirical methods in geotechnical engineering. For testing purposes, the centrifuge has become a highly appealing tool due to its ability to simulate stress conditions of a prototype in a scaled model test, rendering it a tool of immense utility in geotechnical research and practice. General information on Centrifuge modelling and scaling techniques can be retrieved from the literature (e.g. Schofield, 1980). Details of the centrifuge model test in this research program is in Chapter IV.

Offshore Conductor

The conductor is the topmost, outermost, and largest casing in the well. It is a long tubular steel pipe, which conveys fluids and produced hydrocarbons from the wells, through the risers to the vessels or platforms; prevents environmental contamination, and supports the well assembly. It is the key structural foundation for the subsea wellhead. It supports the wellhead, helping resist and support motions imparted on the wellhead through the riser. It mainly supports lateral loads, because the imparted vertical load is negligible in comparison to the horizontal (lateral) loads. This makes the study of conductors similar to foundations of the offshore wind turbines which bears significant lateral and moment loads. Figure 1.4 shows a view of the well system connected to the platform through a riser, with inserts showing the wellhead and the conductor.

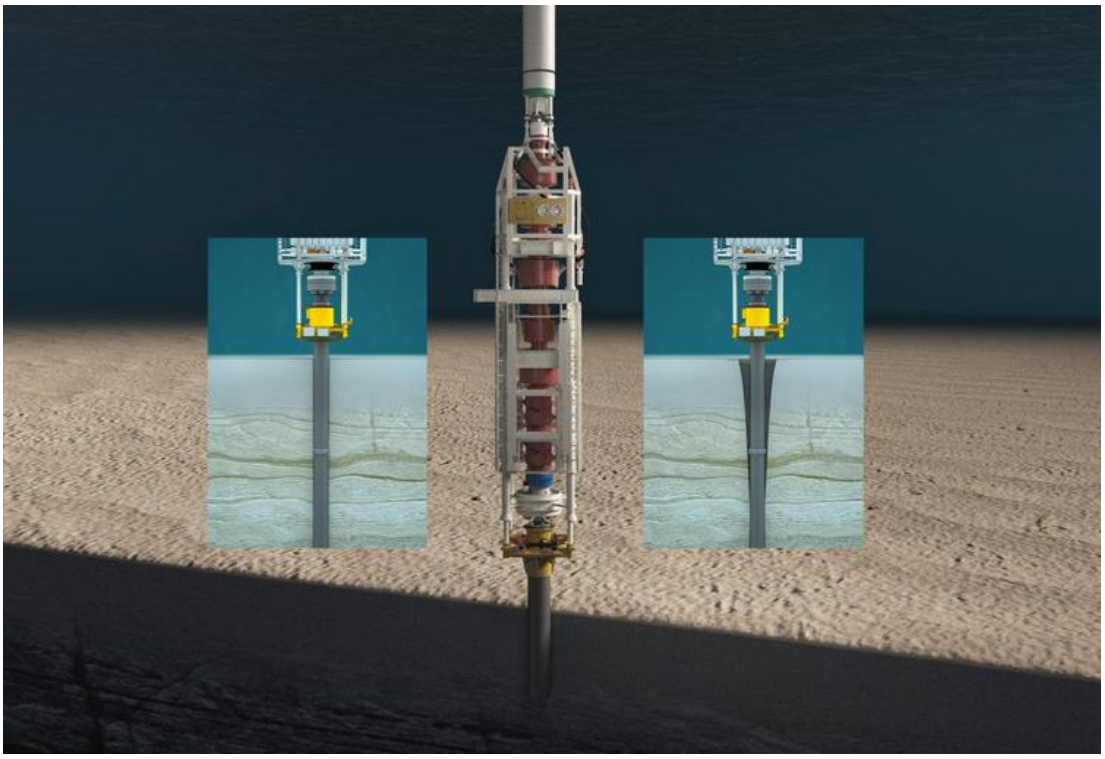

**Figure 1. 4: A view of the offshore wellhead showing the conductor below (reprinted from https://www.4subsea.com/solutions/well-drilling-and-intervention/conductor-analysis/).**

# CHAPTER II

# BACKGROUND AND LITERATURE REVIEW

Complex soil-structure interactions, are mostly modelled with linear and non-linear springs, generally referred to as the Winkler springs. Having structural Winkler springs placed in the three orthogonal directions has provided a practical solution for modeling soil response in soil-structure interaction analysis. It also reduces computational time and costs of numerical simulations. These Winkler springs (soil springs) are represented by P-y curves, which gives the relationship between soil resistance (P), and the soil displacement (y), when a pile/conductor pushes into the soil. Soil response modelling plays a significant role in structural integrity analysis. An appropriate soil response model is one with which both the absolute magnitudes of stress and changes in stresses can be accurately predicted in the structure. A *P-y* approach needs to be carefully selected based on the purpose of the analysis. Present engineering practice typically involves using the *P-y* curves recommended by the American Petroleum Institute (API) (API, 2011) for simulating soil-conductor interaction under fatigue events. These *P-y* methods were developed for ULS and SLS design of piled foundations for steel jackets subjected to monotonic and cyclic storm or hurricane loading and not for FLS assessment. The API recommended *P-y* curves are therefore not fully applicable to a wider range of offshore engineering problems. For instance, in the case of steel catenary risers (SCRs) the complexity of riser-soil interaction has required development of sophisticated soil response models such as the *P-y* formulation described by Aubeny and Biscontin (2009).

P-y Curves

McClelland and Focht (1958) proposed the first P-y method for analysis of laterally loaded piles which was further developed by Matlock and Reese (1962). Different *P-y* formulations have been proposed in the literature, some of which have been included in industry standards. API (2011) recommended *P-y* curves for monotonic and cyclically loaded piles in soft clay based on the work of Matlock (1970). Typically, the API standard presents P-y curves for soil types classified as Soft Clay, Stiff Clay, and Sand. Matlock (1970) presented the groundwork for the construction of P-y curves for Soft Clay; Reese, Cox, and Koop (1975), presented that for Stiff Clay with criteria for clay layer above or below the water table; finally, Neill and Murchinson (1983) presented evaluation of P-y relationships in sands. The present study is motivated by the following issues associated with these recommendations:

- Jeanjean (2009) demonstrated that monotonic "backbone" curve in the API model underestimates the soil response both in terms of the initial stiffness and the ultimate resistance.
- The API model of cyclic behavior presumes that after about 100 load cycles a steady-state, degraded *P-y* curve develops which is independent of the magnitude of cyclic displacement $\Delta y_{cyc}$. This is in contrast to data presented in this study indicating that both the rate of degradation to a steady-state condition and the characteristics of the steady-state *P-y* curve depend on $\Delta y_{cyc}$.
- The API recommendations for cyclic loading were largely intended for relatively large amplitude storm loading, as opposed to fatigue life assessment, which typically involve displacements less than 5% of the pile diameter. Studies by Zakeri et al. (2015, 2016a, 2016b) performed specifically for fatigue evaluation of well conductors indicate the

unload-reload stiffness under cyclic loading to be consistently greater than the stiffness estimated from the backbone curve (e.g. the backbone tangent stiffness). Jeanjean et al (2015) further concluded that the use of softer *P-y* curves in system fatigue analysis does not necessarily result in a conservative analysis.

- The cyclically degraded API *P-y* curve is essentially a truncated version of the monotonic model, where progressively increasing levels of post-peak softening are introduced with increasing proximity to the free surface. The studies by Zakeri et al. (2015, 2016a, 2016b) and data to be presented in this dissertation demonstrate that the unload-reload *P-y* loops do not conform to the shape of the API recommended curves, and the more recent data indicate generally stiffer soil response than that predicted by API curves.
- The API model provides no guidance for the transient stage of degradation of the *P-y* curve from the backbone curve to the steady-state condition; thus, appropriate curves for short duration cyclic loading, such as earthquake or impact loading, are lacking.

To address the limitations to the existing soft clay *P-y* curves discussed above, the model presented in this dissertation embodies a unified description of *P-y* behavior featuring more realistic (stiffer) monotonic load response, a steady-state stiffness dependent on cyclic displacement amplitude, separate equations for describing monotonic versus cyclic behavior, and a complete description of evolving behavior from the backbone curve to the steady-state condition. The degradation component of the model can accommodate variable and random cyclic displacement amplitudes. The P-y relationships are highly dependent on the soil type, soil strength properties, and the nature of the cyclic loads.

Fatigue Life

Fatigue refers to the weakening of a material resulting from repeated changes in cyclic stresses that manifests itself in slow localized development of a crack. Fatigue life refers to an estimate of the number of cycles of loading that an object or material will survive under reversal stresses. Fatigue assessment of wells is a key aspect of the design and integrity assurance of deepwater riser-well systems (Zakeri, et al., 2015). Fatigue assessment is a crucial aspect of well conductor design and integrity assurance. Most of the fatigue damage that occurs, results from small magnitude load conditions at prolonged duration of incremental stresses. Most software programs, use the tangent stiffness along the backbone curve for fatigue assessment. The problem with this approach, is that fatigue evaluations should not be based on the backbone response, but on the cyclic response. In situations where transient loads are predominant (such as earthquakes), and do cause significant fatigue damage over time, it will be useful to actually track the stiffness degradation and account for the amount of fatigue life taken away from the structure by such loads.

This indicates the importance of soil-structure analysis in determining the cyclic stresses in the conductor or pile resulting from loads transmitted from the superstructure. Under cyclic loading, the shear strength of normally consolidated clays gradually degrades, which could result in reduction in axial and lateral bearing capacities and/or increase in displacements beyond acceptable design limits. Fatigue failure in offshore structural components, can result from accumulation of fatigue stresses, with magnitudes substantially below the ultimate design stresses.

The methodology used in characterizing the *P-y* behavior is based on instrumented centrifuge pile/conductor load tests, where displacements are imposed at the pile head (displacement control tests) and strains along the pile shaft are measured, from which line load *P* and displacement *y* are back-calculated. This approach has the limitation that measured *P-y*

response is dependent on the details of loading, namely force versus displacement control at the pile head, soil-pile interaction effects, the amplitude of cyclic loading, the relative magnitudes of the mean and cyclic components of loading, uniform versus random load cycles, and the frequency of loading. One consequence of soil-pile interaction is the redistribution of soil resistance along the depth of the pile during each load cycle. Therefore, irrespective of the loading conditions applied at the pile head, the measured "*P-y* loops" migrate in *P-y* space in a manner that correspond to neither force nor displacement control, thereby complicating data interpretation and input parameter selection for *P-y* predictive models. A second consequence is that displacements decay with increasing depth; thus, *P-y* behavior at greater depths must necessarily be derived from a data involving progressively smaller displacement magnitudes. Additional complexities to be explored when interpreting pile cyclic load test data are the relative magnitudes of the mean and cyclic components of loading and how to deal with random cyclic loading. Finally, time-dependent effects, such as consolidation and the dependence clay stress-strain-strength properties on strain rate, introduce a dependence on load frequency and pile diameter on soil response. Eventhough not explicitly incorporated in this research scope, consolidation effects are potentially very significant to the steady state response, since the prolonged duration of loading permits pore pressure redistribution, as recognized in similar studies of cyclically loaded steel catenary risers (Hodder et al., 2009; Clukey et al, 2017; Yuan et al., 2016).

Case Histories of Well System Fatigue Failures

A number of well system failures have occurred and some reported in the literature. A few of these occurrence are listed below. Sometimes its good practice to look back at historic and present events, to plan and improve the future. In a bit to make improvements, current practices need to be changed with lessons learnt and improved understanding of this subject (fatigue):

- 1981 – Gross structural fatigue failure of a surface casing/wellhead weld was experienced west of Shetland. First identified dynamic loading of subsea wellheads as a failure load (Lorents, 2012).
- 1990 – Fatigue failure of subsea development well in the UK Beryl field, which had to be abandoned (King, 1990).
- 1991 – Two wellhead failures in the field (Milberger et al., 1991).
- 2005 – Fatigue failure was of a conductor/conductor housing weld on a North Sea subsea well leading to experienced abnormal BOP movements by Norsk Hydro Oil and Gas (Møvik, 2006).
- 2006 – Observed relative movement between WH and conductor housing. Norsk Hydro, Fram Øst, B-24, Wellhead (WH) retrieved based on exceeded lifetime of 20in weld after 13 days of drilling (Monica Ovesen, 2012).
- 2007 – Observed relative movement between WH and conductor housing. Statoil, Vigdis Ext, F-4 H, 30 in conductor failure (Monica Ovesen, 2012).

Fatigue Analysis

Fatigue is often the leading failure mode of interest for vibration and sustained repeated loading environments (e.g. vibration, shock). Fatigue analysis is a relevant step to determining the life expectation of structures, when cyclic/dynamic or seismic loads are expected on a structure. Fatigue life represents the number of cycles until a part will fail due to fatigue if loading is reversed between loads of constant amplitudes. In cases where the loading amplitude is non-constant, it represents the number of loading blocks until failure of the element occurs.

Fatigue life represents the available life of the structure under the expected loading conditions. It important to understand that the loads expected on the structures are a forecast and based on experience and geographical locations. Improving modelling abilities aids in reducing the streams of uncertainty that occurs in fatigue life computations. For soil-structure interaction (SSI) from dynamic loads on the conductor / piles, the soil input is very crucial in the overall analysis and determination of the fatigue life of the structure.

The DNVGL-RP-C203 (2016) is the referenced manual for the fatigue life computations in this study, incorporating the rainflow counting method as described in ASTM E1049-85 (2017). The cycle counting methods are utilized when simplification of irregular timeseries is required. Thus, converting to blocks of regular timeseries with varying amplitudes and cycles, which have the same cumulative effect as the irregular time series. Once the irregular timeseries have been converted to an equivalent block of stress ranges and cycles, a representative S-N curve from the RP-C203 is then selected. The deflected shape (displacement) of the pile/conductor can be determined.from the analysis of the soil-structure interaction. The bending moment can be computed from the pile deflection using basic beam flexural relationships presented in Table 7.1 and

Figure 7.1. From the bending moment, the stress can be determined using the relationship shown in Eq. 2.1.

$$\sigma_{nominal} = \frac{M\,x}{I} \qquad \text{Eq. 2.1}$$

where,

I is the moment of inertia;

x is the distance from a point on the bending surface to the centroid;

$\sigma_{nominal}$ is the bending stresses; and

M is bending moment.

The fatigue damage accumulation is thereafter computed using the selected S-N curve to determine the failure number of cycles for the respective stress ranges. The expression in Eq. 2.2 based on the Palmgren-Miner rule, is used to determine the accumulated fatigue damage ($D_i$). If the fatigue damage is less than 1, the structure is considered safe, otherwise failure will or has occurred. The basic aim here was to compare the fatigue life computed from the model to that from the centrifuge tests. The C1 S-N curve in seawater with cathodic protection, considering thickness effects, described by Eq. 2.3, was used for this analysis.

$$D_i = \sum_{i=1}^{k} \frac{n_i}{N_i} \leq \frac{1}{DFF} \qquad \text{Eq. 2.2}$$

where,

D is the accumulated fatigue damage;

$n_i$ is the number of cycles associated with each stress block as obtained from the S-N curves;

$N_i$ is the number of cycles to failure at constant stress range (obtained from a reference S-N curve);

DFF is the design fatigue factor, an inverse of the usage factor; and

k is the number of stress blocks.

$$If\ N\ \leq 10^6:\ \ \log N = 12.049 - 3 * \log\left[\Delta\sigma\ \left(\frac{t}{t_{ref}}\right)^{0.10}\right] \qquad \text{Eq. 2.3}$$

$$If\ N\ > 10^6:\ \ \log N = 16.081 - 5 * \log\left[\Delta\sigma\ \left(\frac{t}{t_{ref}}\right)^{0.10}\right]$$

The fatigue life is hence determined as the ratio of the load series time duration to the total damage experienced in the time duration.

# CHAPTER III

# NON-LINEAR P-Y CURVE MODEL FORMULATION

Observations of the cyclic lateral response from the interaction of flexible vertical tubular structure (conductor or pile) and soil indicate this response is characterized by distinctive features. From the inception, to the end of the motion, these features, are controlled by complex mechanisms. The soil response will be governed by the magnitude of displacement the soil is subjected to, the consistency of the soil, its zone of confinement along the depth of the pile, and the undrained shear strength of the soil. The motions experienced by the conductors, within the framework of this program are categorized into symmetric cyclic loads (cyclic motions with zero offset), asymmetric cyclic loads (cyclic motions with offset), transient motions and random motions (which could have an offset). The motions with offsets do have a mean and are cycled about this mean position.

The behavior of the soil in the zone of influence of the cyclic laterally loaded flexible vertical tubular structure comprises of three (3) distinctive features which are:

(a) The Initial Pile Excursion

(b) The Cyclic Load Phase

(c) The Stiffness Degradation

The initial pile excursion starts from the inception of the load application in a specific direction until a load reversal occurs to push the conductor / pile in an opposite direction to its current trajectory. This is considered the initial excursion into the soil (undisturbed or disturbed soil zones) for that specific load regime. This model is formulated such that the initial pile excursion, occurs in the positive quadrant only.

The cyclic load phase begins once the load reverses direction from the initial pile excursion path which commences with the initial unload loop. Anytime a point is reached where the load or displacement is at its maximum or minimum load, a load reversal occurs and conductor/pile traverses in an opposite direction to its previous trajectory. This describes the unload and reload loops of the cyclic behavior. This unload loop occurs when the load goes from maximum to minimum reversal points. The reload loop, thus from minimum to maximum reversal points. The cyclic phase clearly incorporates a series of load reversals, depending on the number of cycles the forcing load subjects on the structure. The cyclic phase and the stiffness degradation phase occur simultaneously.

The Initial Pile Excursion Phase

The initial pile excursion phase is described mathematically by a hyperbolic load-displacement relationship of the form shown in Eq. 3.1 and schematically represented in Figure 3.1. The initial excursion load describes the relationship between the lateral displacement and mobilized soil resistance during the initial push of the pile into the soil (which could be in a pristine state, or disturbed by prior loading), prior to any load reversal. This hyperbolic model involves two dimensionless parameters: $K_{max}$ controls the initial tangent of the hyperbola and $f\ (= P/(s_u D))$ controls the asymptote. The displacement y is referenced to the pile configuration prior to motion application. When the loading is symmetric, i.e., uniform displacement amplitudes with a mean value of zero, this will be the pile installed configuration. However, when loading is asymmetric, uniform cyclic amplitudes about a non-zero mean displacement, or random, there might exist multiple excursions different from the initial excursion. The displacement, y is hence referenced to the pile configuration at the onset of the new pile excursion. The emphasis here is on

accurately describing $P$ in the working load range involving relatively small displacements $y$ (≤0.10D), as opposed to displacements in the vicinity of the limit state.

$$\frac{P}{s_u D} = \frac{K_{max}}{1+fK_{max}\left(\frac{\Delta y}{D}\right)}\left(\frac{\Delta y}{D}\right) \qquad \text{Eq. 3.1}$$

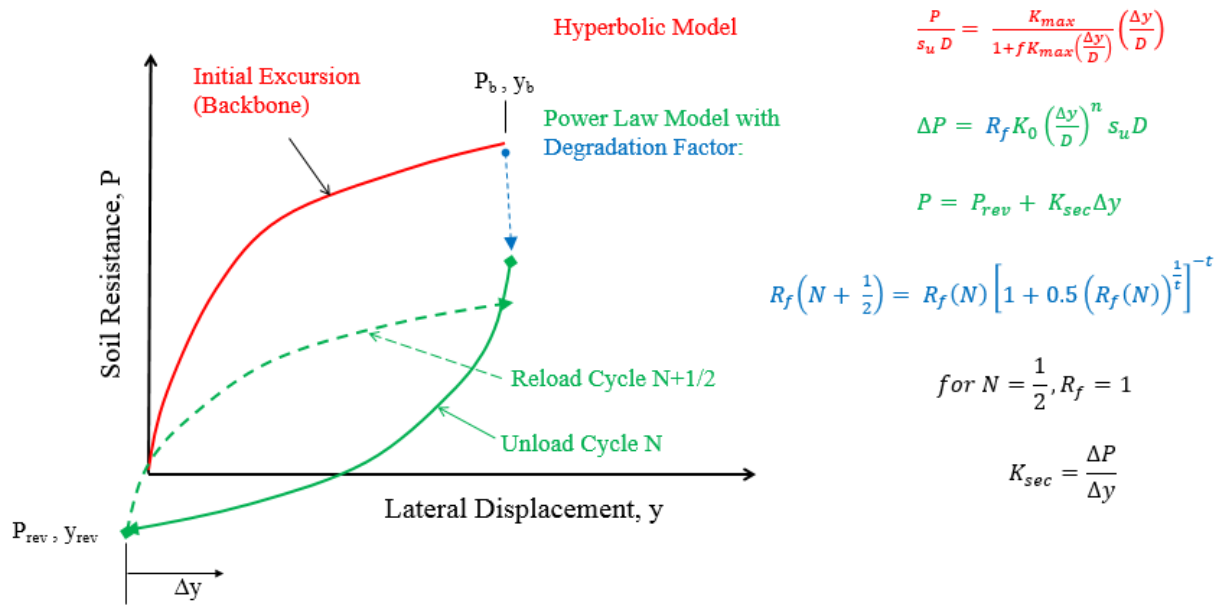


**Figure 3. 1: Schematic representation of the distinct phases of the cyclic load mechanism.**

The Cyclic Load Phase

The cyclic load phase consists of a series of unload and reload loops, triggered at the onset of a load reversal. Cyclic unloading occurs when the load is being reversed after reaching a peak load. Likewise, cyclic reload occurs when the load is being reversed from a minimum load point, after unloading. The change in soil resistance from the reversal points (peak or troughs), signifying unload or reload loops, is described by a power law equation of the following form in Eq. 3.2, also schematically represented in Figure 3.1.

$$\Delta P = R_f K_0 \left(\frac{\Delta y}{D}\right)^n s_u D \qquad \text{Eq. 3.2}$$

The soil resistance at the time steps within that loop can then be obtained from Eq. 3.3.

$$P = P_{rev} + K_{sec}\Delta y \qquad \text{Eq. 3.3}$$

$K_{sec}$, the secant stiffness, is obtained as shown in the following section, in Eq. 3.4 (a) and Eq. 3.4 (b).

$$K_{sec} = \frac{K_{max}}{1+fK_{max}\left(\frac{\Delta y}{D}\right)} s_u \qquad \text{(initial pile excursion)} \qquad \text{Eq. 3.4 (a)}$$

$$K_{sec} = R_f \frac{K_0}{\Delta y}\left(\frac{\Delta y}{D}\right)^n s_u D \qquad \text{(cyclic)} \qquad \text{Eq. 3.4 (b)}$$

Recall earlier, it was mentioned that there could exist an offset in the pile configuration prior to the current load being applied. When this occurs, if the pile is being pushed into soil not previously penetrated by the pile (when the displacement amplitudes are larger than previous displacement amplitudes in the load packet), the difference in the amplitude of push at the pile head (y_(max-new)) is checked against the maximum past amplitude (y_(max-past)). An illustration of this is shown in Figure 3.2, which is a section of actual raw data. This offset, could also occur with random load motions. If this difference is greater than 0.01D (1% pile diameter), we treat this as a new excursion and apply the hyperbolic model in Eq. 1. Otherwise, the rules applied to the symmetric harmonic motion still applies. The secant stiffness of this new excursion is scaled by a factor $\chi$ defined below. Eq. 3.4 (a) is thus replaced by Eq. 3.5. The major difference between the asymmetric and random motion, would be that the references for the new excursion will differ. If there is an offset prior to applying the motions (harmonic or random), the new excursion computations will be referenced to the offset pile position instead of the installed pile position.

If a new excursion exists, $\chi = \frac{y_{max-new}}{(y_{max-past}+y_{max-new})}$, otherwise, $\chi = 1$.

$$K_{sec} = \chi \frac{K_{max}}{1 + f K_{max}\left(\frac{\Delta y}{D}\right)} s_u \qquad \text{(new pile excursion)} \qquad \text{Eq. 3.5}$$

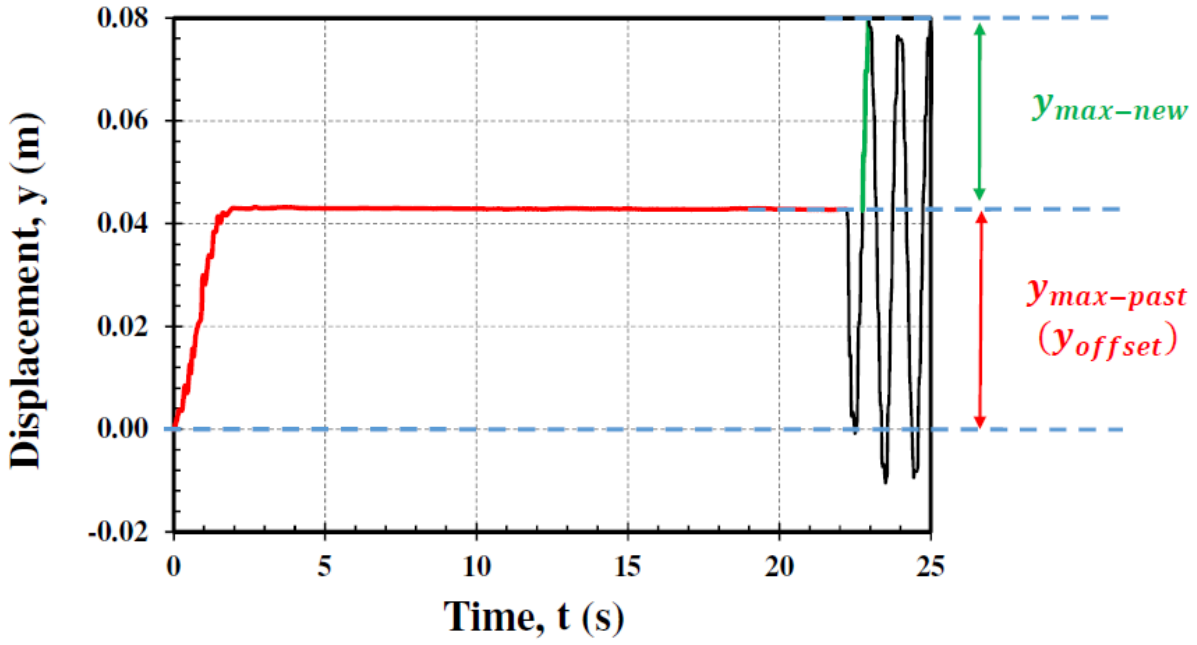


**Figure 3. 2: Illustration of the new excursion amplitude ($y_{max\text{-}new}$) relative to maximum past amplitude ($y_{max\text{-}past}$) for non-symmetric motions.**

The Stiffness Degradation Phase

The stiffness degradation phase occurs synchronously with the cycling phase, and controls the reduction in stiffness of the soil as the cycling progresses. The degradation resulting from the cyclic loads, creates a downward ratcheting of the reversal soil resistances, in *P*-*y* space. This behavior occurs in soft clays when displacement control is enforced, a trend previously observed in Idriss et al. (1976). To model the remaining cyclic unload/reload loop incorporating degradation effects, Eq. 3.6 was utilized to compute the reduction factor $R_f$ values appearing in Eq. 3.2. This is designed to induce a stiffness degradation at each load reversal (half cycle). Each reversal is considered to increase the load cycle *N* count by one-half.

Eq. 3.6 and 3.7 are formulated from the model proposed by Idriss, et al., 1978, for modelling the softening behavior of soft clays subjected to cyclic or earthquake motions. The cycling itself could result in soil remolding and softening, this softening of soil is observed in the reduction of the soil stiffness, and sometimes, in the soil strength.

$$K_{sec}\left(N+\tfrac{1}{2}\right)=\ R_f\left(N+\tfrac{1}{2}\right)K_{sec}\left(\tfrac{1}{2}\right) \qquad \text{Eq. 3.6}$$

$$R_f\left(N+\tfrac{1}{2}\right)=\ R_f(N)\left[1+0.5\left(R_f(N)\right)^{\frac{1}{t}}\right]^{-t} \qquad \text{Eq. 3.7}$$

N = 0, ½, 1, 3/2, 2, …

Non-Linear P-Y Curve Model Framework

The distinctive features of the cyclic P-y curve for modelling cyclic lateral soil structure interaction, has been introduced and described in the preceding paragraphs. Then following paragraphs in this chapter elucidates the link to these phases forming the non-linear p-y model required for analysis. Shown below are pictorial representations of how the different features are tied together. Figure 3.3 represents the flow chart for the symmetric harmonic, transient, and random motions while Figure 3.4 represents that for motions with offsets e.g. asymmetric motions (harmonic motions with offsets).

In Figure 3.3, the motion commences with initial conditions (initial pile configuration, undrained shear strength profile, pristine or disturbed soil conditions, etc.), then progresses along to the initial excursion of the pile into the soil surrounding the pile. Then there exists an initial unload of the pile having reached a maximum pile initial penetration, at which point, no degradation has occurred is assumed to have occurred. The initial unload path continues until the pile reaches its minimum point and another reversal occurs. At this point stiffness degradation

initiates, with the rate of degradation being controlled by the parameter *t* which, in turn, depends on the magnitude of cyclic loading $\Delta y_{cyc}$. Each subsequent load reversal increases the load cycle count by ½, which leads to progressively increasing stiffness degradation according to Eqs. 3.6 and 3.7.

Figure 3.4 shows a computation sequence similar to that described in Figure 3.3, except that if a sufficiently large reload excursion occurs, the hyperbolic model is triggered. The new excursion will occur if the difference between the amplitude of the reload point and the maximum past excursion is greater than 1% of the pile diameter (0.01D). The maximum past excursion for the asymmetric motions will always be the initial excursions point. The description in Figure 3.4 represents the generalized model, which applies to all load types. For the symmetric and transient loads, the new excursion component is never activated, which is the reflections of Figure 3.3. A summary of the P-y model equations and the parameters required to be calibrated are presented in Table 3.1.

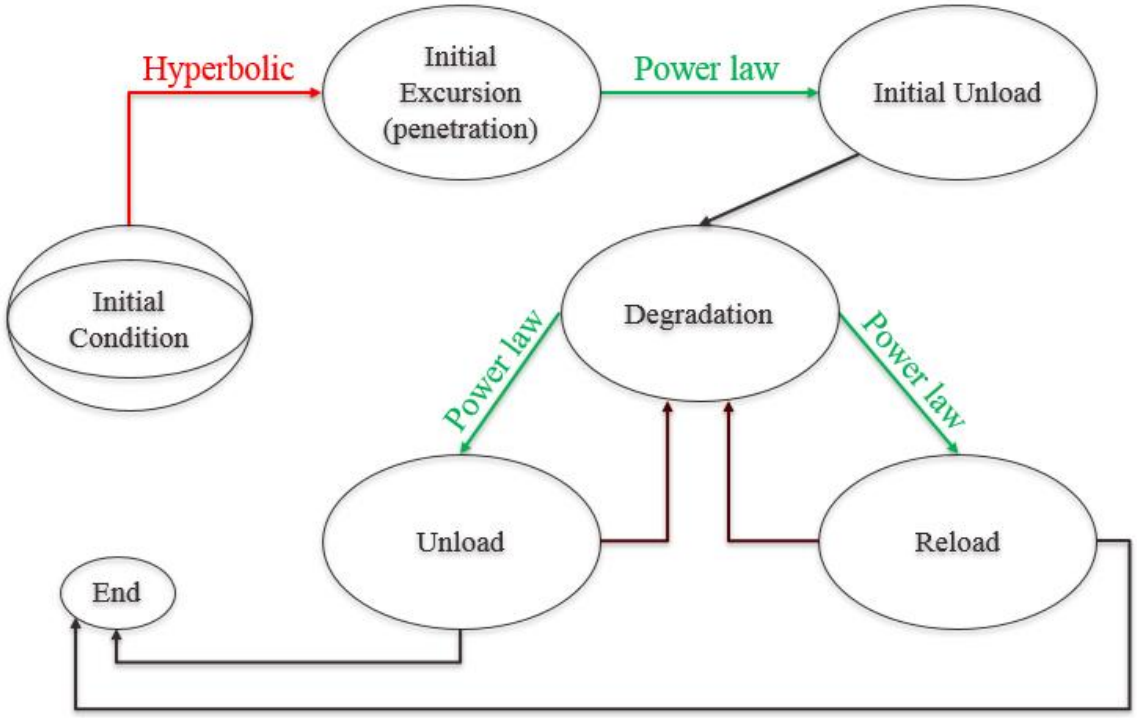


**Figure 3. 3: Flow chart describing the symmetric harmonic and transient motion model.**

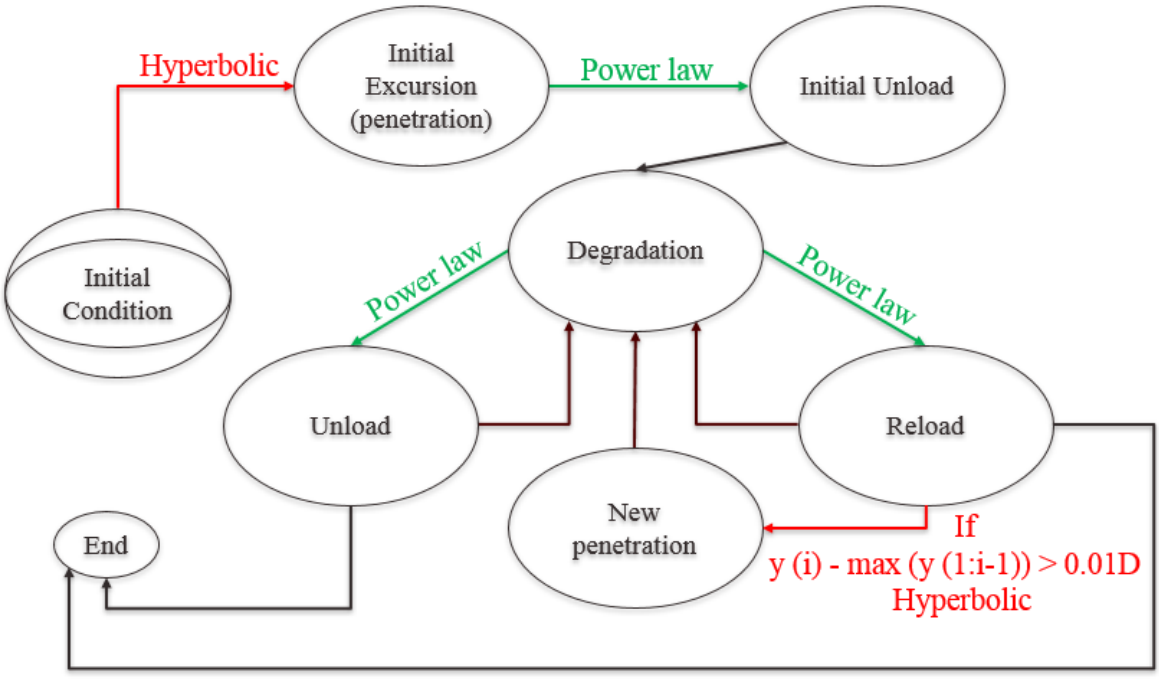


**Figure 3. 4: Flow chart describing the mechanism of motions with offsets.**

**Table 3.1: Summary of P-y model equations.**

| Model Component | Equation |
|---|---|
| **Initial Excursion Curve / Re-penetration** | $\frac{P}{s_u D} = \chi \frac{K_{max}}{1+fK_{max}\left(\frac{\Delta y}{D}\right)}\left(\frac{\Delta y}{D}\right)$<br><br>$K_{sec} = \chi \frac{K_{max}}{1 + fK_{max}\left(\frac{\Delta y}{D}\right)} s_u$<br>For initial pile excursion, $\chi = 1$<br><br>$\chi = \frac{y_{max-new}}{(y_{max-past} + y_{max-new})}$ (applies to re-penetration)<br><br>**$K_{max}$** and **f** from Table 5.1 and 5.2 |
| **Cyclic Unload / Reload** | $\Delta P = R_f K_0 \left(\frac{\Delta y}{D}\right)^n s_u D$<br><br>$P = P_{rev} + K_{sec}\Delta y$<br><br>$K_{sec} = R_f \frac{K_0}{\Delta y}\left(\frac{\Delta y}{D}\right)^n s_u D$ (Cyclic)<br><br>**$K_0$** and **n** from Table 5.1 and 5.2 |
| **Stiffness Degradation** | $K_{sec}\left(N + \frac{1}{2}\right) = R_f\left(N + \frac{1}{2}\right) K_{sec}\left(\frac{1}{2}\right)$<br><br>$R_f\left(N + \frac{1}{2}\right) = R_f(N)\left[1 + 0.5\left(R_f(N)\right)^{\frac{1}{t}}\right]^{-t}$<br><br>where, N = 0, ½, 1, 3/2, 2, …<br><br>**t** from Figure 5.7 |

# CHAPTER IV

# EXPERIMENTAL TEST PROGRAM

The experimental test program involved centrifuge model tests simulating a 30.50 m long, 0.0508 m wall thickness, 0.914 m diameter well conductor prototype, installed in normally consolidated to lightly over-consolidated kaolin clay, and over-consolidated glacial Canadian clay. These conductors were subjected to various lateral loading conditions recreated from field observations (Harmonic and random motions with zero (0) and non-zero means). The model tests were carried out at a centrifuge acceleration of 55.35 g. The test series (referred to as the Series 1 tests in Zakeri et al., 2016a, and Series 4 tests in Zakeri et al., 2016b) consisted of four (4) conductors.

## Testbed Preparation

### *Soft Clays*

The testbed was prepared from consolidated clay (Alwhite kaolin) slurry such that its moisture content was twice its liquid limit (LL). This slurry was consolidated in a circular strong box, with dimensions of 905 mm diameter by 595 mm deep. After an initial pre-consolidation, the clay sample was consolidated under downward hydraulic gradient (DHG) to achieve vertical stress of 20 kPa at the top and 280 kPa at the bottom. Once a constant stress state, and over 90% consolidation had been achieved in the clay sample, the clay surface was unloaded to zero (0 kPa) in 10 kPa decrements. Final consolidation of the testbed was achieved by loading the sample in the centrifuge and accelerating to 55.35g. Centrifuge consolidation was monitored using pore pressure transducers and a surface mounted linear voltage displacement transducer (LVDT).

The soil undrained shear strength, $s_u$, was measured by conducting Four (4) T-bar penetrometer tests, near the location of the 4 piles, and two (2) vane tests. Figure 4.1 shows a schematic of the conductor, and Figure 4.2a and 4.2b, shows a view of the Soft and Stiff clay test site respectively, with the conductors' arrangement in the steel tube. Figure 4.3a and 4.3b show the interpreted best line fit for the strength profile of the soft and stiff clay testbed respectively.

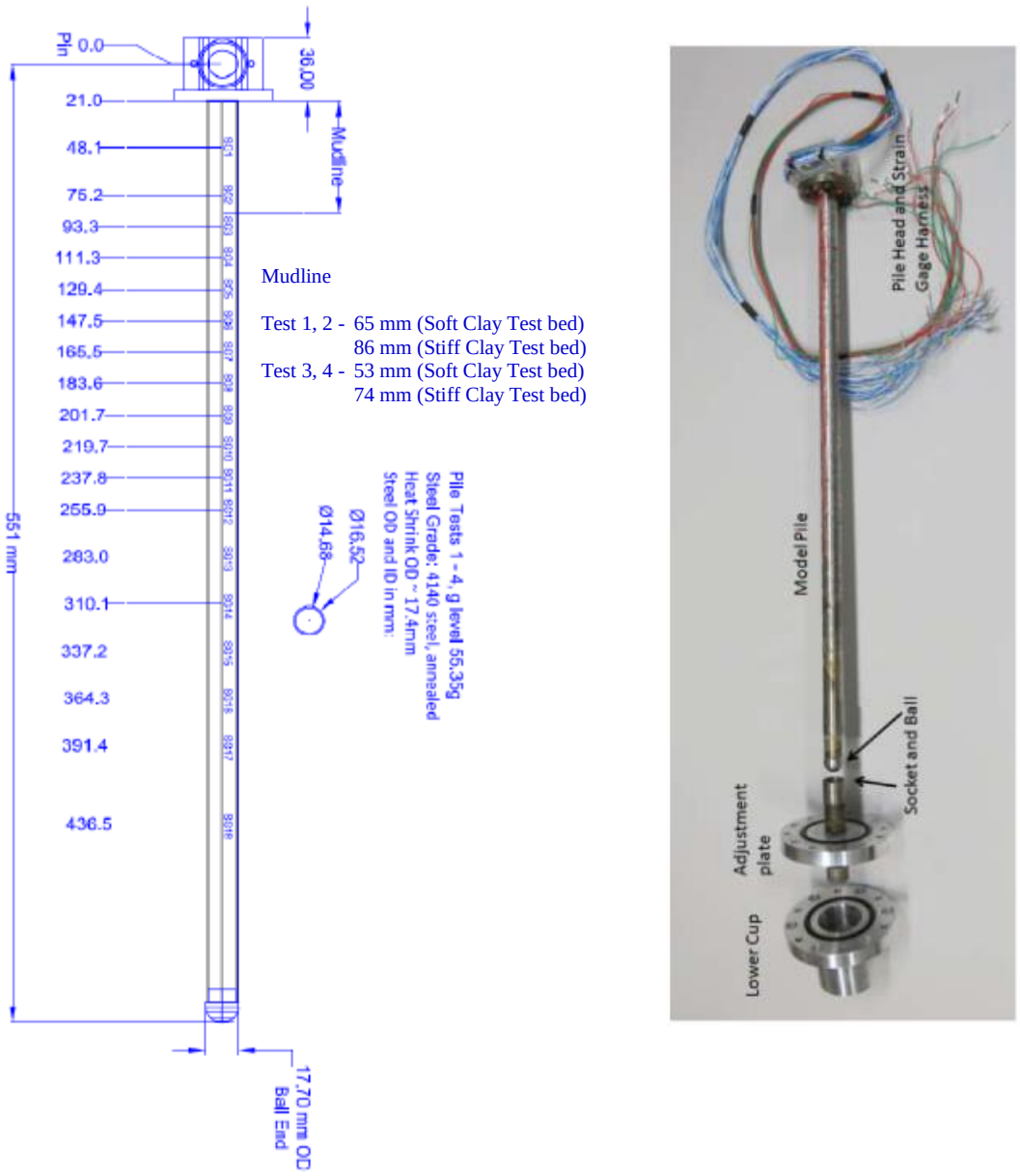


**Figure 4. 1: General schematic of the conductor setup.**

*Stiff Clays*

The testbed was prepared from consolidated clay (processed Canadian glacier till) slurry prepared to 48 % moisture content (twice its LL). This slurry was consolidated in a circular strong box, with dimensions of 905 mm diameter by 595 mm deep. After an initial pre-consolidation,

the clay sample was consolidated under downward hydraulic gradient (DHG) to achieve vertical stress of up to 640 kPa at the top. Upon achieving a constant stress state, with over 90 % consolidation in the clay sample, the clay surface was unloaded to zero (0 kPa). Final consolidation of the testbed was achieved in the centrifuge. Other procedures and monitoring methods were consistent with the descriptions in the preceding section.

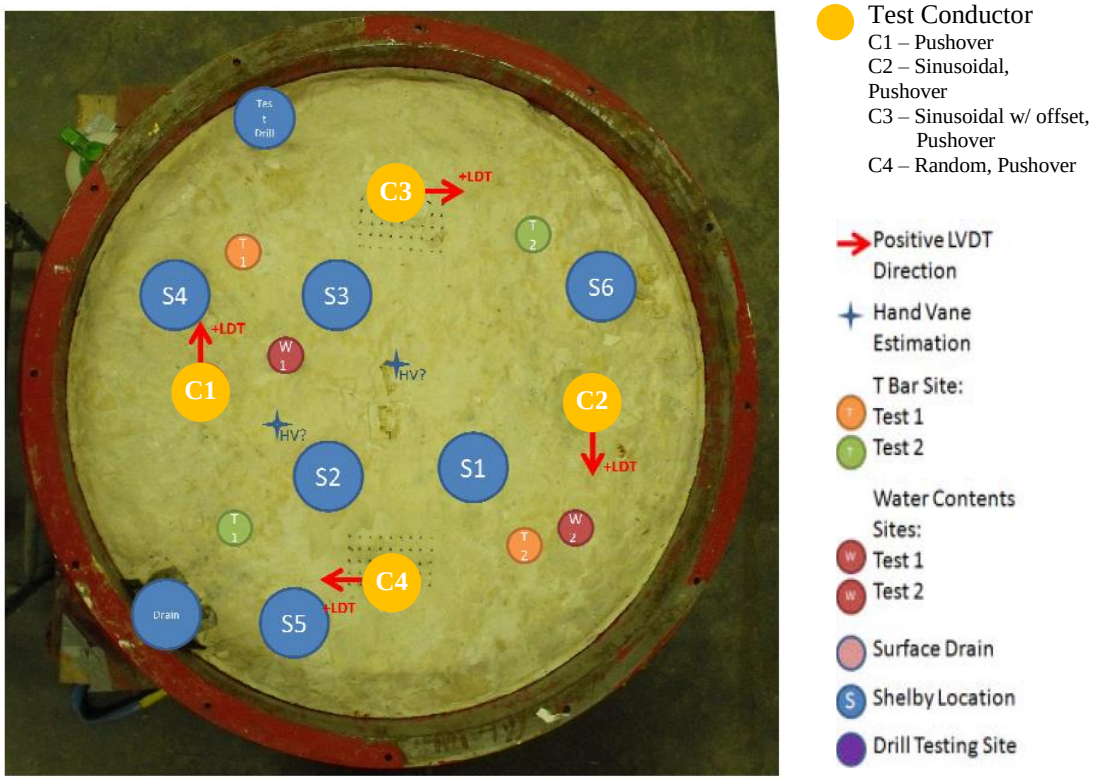


**Figure 4. 2 a: A view of the soft clay test bed site for the conductors.**

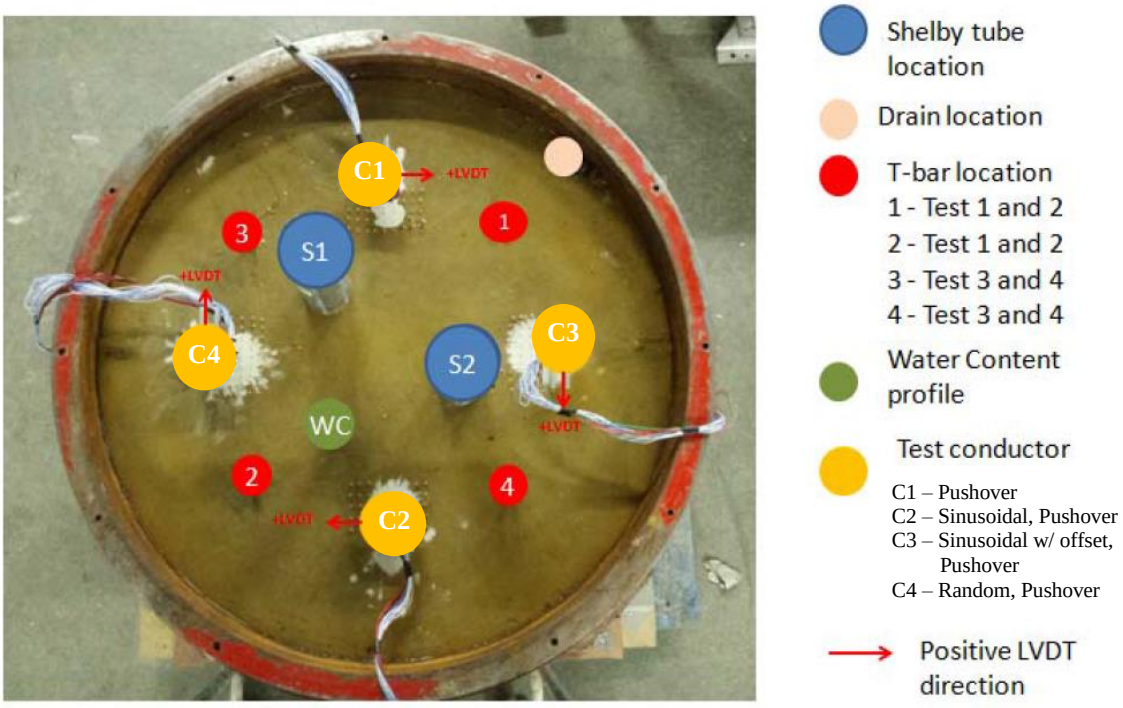


**Figure 4. 2 b: A view of the stiff clay test bed site for the conductors.**

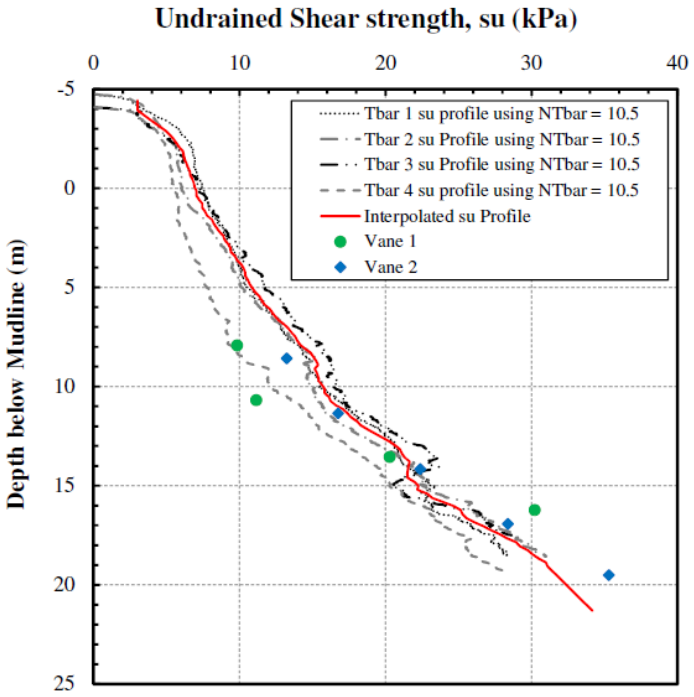


**Figure 4. 3 a: Undrained shear strength of the soft clay testbed.**

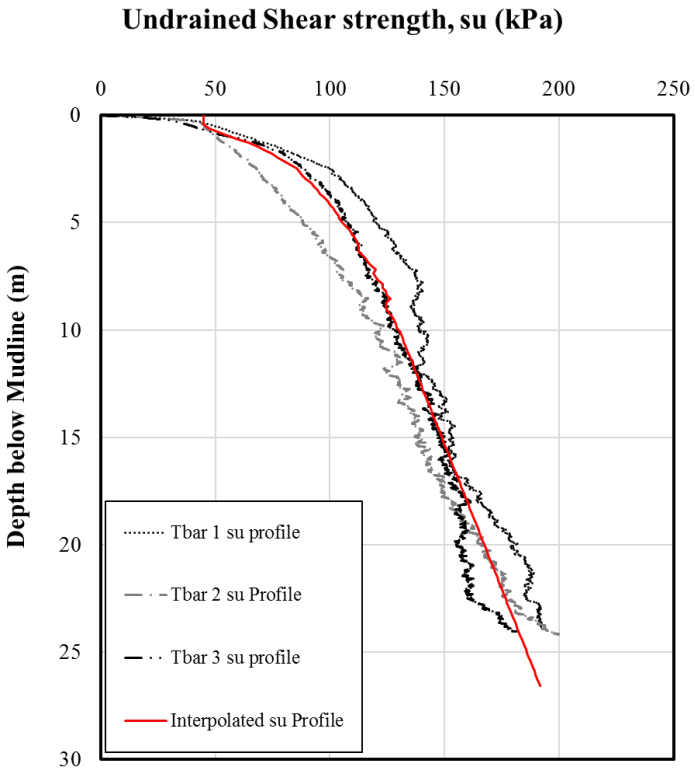


**Figure 4. 3 b: Undrained shear strength of the stiff clay testbed.**

Model Test Program

*Soft Clays*

The model test program involved displacement control tests consisting of monotonic load, regular wave, and irregular wave load applications. The model conductors (C1, C2, C3, and C4) were subjected to the following load sequences, which were bending tests: C1 was loaded monotonically (Test 1); C2 was subjected to a series of symmetric harmonic motions for 500 cycles (Test 2); C3 was subjected to 1000 cycles of harmonic motions, with some loading sequences being symmetric, others with prescribed offset (Test 3); and C4 was subjected to random motions, 100 repetitions of 10 second motion packet (Test 4). The loading sequence applied on C2, C3, and C4 were applied with a 3-month (prototype) rest period between each motion. A summarized

description of these applied loads is presented in Table 4.1. The term “offset” denotes a load condition where the mean displacement at the pile head is non-zero. The embedment depth C1 and C2 is 25.7 m; while for C3 and C4, it is 26.4 m. To minimize boundary and conductor-to-conductor interaction effects, a clearance of 7 D to 10 D was ensured between piles, and between the piles and the container walls. Each conductor was instrumented with 18 full Wheatstone bridges, and wrapped around with heat shrink tubing to protect the strain gages. The model conductors had a ball and socket boundary condition at the bottom, which ensured no translation while allowing rotation at the pile tip. At the pile head was a pinned linkage that ensures that purely lateral loads were applied without imparting axial force into the conductors. Table 4.2 shows the location of the strain gages along the conductor/pile depth, and the pile head location (zero moment) relative to the mudline. These distances shown are in prototype scale.

The elastic (Young’s modulus) and yield properties (yield stress) used in analysis were determined from tension tests carried out on three (3) tubular pipes manufactured with but different from the bending test pipe batch. The testbed was instrumented with pore pressure transducers (PPT), within the clay layers and at the water level to measure pore pressures. Consolidation of the testbed surface was measured using the two linear voltage displacement transducer (LVDT). Consolidation of the clay sample was monitored with the buried PPTs. Digital cameras were also installed to monitor soil deformation at the soil surface around the conductors during cyclic motions. Two load cells were installed at the conductor head to measure the applied loads, one primary, and a backup. Pile head rotations were measured with an installed inclinometer. An LVDT was installed at the actuator to measure pile head displacements, coupled with a laser used as a backup to measure pile head displacements. More details of the tests, loading conditions and material properties are presented in Zakeri et al. (2016a).

*Stiff Clays*

The centrifuge model test program were displacement control tests consisting of monotonic load, regular wave, and irregular wave load applications, exactly as described for the soft clays in the preceding section. The load programs for the model conductors (C1, C2, C3, C4), were similar to the description above for the soft clays. However, there is some variance in the exact amplitudes from experimentation procedures, with an added difference being that the symmetric harmonic motions on C2 were applied for 1000 cycles. The embedment depth C1 and C2 is approximately 26.6 m; while for C3 and C4, it is 26.5 m. The location of the strain gages (prototype scale) along the depth of the conductor/pile in reference to the mudline is depicted in Table 4.3.

In summary, Figure 4.1 shows a schematic for the strain gage locations along the depth of the conductor (left image), and also the pile toe ball and socket boundary condition (right image). The interpreted best line fit for the strength profile of the soft and stiff clay testbeds, is shown in Figure 4.3a and 4.3b.

**Table 4.1: Overview of the test program in normally consolidated to overconsolidated clay.**

| Cond. | Test Type | No. | Motion Description and Amplitudes | | | |
|---|---|---|---|---|---|---|
| | | | Offset | X Diameter (D)[1, 2] | Amplitude | |
| | | | | | Model Terms[3] (mm) | Prototype Terms[3] (mm) |
| ***C1*** | Pushover | Forward | - | 0.05D / -0.05D<br>0.5D / -0.5D<br>1.15D / -1.15D | 0.87 / -0.87<br>8.7 / -8.7<br>20.1 / -20.1 | 50.8 / -50.8<br>482.6 / -482.6<br>1118 / -1118 |
| | | Reverse | - | -1.71D / 1.71D | -29.75 / 29.75 | -1645 / 1645 |
| ***C2*** | Harmonic | m1 | 0 | 0.025D | 0.88 | 48.7 |
| | Harmonic | m2 | 0 | 0.05D | 1.74 | 96.3 |
| | Harmonic | m3 | 0 | 0.1D | 3.5 | 193.7 |
| | Harmonic | m4 | 0 | 0.15D | 5.2 | 287.8 |
| | Harmonic | m5 | 0 | 0.25D | 8.7 | 481.5 |
| | Harmonic | m2b | 0 | 0.05D | 1.74 | 96.3 |
| | Pushover | Forward | - | -1.15D / 1.15D | -20.0 / 20.0 | -1118 / 1118 |
| | Pushover | Reverse | - | -1.15D / 1.15D | -20.0 / 20.0 | -1118 / 1118 |
| ***C3*** | Harmonic | m1 | 0 | 0.025D | 0.88 | 48.7 |
| | Harmonic | m2 | 0.05D | 0.05D | 1.74 | 96.3 |
| | Harmonic | m3 | 0.05D | 0.1D | 3.5 | 193.7 |
| | Harmonic | m4 | 0.05D | 0.025D | 0.88 | 48.7 |
| | Harmonic | m5 | 0.1D | 0.025D | 0.88 | 48.7 |
| | Harmonic | m6 | 0 | 0.1D | 3.5 | 96.3 |
| | Harmonic | m7 | 0 | 0.15D | 5.2 | 287.8 |
| | Pushover | Forward | - | 0.75D / -0.75D | 13 / -13 | 715 / -715 |
| | Pushover | Reverse | - | -0.75D / 0.75D | -13 / 13 | -715 / 715 |
| ***C4[4]*** | Random | m1 | S1: 0.025D<br>S4: 0 | K – SS4 | RMS amp. = 0.22<br>Max amp. = 0.72 | RMS amp. = 12.2<br>Max amp. = 40.0 |
| | Random | m2 | S1: 0.025D<br>S4: 0 | T – SS4 | RMS amp. = 0.33<br>Max amp. = 0.95 | RMS amp. = 18.5<br>Max amp. = 52.8 |
| | Random | m3 | S1:0.025D<br>S4: 0 | T – SS7 | RMS amp. = 0.50<br>Max amp. = 1.57 | RMS amp. = 27.7<br>Max amp. = 87.1 |
| | Random | m4 | S1: -0.025D<br>S4: 0.05D | T – SS7 | | |
| | Random | m5 | S1: -0.075D<br>S4: 0.1D | T – SS7 | | |
| | Random | m6 | S1: 0.025D<br>S4: 0 | T – SS7 | | |
| | Pushover | Forward | - | 0.75D / -0.75D | 13 / -13 | 715 / -715 |
| | Pushover | Reverse | - | -0.75D / 0.75D | -13 / 13 | -715 / 715 |

Notes:

1. The outside diameter of the conductor with the protective heat shrink was 0.968 m prototype terms.
2. One-way amplitude.
3. Peak-to-peak amplitudes for harmonic motions and peak amplitudes for random motions.
4. After completion of the test, it was realized that Motions 1, 2, 3 and 6 in Series 1 were applied at an unintentional offset.
5. RMS = Root Mean Square

**Table 4.2: Centrifuge test measurements and locations referenced to the mudline for series 1 Tests.**

| Measured properties | C1 and C2 Referenced depth (m) | C3 and C4 Referenced depth (m) |
|---|---|---|
| Pile head tilt, y' | -4.76 | -4.10 |
| Pile head Displacement, y | | |
| Pile head force | | |
| Strain Gage 1 Moment | -2.10 | -1.43 |
| Strain Gage 2 Moment | -0.60 | 0.07 |
| Strain Gage 3 Moment | 0.40 | 1.07 |
| Strain Gage 4 Moment | 1.40 | 2.06 |
| Strain Gage 5 Moment | 2.40 | 3.07 |
| Strain Gage 6 Moment | 3.40 | 4.07 |
| Strain Gage 7 Moment | 4.40 | 5.06 |
| Strain Gage 8 Moment | 5.40 | 6.07 |
| Strain Gage 9 Moment | 6.40 | 7.07 |
| Strain Gage 10 Moment | 7.40 | 8.06 |
| Strain Gage 11 Moment | 8.40 | 9.07 |
| Strain Gage 12 Moment | 9.40 | 10.07 |
| Strain Gage 13 Moment | 10.90 | 11.57 |
| Strain Gage 14 Moment | 12.40 | 13.07 |
| Strain Gage 15 Moment | 13.90 | 14.57 |
| Strain Gage 16 Moment | 15.40 | 16.07 |
| Strain Gage 17 Moment | 16.90 | 17.57 |
| Strain Gage 18 Moment | 19.40 | 20.06 |

**Table 4.3: Centrifuge test measurements and locations referenced to the mudline for series 4 Tests.**

| Measured properties | C1 Referenced depth (m) | C2 Referenced depth (m) | C3 and C4 Referenced depth (m) |
|---|---|---|---|
| Pile head tilt, y' | -3.8745 | -3.9299 | -3.9852 |
| Pile head Displacement, y | | | |
| Pile head force | | | |
| Strain Gage 1 Moment | -1.2122 | -1.2676 | -1.3229 |
| Strain Gage 2 Moment | 0.2878 | 0.2324 | 0.1771 |
| Strain Gage 3 Moment | 1.2897 | 1.2343 | 1.1790 |
| Strain Gage 4 Moment | 2.2860 | 2.2306 | 2.1753 |
| Strain Gage 5 Moment | 3.2878 | 3.2324 | 3.1771 |
| Strain Gage 6 Moment | 4.2896 | 4.2342 | 4.1789 |
| Strain Gage 7 Moment | 5.2915 | 5.2361 | 5.1808 |
| Strain Gage 8 Moment | 6.2878 | 6.2324 | 6.1771 |
| Strain Gage 9 Moment | 7.2896 | 7.2342 | 7.1789 |
| Strain Gage 10 Moment | 8.2859 | 8.2305 | 8.1752 |
| Strain Gage 11 Moment | 9.2877 | 9.2323 | 9.1770 |
| Strain Gage 12 Moment | 10.2896 | 10.2342 | 10.1789 |
| Strain Gage 13 Moment | 11.7896 | 11.7342 | 11.6789 |
| Strain Gage 14 Moment | 13.2895 | 13.2341 | 13.1788 |
| Strain Gage 15 Moment | 14.7895 | 14.7341 | 14.6788 |
| Strain Gage 16 Moment | 16.2895 | 16.2341 | 16.1788 |
| Strain Gage 17 Moment | 17.7895 | 17.7341 | 17.6788 |
| Strain Gage 18 Moment | 20.2858 | 20.2304 | 20.1751 |

# CHAPTER V

# MODEL CALIBRATION

## P-y Curves from Bending Moment Profiles

The data reduction process began with the conversion of the strain gage data (bending moments) to soil resistance P and deflection y. The bending moments were obtained at the discrete locations along the depth of the conductor/pile as shown in Figure 5.1 or Table 5.2 and 5.3 (the strain gage locations). In order to obtain a continuous bending moment profile required in determining the *P-y* data; curve fits were carried out on the bending moment profiles.

Two approaches were considered for conducting the curve fitting/data reduction process of the harmonic motions. The results of both methods were compared for the data reduction, to verify consistency of the reduction process, and ensure that a reasonable *P-y* data representative of the tests carried out was employed in this analysis. These methods were the least squares method using a second order polynomial, and the cubic smoothing spline method (a curve fitting technique using function 'csaps' in Matlab®). In implementing the cubic smoothing spline method in Matlab®, a smoothing parameter value of 0.5 was used. A smoothing parameter of 0.5, yields an average fit between having a least-squares straight line fit (achieved with a smoothing parameter of zero (0)), and a natural cubic spline interpolant (achieved with a smoothing parameter of one (1)). Matlab® documentation shows more information on this procedure. This gave reasonable fits to the bending moment data, while minimizing sensitivity to the test data roughness, which is inevitable.

The *P-y* data was obtained using the differential equations for a beam subjected to pure bending, which relates to the problem of a vertical pile subjected to pure lateral load. The curve fitting of the cubic smoothing spline, yields a piecewise polynomial form, with the coefficients of the polynomial. The soil resistance, *P* is derived by taking the double differential of the bending moment fit equation ($P = d^2M / dz^2$), and the displacement, *y*, by double integration of the pile curvature (*M/EI*), where *M*(*z*) is the bending moment fit equation, *E* is Young's modulus, and *I* is area moment of inertia. The soil resistance and displacement profiles were then obtained from the mudline to pile toe, at 1m intervals along the conductor/pile depth. The data reduction process is schematically illustrated in Figure 5.1. Another consideration in the data reduction process, is normalizing the *P-y* data to enable results from the analysis be applicable to other conductors/piles with similar soil properties, and loading conditions. The normalization approach will be discussed subsequently. Figure 5.2 shows a schematic of the pile with the springs affixed to the pile, incorporating the cyclic *P-y* curves along the pile depth.

This test sequence provided high quality, and high-resolution data, simulating a wide range of cyclic load conditions, including uniform versus random loading, pile head displacement amplitudes ranging from 0.025 D - 0.250 *D*, and mean displacements during cyclic loading ranging from 0.0 to 0.1 *D*. The development of this nonlinear *P-y* model presented here was obtained from calibrations to the *P-y* data obtained from the harmonic motion test series mentioned and discussed in chapter III. The focus of this study is fatigue damage in conductors which typically arises from smaller range of motions. This will generally be harmonic motions, with cyclic displacement amplitude less than or equal to 10 % of conductor diameter (0.10 D). However, this model has been calibrated to the test data beyond this range, up to 15 % of conductor diameter (0.15 D).

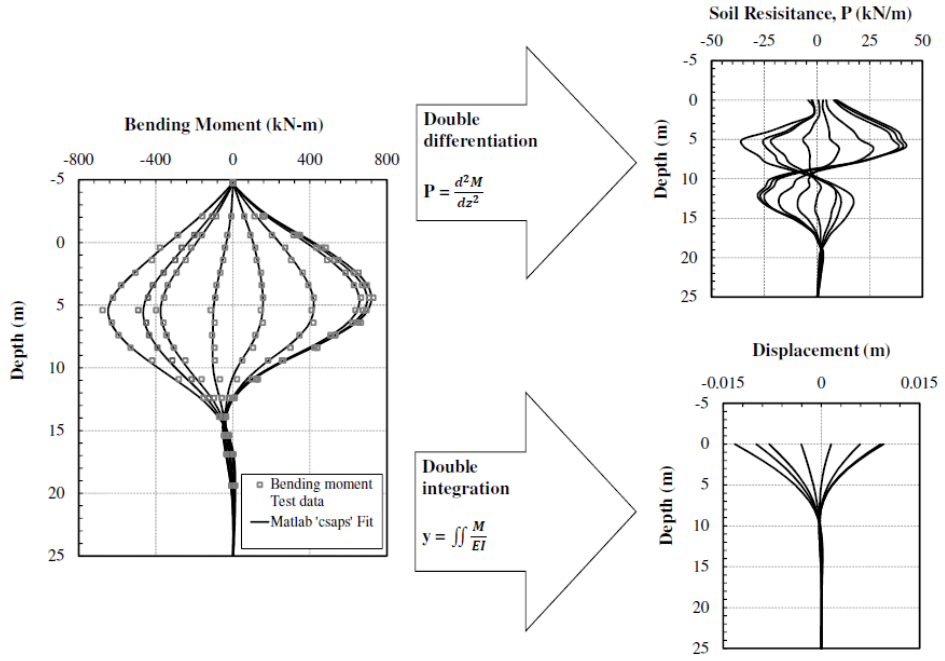


**Figure 5. 1: Schematic representation of the data reduction process from the bending moments to soil resistance (P), and deflection (y) data.**

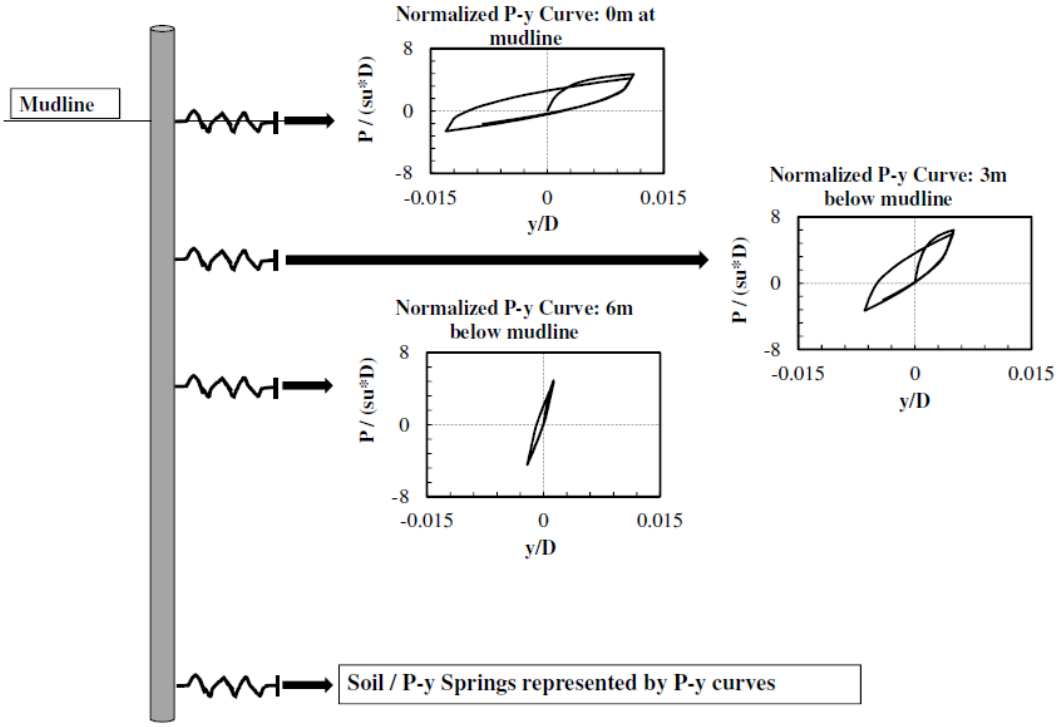


**Figure 5. 2: A schematic of a cyclic laterally loaded pile with the springs affixed to the pile.**

*Model Parameter Evaluation*

The section below briefly describes the model parameter determination process. This involved calibrations to harmonic motions data, with cyclic displacement amplitude less than or equal to 0.15 D. It describes the curve fitting to the normalized cyclic P-y data, and the stiffness degradation parameter calibration process.

*Normalization of P-y Curves*

Historically, soil resistance has been normalized by ultimate soil resistance $P_{ult} = N_p(z)s_uD$ determined empirically or from plasticity theory. In principle, this approach has the advantage of having a bearing function $N_p(z)$ that is independent of diameter, where $N_p(z)$ can be determined experimentally or analytically (Murff and Hamilton, 1993). However, the estimation of $N_p$ is subject to different levels of interpretation, failure mechanism and uncertainties, such as the occurrence of gapping, variation in the strength profile, roughness of pile surface and discrepancies between analytical and experimental measures of ultimate resistance. Jeanjean, et al. (2017) describes approaches available for estimating $N_p(z)$ for different modes of failures and compares predictions made with a wide range of load scenarios applied on test piles. Normalizations by the $P_{ult}$ was carried out, however, the depth dependency of the normalized p-y curves were still evident. Given that normalization by $P_{ult}$ yielded little benefit, lateral soil resistance was normalized by undrained strength * Pile diameter ($s_uD$) at the depth under consideration. This normalization method could limit the model parameters derived from the experimental data to be valid only for pile diameters on the order of 1 m. Following prevailing practice, lateral displacement $y$ was normalized by the diameter, $D$.

Least squares optimized nonlinear curve fits were carried out for the normalized *P-y* data. The least squares curve fits were achieved by implementing a curve fitting technique using function 'lsqnonlin' in Matlab®, and including robust least squares, with guidelines available in Matlab® documentation, using the bisquares weights method. The lower bound were set as zero (0) for all parameters. The upper bounds were set to 1 for *f* and *n*, 1500 for $K_0$, and 20000 for $K_{max}$, for the soft clay. However, for the stiff clay, the upper bounds were set to 1 for *f* and *n*, 1500 for $K_0$, and 10000 for $K_{max}$. The curve fit parameter from the method yielding the lower norm of residuals, was implemented in the *P-y* model. The corresponding curve fits are described in the sections below.

*Initial Pile Excursion Curve*

As noted earlier, soil resistance mobilized during the initial excursion of the pile into the soil is described by Eq. 2.1, which requires evaluation of $K_{max}$ and *f*. To derive values for these parameters, curve fits were made at 1 m intervals along the pile. Using the numerical integration and differentiation techniques described earlier, *P-y* curves of sufficient resolution to obtain meaningful curve fits were possible down to about 8 - 10 m BML. Below this depth, purely linear behavior with stiffness $K_{max}$ and *f* was assumed due to little movements, with $K_{max}$ and *f* fixed at 20000, and zero (0) respectively, at the pile tip for the soft clay, for the stiff clay $K_{max}$ and *f* were 10000, and zero (0) respectively. Parameters for intermediate depths between the pile tip and the last calibration depth were obtained by linear interpolations. Figure 5.3 shows the curve fits to the initial excursion of Test 2 (C2): M1, and Test 3 (C3): M1 *P-y* curves, at 4m BML for soft clay and 2m BML for stiff clay. The results for other depths and motions are presented in Appendix A. The sample calibration fits shown in Figure 5.3 where selected in the region of the maximum bending

moment locations. Table 5.1 and 5.2 show depth dependent values of the $K_{max}$ and f parameters for soft and stiff clay respectively.

## SOFT CLAY

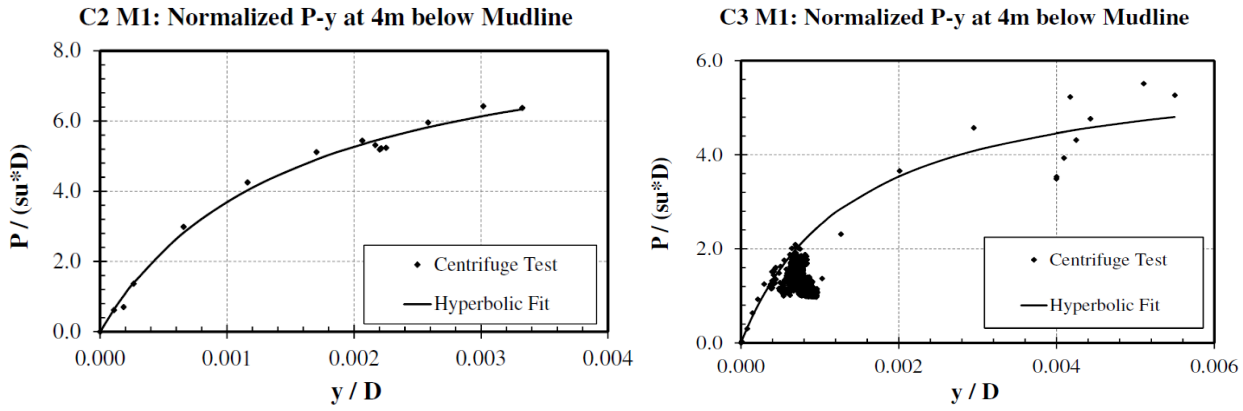


## STIFF CLAY

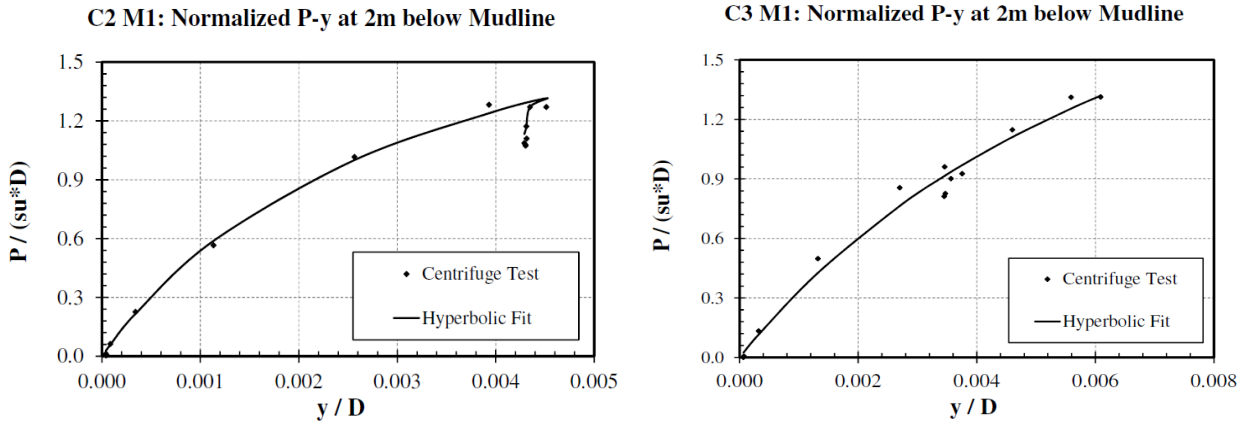


**Figure 5. 3: Hyperbolic curve fit for the initial pile excursion close to the region of maximum bending moment.**

*Cyclic Unload and Reload Loops*

The cyclic unload and reload loops commenced after the initial excursion load, after the first load reversal. *P-y* behavior corresponding to the unload/reload loops was modelled using the power law equation described by Eq. 2.2. Eq. 2.2 was fitted to the unloading branch of the initial loop ($N$ = ½) to obtain best-fit estimates of $K_0$ and $n$. Figure 5.4 shows curve fits to the initial unload loop for Test 3 (C3): M1 *P-y* curves at 5m BML for soft clay. Figure 5.4 also shows curve fits to the initial unload loop for Test 2 (C2): M1, and Test 3 (C3): M1 *P-y* curves at 3m BML for stiff clay. The results for other depths and motions are presented in Appendix B. The sample calibration fits shown in Figure 5.4 were selected in the region of the maximum bending moment locations. Although the possibility of using depth-independent values of $K_0$ and $n$ was explored, deviations between measured and model evaluations of bending moments were judged to be excessive. Hence the choice of depth-dependent values for the power law parameters, as shown in Table 5.1 for soft clay and Table 5.2 for stiff clay. Below the depth where displacements are sufficiently large to provide meaningful P-y interpretations, a finite stiffness must still be specified. The analysis therefore assigns a stiffness obtained by linear interpolation between the stiffness at the last measurable depth and the stiffness computed using $K_0$ = 1500 and $n$ = 1 at the pile toe. Analysis of the unload-reload loops for load cycles $N$>1 showed that the best matches were achieved when the parameters $K_0$ and $n$ were updated for each load cycle. However, this required a large array of input parameters without a commensurate improvement in the ability to predict cyclic bending stresses in the pile. Therefore, a model format was adopted in which $K_0$ and $n$ are taken as a function of depth, but the values for the first load cycle are taken to be applicable to all subsequent load cycles. It is further noted that the variation of the power law parameters with increasing cycles is, to some extent, implicitly modelled when the stiffness degradation effect is

accounted for. Finally, *P-y* behavior, especially at shallow depths with large pile head displacements, deviates substantially from the power law form (see Figure 5.5). The comforting part is that the soil resistance at these shallow depths is relatively small and has minor influence on computed bending moments controlling fatigue life. Accordingly, the model does not attempt to rigorously simulate the complex soil behavior in this region.

## SOFT CLAY

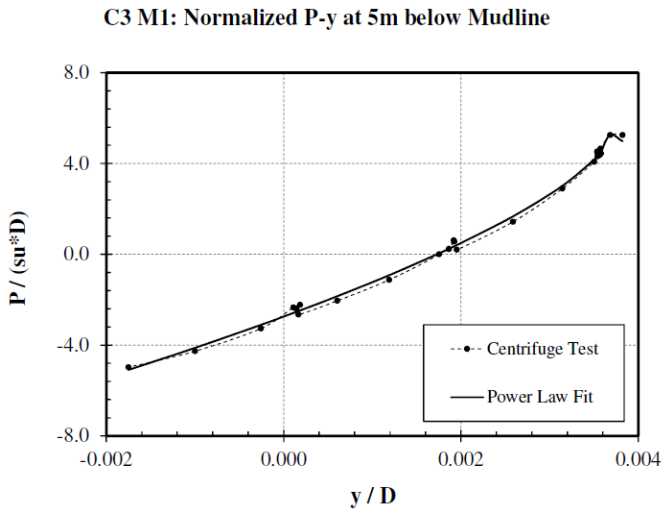


## STIFF CLAY

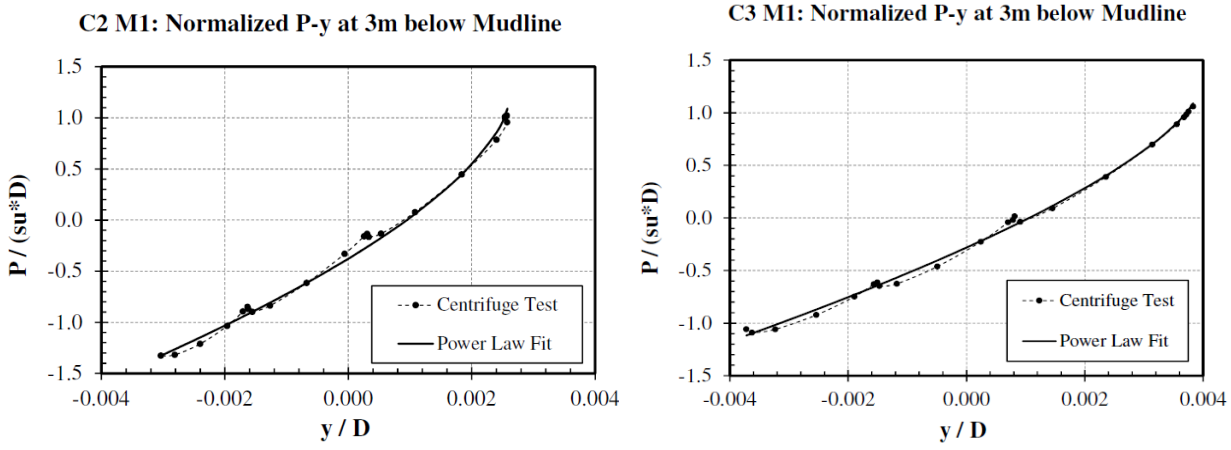


**Figure 5. 4: Power law curve fit for the initial unload curve close to the region of maximum bending moment.**

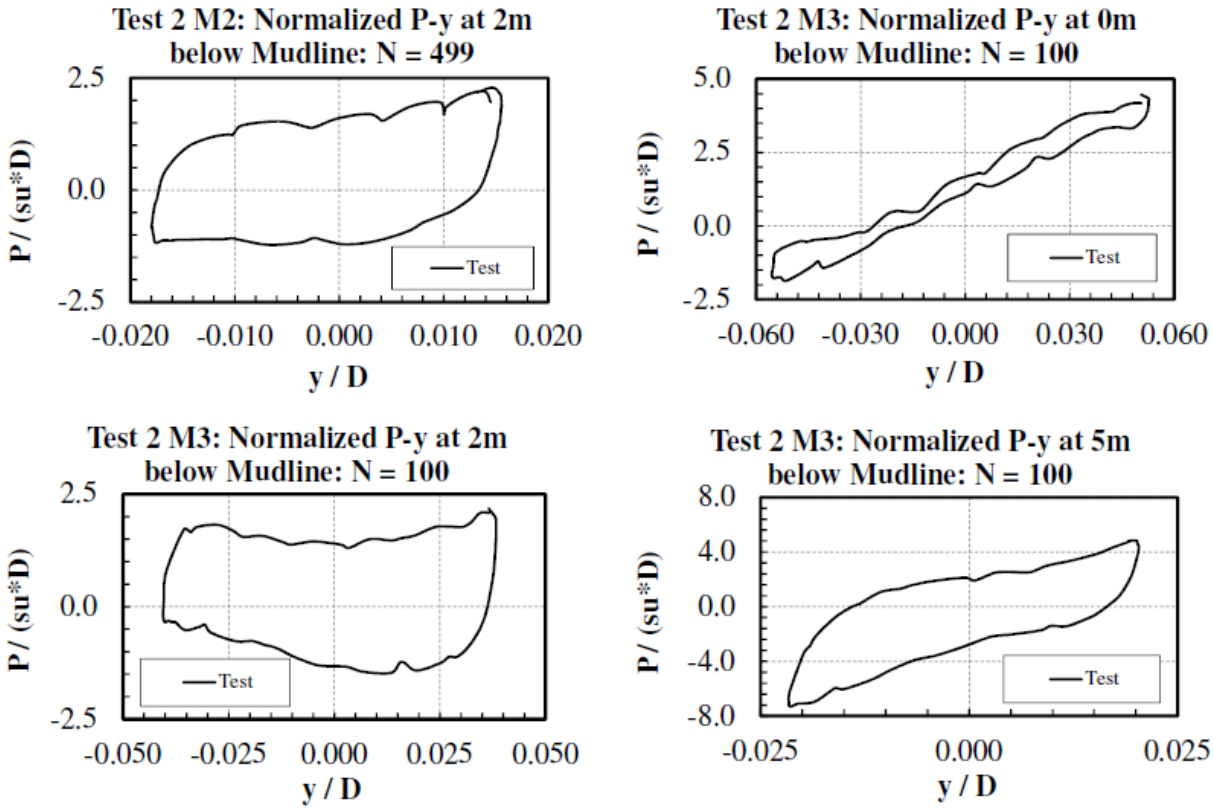


**Figure 5. 5: Varied shapes of test P-y curves deviating from the power law form.**

**Table 5.1: Soft clay initial pile excursion and cyclic P-y parameters.**

| z /D | Motion | Kmax | f | $K_0$ | n |
|---|---|---|---|---|---|
| 0 | Test 2 (C2) M1 Pristine Soil | 2750 | 0.2064 | Refer to Test 3 M1 Parameters | |
| 1.04 | | 5377 | 0.1822 | | |
| 2.07 | | 5453 | 0.1779 | | |
| 3.11 | | 6151 | 0.1378 | | |
| 4.15 | | 6198 | 0.1093 | | |
| 5.19 | | 6011 | 0.0911 | | |
| 6.23 | | 4843 | 0.0540 | | |
| 0 | Test 2 (C2) M2 Disturbed Soil | 688 | 0.1362 | 62.37 | 0.6533 |
| 1.04 | | 2351 | 0.2265 | 24.13 | 0.3489 |
| 2.07 | | 2867 | 0.2195 | 25.57 | 0.3316 |
| 3.11 | | 3326 | 0.1468 | 62.77 | 0.4425 |
| 4.15 | | 3957 | 0.1011 | 131.84 | 0.5221 |
| 5.19 | | 4912 | 0.0816 | 245.90 | 0.5865 |
| 6.23 | | 5331 | 0.0749 | 333.60 | 0.6212 |
| 7.27 | | 3059 | 0.0600 | 640.79 | 0.7501 |
| 8.31 | | | | 1180.01 | 0.8230 |
| 9.34 | | | | 1500.00 | 0.9075 |
| 0 | Test 2 (C2) M3 Disturbed Soil | 367 | 0.1265 | 40.02 | 0.6126 |
| 1.04 | | 2861 | 0.2930 | 11.65 | 0.2551 |
| 2.07 | | 1803 | 0.2478 | 11.43 | 0.2145 |
| 3.11 | | 1670 | 0.1583 | 33.32 | 0.3645 |
| 4.15 | | 1966 | 0.0961 | 78.57 | 0.4707 |
| 5.19 | | 2259 | 0.0629 | 136.07 | 0.5177 |
| 6.23 | | 2711 | 0.0549 | 174.50 | 0.5416 |
| 7.27 | | 1703 | 0.0484 | 269.25 | 0.6447 |
| 8.31 | | 2836 | 0.0821 | 429.32 | 0.6999 |
| 9.34 | | 5641 | 0.1281 | 479.71 | 0.6839 |
| 10.38 | | | | 1500.00 | 0.8398 |
| 0 | Test 2 (C2) M4 Disturbed Soil | 360 | 0.1916 | 22.62 | 0.6009 |
| 1.04 | | 20000 | 0.5819 | 4.41 | 0.1610 |
| 2.07 | | 1297 | 0.4904 | 4.20 | 0.0971 |
| 3.11 | | 1258 | 0.2754 | 12.01 | 0.2210 |
| 4.15 | | 1545 | 0.1619 | 30.72 | 0.3509 |
| 5.19 | | 1798 | 0.1142 | 54.32 | 0.4104 |
| 6.23 | | 2727 | 0.1078 | 61.86 | 0.4097 |
| 7.27 | | 2545 | 0.1531 | 70.43 | 0.4501 |
| 8.31 | | 3066 | 0.1035 | 111.19 | 0.4762 |
| 9.34 | | 4378 | 0.0883 | 136.93 | 0.4767 |
| | | | | 277.86 | 0.6073 |

| z /D | Motion | Kmax | f | $K_0$ | n |
|---|---|---|---|---|---|
| 0 | Test 3 (C3) M1 Pristine Soil | 3263 | 0.4213 | 52.83 | 0.5699 |
| 1.04 | | 7653 | 0.3793 | 55.02 | 0.5240 |
| 2.07 | | 5821 | 0.3495 | 89.72 | 0.5957 |
| 3.11 | | 4735 | 0.2494 | 163.99 | 0.6465 |
| 4.15 | | 4267 | 0.1656 | 299.87 | 0.6820 |
| 5.19 | | 3631 | 0.1288 | 326.49 | 0.6618 |
| 6.23 | | 3094 | 0.0742 | 462.53 | 0.6961 |
| 7.27 | | 3395 | 0.0392 | 949.91 | 0.7948 |
| 8.31 | | | | 1500.00 | 0.8902 |
| 0 | Test 3 (C3) M2 Disturbed Soil | 777 | 0.2735 | 21.68 | 0.3795 |
| 1.04 | | 2088 | 0.3166 | 17.90 | 0.2961 |
| 2.07 | | 2981 | 0.2980 | 20.99 | 0.3166 |
| 3.11 | | 4123 | 0.2176 | 33.37 | 0.3454 |
| 4.15 | | 5760 | 0.1549 | 68.71 | 0.4258 |
| 5.19 | | 7988 | 0.1607 | 90.05 | 0.4600 |
| 6.23 | | 9840 | 0.1674 | 124.28 | 0.5012 |
| 7.27 | | 11399 | 0.1792 | 190.57 | 0.5561 |
| 8.31 | | 10467 | 0.2227 | 387.14 | 0.6691 |
| 9.34 | | 20000 | 0.3225 | 1500.00 | 0.8394 |
| 0 | Test 3 (C3) M3 Disturbed Soil | 694 | 0.5584 | 15.79 | 0.3965 |
| 1.04 | | 2786 | 0.8755 | 9.64 | 0.2685 |
| 2.07 | | 3032 | 0.7004 | 12.30 | 0.2846 |
| 3.11 | | 3466 | 0.3767 | 24.11 | 0.3385 |
| 4.15 | | 4310 | 0.2082 | 49.93 | 0.3957 |
| 5.19 | | 5607 | 0.1813 | 60.88 | 0.4132 |
| 6.23 | | 6406 | 0.1567 | 83.26 | 0.4511 |
| 7.27 | | 6703 | 0.1396 | 127.45 | 0.5019 |
| 8.31 | | 5395 | 0.1320 | 202.91 | 0.5705 |
| 9.34 | | 5209 | 0.0769 | 420.62 | 0.6593 |
| 10.38 | | | | 1500.00 | 0.8381 |
| 0 | Test 3 (C3) M4 Disturbed Soil | 197 | 0.8279 | 10.85 | 0.5300 |
| 1.04 | | 45 | 1.0000 | 4.05 | 0.2775 |
| 2.07 | | 102 | 1.0000 | 5.63 | 0.2900 |
| 3.11 | | 6381 | 0.7285 | 13.02 | 0.3589 |
| 4.15 | | 4150 | 0.3832 | 27.36 | 0.4055 |
| 5.19 | | 6151 | 0.3784 | 30.77 | 0.3939 |
| 6.23 | | 6627 | 0.3065 | 42.57 | 0.4133 |
| 7.27 | | 6383 | 0.2369 | 88.55 | 0.4993 |
| 8.31 | | 5662 | 0.1985 | 200.96 | 0.6083 |
| 9.34 | | 7730 | 0.1723 | 588.55 | 0.7198 |
| 10.38 | | 9935 | 0.1881 | 1500 | 0.8231 |

Notes: z is depth along the conductor and D is conductor's outside diameter.

**Table 5.2: Stiff clay initial pile excursion and cyclic P-y parameters.**

| z /D | Motion | Kmax | f | K0 | n |
|---|---|---|---|---|---|
| 0 | Test 2 (C2) M1 Pristine Soil | 438 | 0.5711 | 25.18 | 0.6054 |
| 1.04 | | 693 | 0.4179 | 39.05 | 0.5968 |
| 2.07 | | 703 | 0.4452 | 45.21 | 0.5924 |
| 3.11 | | 970 | 0.4463 | 60.67 | 0.6156 |
| 4.15 | | 1008 | 0.4694 | 173.14 | 0.7894 |
| 5.19 | | | | 571.13 | 0.9475 |
| 0 | Test 2 (C2) M2 Disturbed Soil | 200 | 0.2754 | 18.89 | 0.5367 |
| 1.04 | | 342 | 0.2179 | 35.31 | 0.5827 |
| 2.07 | | 369 | 0.2866 | 78.74 | 0.7396 |
| 3.11 | | 379 | 0.2730 | 108.60 | 0.7854 |
| 4.15 | | 420 | 0.1623 | 132.00 | 0.7918 |
| 5.19 | | 738 | 0.2050 | 175.98 | 0.7871 |
| 6.23 | | | | 190.07 | 0.8278 |
| 0 | Test 2 (C2) M3 Disturbed Soil | 110 | 0.1615 | 9.52 | 0.3661 |
| 1.04 | | 191 | 0.1248 | 19.85 | 0.4502 |
| 2.07 | | 212 | 0.1803 | 48.77 | 0.6513 |
| 3.11 | | 291 | 0.1954 | 50.57 | 0.6295 |
| 4.15 | | 507 | 0.2226 | 44.32 | 0.5685 |
| 5.19 | | 718 | 0.1353 | 39.23 | 0.5024 |
| 6.23 | | | | 43.87 | 0.5633 |
| 0 | Test 2 (C2) M4 Disturbed Soil | 15 | 1.0000 | 0.46 | 0.0184 |
| 1.04 | | 41 | 0.5726 | 2.27 | 0.1832 |
| 2.07 | | 61 | 0.4481 | 11.47 | 0.4980 |
| 3.11 | | 105 | 0.2972 | 17.43 | 0.5151 |
| 4.15 | | 168 | 0.2052 | 20.36 | 0.4713 |
| 5.19 | | 255 | 0.1353 | 23.67 | 0.4269 |

| z /D | Motion | Kmax | f | K0 | n |
|---|---|---|---|---|---|
| 0 | Test 3 (C3) M1 Pristine Soil | 178 | 0.9368 | 9.68 | 0.4920 |
| 1.04 | | 250 | 0.4187 | 25.62 | 0.5949 |
| 2.07 | | 373 | 0.3182 | 41.39 | 0.6271 |
| 3.11 | | 497 | 0.3293 | 60.12 | 0.6675 |
| 4.15 | | 405 | 0.3918 | 80.03 | 0.7585 |
| 5.19 | | | | 339.99 | 1.0000 |
| 0 | Test 3 (C3) M2 Disturbed Soil | 119 | 1.0000 | 5.96 | 0.3649 |
| 1.04 | | 202 | 0.5786 | 15.92 | 0.5277 |
| 2.07 | | 293 | 0.4613 | 33.33 | 0.6514 |
| 3.11 | | 430 | 0.4072 | 53.86 | 0.7036 |
| 4.15 | | 416 | 0.3459 | 115.12 | 0.8403 |
| 5.19 | | | | | |
| 6.23 | | | | | |
| 0 | Test 3 (C3) M3 Disturbed Soil | Refer to Test 3 M2 Parameters | | 5.00 | 0.3480 |
| 1.04 | | | | 13.76 | 0.5237 |
| 2.07 | | | | 26.41 | 0.6358 |
| 3.11 | | | | 57.04 | 0.7301 |
| 4.15 | | | | 116.47 | 0.8505 |
| 5.19 | | | | 317.93 | 1.0000 |
| 6.23 | | | | | |
| 0 | Test 3 (C3) M4 Disturbed Soil | 16 | 1.0000 | 1.58 | 0.4706 |
| 1.04 | | 38 | 1.0000 | 1.99 | 0.4419 |
| 2.07 | | 66 | 1.0000 | 2.30 | 0.4345 |
| 3.11 | | 228 | 1.0000 | 12.81 | 0.6158 |
| 4.15 | | 408 | 0.8344 | 46.62 | 0.7665 |
| 5.19 | | 494 | 0.4091 | 218.26 | 0.9420 |

Notes: z is depth along the conductor and D is conductor's outside diameter.

*Stiffness Degradation*

The degradation resulting from the cyclic loads, creates a downward ratcheting of the peak reversal soil resistances. The initial step in determining the degradation parameter, $t$ was to normalize the secant stiffnesses at every half cycle, $K_{sec}(N+½)$ by the initial unload soil stiffness $K_{sec}(N=½)$, which is equal to the reduction factor $R_f$ . The parameter $R_f$ is a soil stiffness reduction factor that controls the position and shape of each *P-y* loop. The degradation parameter, $t$ is derived from fits of Eq. 2.7 to the relationship between $R_f$ and number of half cycles. The parameter $R_f$ is

a function of a parameter called the degradation parameter *t*. While $R_f$ describes the stiffness reduction, the rate at which the stiffness degradation occurs is controlled by the degradation parameter *t*. The degradation parameter *t*, is a function of cyclic displacement $\Delta y_{cyc}$, where $\Delta y_{cyc}$ is the absolute displacement change between any two load reversals. To reiterate the idea expressed above, the *t* parameter is required to compute the corresponding $R_f$ and it is a function of cyclic displacement magnitude $\Delta y_{cyc}$ Once a displacement profile is known or assumed, the corresponding *t* parameter to such displacement profile is computed, then $R_f$, corresponding to that displacement profile, can be computed using Eq. 2.7. The quality of the $R_f$ fits varied from excellent to fair as illustrated by Figure 5.6. Figure 5.7 presents the degradation parameter *t* values derived from the model tests (Test 2) along with the $t$-$\Delta y_{cyc}$ relationship selected for the model computations. The reported t parameter thus far has been derived from calibrations to the soft clay dataset.

It is observed that, in intact soil conditions, the stiff clay will experience lesser degradation at a slower rate compared to the soft clay subjected to the same conditions. This implies that the degradation parameter utilized in the analysis for the stiff clay, will be a percentage of that from the soft clay (M1 motions: $t_{\text{stiff clay}} = 0.5 * t_{\text{soft clay}}$, M2 and M3 motions: $t_{\text{stiff clay}} = 0.6 * t_{\text{soft clay}}$). The data comparison between the soft and stiff soils suggest that $t_{\text{stiff clay}}$ could range from 0.5 to $1.0 * t_{\text{soft clay}}$. It was however observed that as the stiff clay experienced more episodes of cyclic motions, its soil structure experiences a greater level of damage and does not recover fully with the rest period. Once M3 motions were applied, the observed degradation behavior was comparable to observations with the soft clay, in the upper region of the conductor. Figure 5.8 shows a comparison of the soft and stiff clay data at depths where subjected to similar displacements.

In summary, the basic model input parameters are shown in Table 5.3. Prior to carrying out the optimized fits, manual curve fits were carried out, which closely matched the *P-y* data. However, considerations given to reproducibility of the process influenced the choice of the optimized curve fitting techniques, described in this Chapter.

**Table 5.3: Input parameters for complete soil-pile interaction model**

| Model Component | Variable | Symbol | SI Units |
|---|---|---|---|
| Pile | Diameter | $D$ | m |
| | Wall thickness | $t$ | m |
| | Length | $L$ | m |
| | Length above mudline | $L_{above}$ | m |
| | Embedded length | $L_{below}$ | m |
| | Elastic modulus | $E$ | kPa |
| | Area moment of inertia | $I$ | $m^4$ |
| Soil | Undrained shear strength | $s_u(z)$ | kPa |
| Initial Excursion | Initial tangent stiffness (Eq. 3.1) | $K_{max}$ | -- |
| | Asymptote parameter (Eq. 3.1) | $f$ | -- |
| | Modified stiffness factor (Eq. 3.5) | $\chi$ | -- |
| Cyclic unload-reload loops | Power law coefficient (Eq. 3.2) | $K_0$ | -- |
| | Power law exponent (Eq. 3.2) | $n$ | -- |
| | Stiffness degradation (Eq. 3.7) | $t$ | -- |

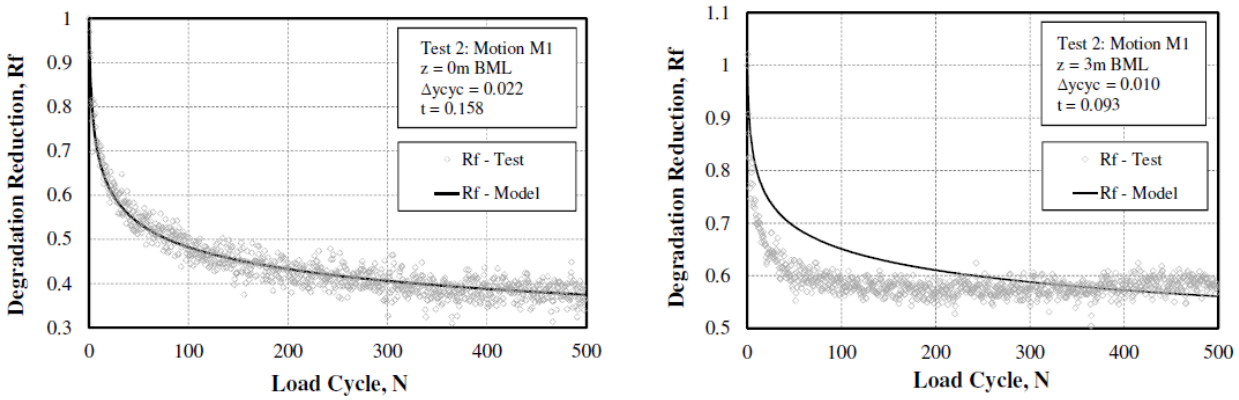


**Figure 5. 6: Excellent $R_f$ fit (left), and fair $R_f$ fit (right) to test 2 M1 data at 0m and 3m BML.**

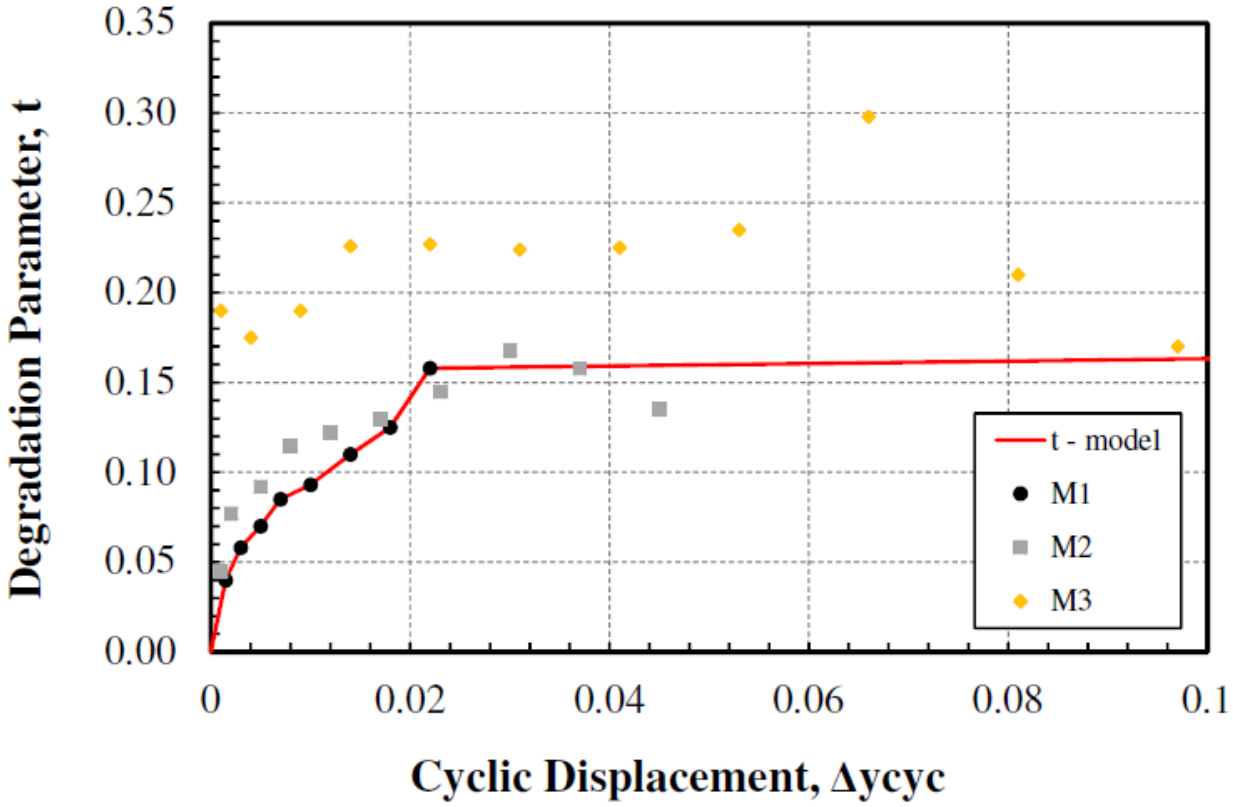


**Figure 5. 7: The relationship between cyclic displacement magnitude Δycyc and degradation parameter t, from test 2 M1, M2, and M3 motions.**

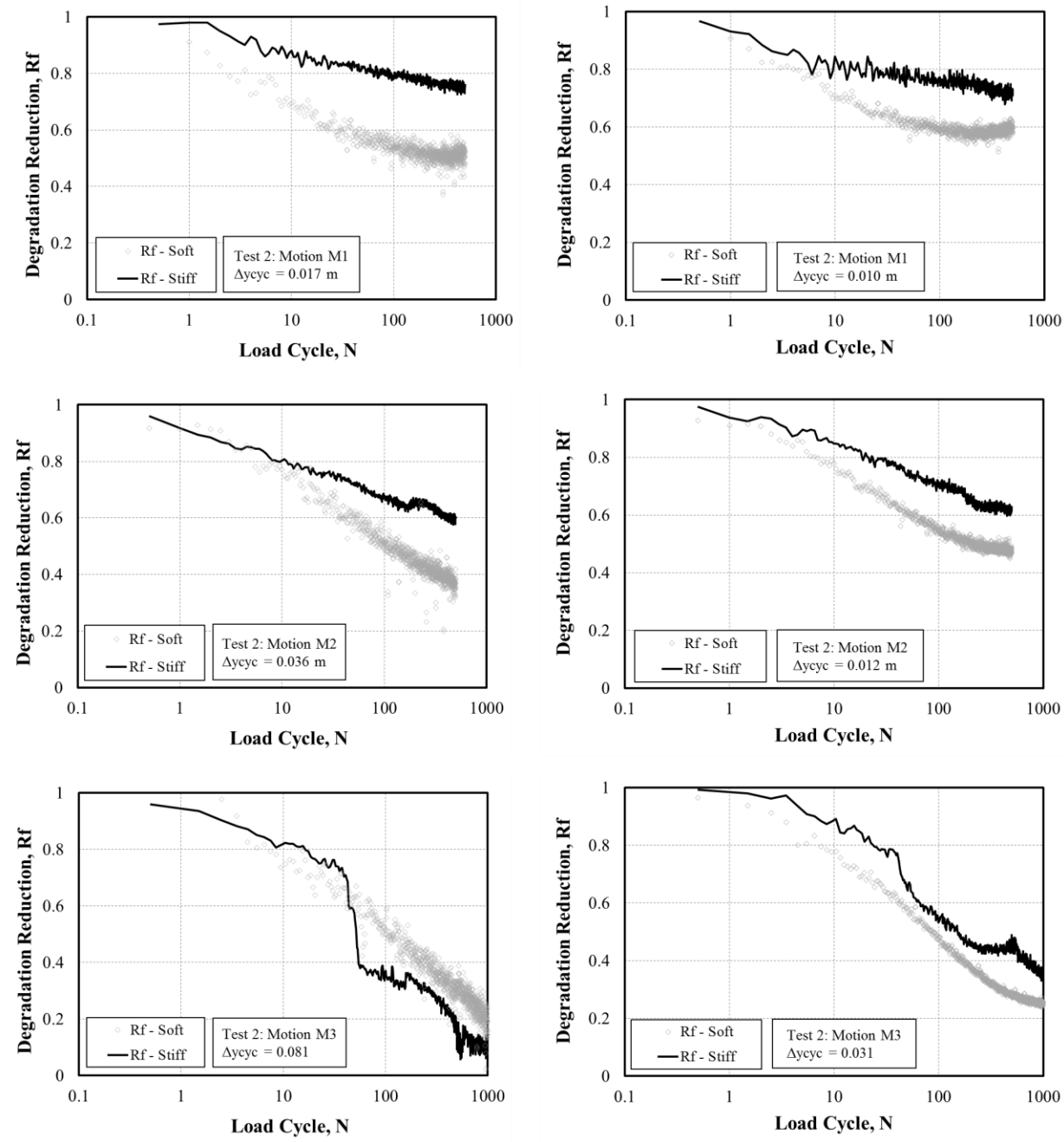


**Figure 5. 8: Comparison of normalized secant stiffness for soft and stiff clays for M1 - M3 motions.**

# CHAPTER VI

# ALTERNATIVE PLASTICITY THEORY FRAMEWORK

The model presented in Chapter III is essentially a phenomenological model, where empirical equations are fitted to experimental data. An alternative approach is to describe permanent deformations under cyclic lateral loads with a framework of plasticity theory. This chapter presents such a framework.

Classical Plasticity theory assumes that there exists an elastic region below a yield surface where elastic behavior occurs; i.e. upon unloading the material returns to its original undeformed configuration. However, if the material is loaded from a stress state on the yield surface, subsequent unloading will not return it to its initial configuration; i.e. permanent deformation occurs. These permanent deformations are effects of factors which depend on the type of soil, its formation process, and geologic history. This could be a result of rearrangement in the fabric structure of the soils, and possibly crushing of particles. The process of yielding redefines the size, shape, and/or location of the yield surface, and is a function of the stress and/or strain history. The plasticity formulations have also been used to describe P-y spring behavior. Bounding surface plasticity has been used by a number of researchers to describe material behavior under loading (examples include, Krieg, 1975; Dafalias, 1986; McCarron, 2015; Choi et al. 2015). The central element in the plasticity theory is the yield condition, which is the relationship among stress components of which incipient yield occurs.

## Yield Surface

Generally, a yield function will be chosen to describe the yield surface. The yield surface, denoted by $f(\sigma) = 0$, describes the locus of stress states at which permanent deformations occur. As plastic deformation occurs, a hardening rule is needed to describe the material behavior with the plastic loading applied. One plasticity model widely considered for P-y analysis is the multi-surface bounding surface plasticity. In these models, there are typically 2 surfaces, the yield surface and the bounding surface.

## Hardening Rule

The hardening rule describes how the yield surface changes with plastic loading. The hardening rule can be isotropic, kinematic, or mixed hardening (a combination of isotropic and kinematic hardening rules). In isotropic hardening, the position and shape of the yield surface remains fixed, however, the size of the yield surface expands symmetrically in stress space, with plastic deformation. By contrast, kinematic hardening denotes a condition where the size of the yield surface does not change, but the surface translates about in the stress space. The hardening parameters help describe of how the size, shape, and current yield surface varies as plastic loading progresses.

## Application to Soil Springs

In the case of a plasticity model for lateral soil springs, the analysis reduces to a one-dimensional model. The ultimate limit state under monotonic loading is defined by a bounding surface parameter $P_y$. In the case of a purely kinematic hardening model, $P_y$ is constant. The yield

surface will be a function of some state variable (stress, soil resistance etc.), and hardening parameter, and possibly a record and tracking of the state variable at the center of the elastic region.

$$f\left(P_i - P_\alpha\,,\ P_y\right) = 0 \qquad \text{Eq. 6.1}$$

$P_i$ will be the state variable (current soil resistance), $P_\alpha$ the record of the state variable at the center of the elastic region, and $P_y$ controls the size of the yield surface. Various formulations have been prescribed depending on the type of problem being solved.

*Bounding Surface Plasticity Model*

The bounding surface plasticity model proposed by Choi et al. (2015), presented a plasticity model for uniaxial loading in sand. The framework of this model was applied in the plasticity model for clays employed in this study. The model employs four (4 parameters) at a given depth along the depth of the pile or conductor. The bounding surface plasticity soil spring model could be formulated to have several level of components to describe specific behavior expected in the loaded soil. These components could include but not limited to:

a) Elastic-plastic bounding surface component
b) Viscous component
c) Damage component
d) Gapping component

Within the scope of this study, the Elastic-plastic bounding surface and damage components were incorporated. The components of the constitutive model are shown and described below.

*The elastic constitutive law is modelled with Eq. 6.2a*

The elastic constitutive law simply shows the relationship between the elastic displacement rate, proportional to the incremental soil-resistance.

$$\dot{P} = K_e \dot{y}_e = K_e \left(\dot{y} - \dot{y}_p\right) \quad \text{Eq. 6.2a}$$

where,

$K_e$ is the elastic modulus

$\dot{y}$ is the total displacement increment

$\dot{y_p}$ is the plastic displacement increment

$\dot{P}$ is the computed incremental soil-resistance

The elastic modulus is presented in Eq.6.2b based on the corrections presented by Choi et al. (2016) in an erratum accompanying the publication in 2015 (Choi et al., 2015), which incorporates both the elatic modulus of the pile material and elastic modulus of the soil.

$$K_e = 1.67 * E_s * \left[\frac{E_p}{E_s}\right]^{-(0.053)} \quad \text{Eq. 6.2b}$$

Where,

$E_p$ is the elastic modulus of the pile material

$E_s$ is the elastic modulus of the soil

The elastic modulus of the soil is computed with the shear modulus of the soil which can be measured in the laboratory or field. It can also be estimated through existing correlations. However when using correlations to estimate the shear wave velocity attention should be paid to the source of data the correlations are based upon.

$$E_s = 2 * \rho * V_s^{\,2} * (1 + \mu) \quad \text{Eq. 6.2c}$$

Where,

ρ the mass density of the soil

$V_s$ is the shear wave velocity

μ is the soil Poisson's ratio

Below is an expression for shear wave velocity that has been adopted in this model's frame work. When choosing the formulation to use for the shear wave velocity, the type of soil (sand, soft clay, or stiff cay), and condition (intact or fissured) of the soil needs to be considered. The formulation for shear wave velocity in clays presented in Eq. 6.2d was proposed by Taboada et al. (2013). It is important to note that the empirical formulation presented is great if the soil properties and conditions are similar to those in the sample database used for the correlation. There can also be shear wave velocity profiles generated based on field and laboratory data measurements, instead of empirical correlations where possible.

$$V_s = 31\ (s_u)^{0.414} \qquad \text{Eq. 6.2d}$$

Where,

$s_u$ is the undrained shear strength of the soil

*The yield function (f) defining the yield surface in Eq. 6.3a*

$$f = |P - P_\alpha| - P_{yield} \quad \text{Eq. 6.3a}$$

$$P_{yield} = K_e * y_{yield} \quad \text{Eq. 6.3b}$$

$$y_{yield} = \frac{2.5 * D * \gamma_{yield}}{(1+\mu)} \quad \text{Eq. 6.3c}$$

Where,

$P_\alpha$ is the value of P at the center of the elastic region (generally referred to as back stress)

$P_{yield}$ defines the size of the elastic region (the extent of the yield surface)

*Plastic modulus ($K_p$) definition shown in Eq. 6.4a*

$$K_p = C * K_e * \frac{|(P_{ult} * sign(\dot{y})) - P|}{|P - P_{in}|} \quad \text{Eq. 6.4a}$$

$$C = A \frac{(P_{ult} - P_{yield})[\ln(P_{ult} - P_{yield}) - \ln(P_{ult})] + P_{ult}[\ln(2) - 0.5] + P_{yield}[1 - \ln(2)]}{K^e y_{50} - 0.5 P_{ult}} \quad \text{Eq. 6.4b}$$

Where,

$P_{ult}$ defines the size of the bounding surface.

$P_{in}$ defines the onset of plastic loading during current cycle

*C* is a plastic deformation parameter

*Dam* is a damage parameter

*A* is a scaling factor which is incorporated to the formulation presented by Choi et al., 2015 to match the interpreted P-y curves from the test program presented in Chapter IV. It could change with the loading condition and cyclic displacement magnitude. A value of 9 was used in this study for soft clays. A value could range between 1 and 10.

$y_{50} = 2.5 * \varepsilon_{50} * D$

$$P_{ult} = N_p * s_u * D$$ Eq. 6.4c

Where,

$N_p$ is the ultimate bearing or resistance factor

$D$ is the pile diameter

*Kinematic hardening law*

$$\dot{P}_\alpha = K_p * \dot{y}_p$$ Eq. 6.5

Where,

$K_p$ is the plastic modulus

*Tangent elasto-plastic damage stiffness*

The basic tangent elasto-plastic stiffness is given by the relationship between the elastic and plastic stiffness shown in Eq. 6.6.

$$K = \frac{\dot{P}}{\dot{y}} = \frac{K_p * K_e}{K_p + K_e} * R_f$$ Eq. 6.6

$R_f$ is a degradation parameter

The degradation parameter was used to account for damage on the tangent elasto-plastic stiffness. The incorporation of this damage formulation helps take into account the stiffness softening behavior, which could be modified with further rigourous analysis, studies, and calibrations. The degradation law applied in the empirical model was again utilized here (refer to Eq. 3.7). The only difference is the tangent displacements where used instead of the cyclic displacements.

# CHAPTER VII

# RESULTS

Simulation of the *P-y* response of the cyclically laterally loaded soil has been captured using the models described in the preceding sections. This section presents the results obtained and discusses the performance and limitations of the presented models. The phenomenological model introduced in Chapter III, was calibrated with the centrifuge harmonic motion test data presented in Chapter IV. The calibrated model was then utilized in computing bending moments which is compared to the harmonic motion bending moments, in what is referred here as the reverse analysis. The model was also used in predicting bending moments from the random motions. The reverse analysis is achieved by solving the fourth-order ordinary differential equation, which governs the pile-soil interaction problem shown in Eq. 7.1, through a finite difference scheme. Where the secant stiffness $K_{sec}$ is derived from the cyclic *P-y* curves as presented earlier, in Chapter V. The relationships commonly used in Piles subjected to flexural bending problem is shown in Table 7.1 and Figure 7.1. Appendix C shows the finite difference interpretation of Eq. 7.1. This was solved numerically utilizing a series of connected scripts and functions written in MATLAB.

$$EI\ \frac{d^4(\Delta y)}{dz^4} + K_{sec}(\Delta y) = 0 \qquad \text{Eq. 7.1}$$

**Table 7.1: Relationships commonly used for piles subjected to bending motions.**

| Variable | Formula | Units |
|---|---|---|
| Distance along the length of Pile (measured from the pile head) | z | [L] |
| Deflection | y | [L] |
| Distance from exterior bending surface to the neutral axis (centroid), within the pile cross-section | x | [L] |
| Slope or Rotation of Pile section | $\phi = \frac{dy}{dz}$ | [Dimensionless] |
| Curvature | $c = \frac{d^2y}{dz^2}$ | [Radians / L] |
| Bending Moment | $M = EI \frac{d^2y}{dz^2}$ | [F * L]] |
| Shear Force | $V = EI \frac{d^3y}{dz^3}$ | [F] |
| Soil Reaction | $P = EI \frac{d^4y}{dz^4}$ | [F / L] |

E = Elastic modulus / young modulus of Pile material

I = Moment of inertia of pile section with respect to the neutral axis

EI = Flexural Stiffness of the Pile

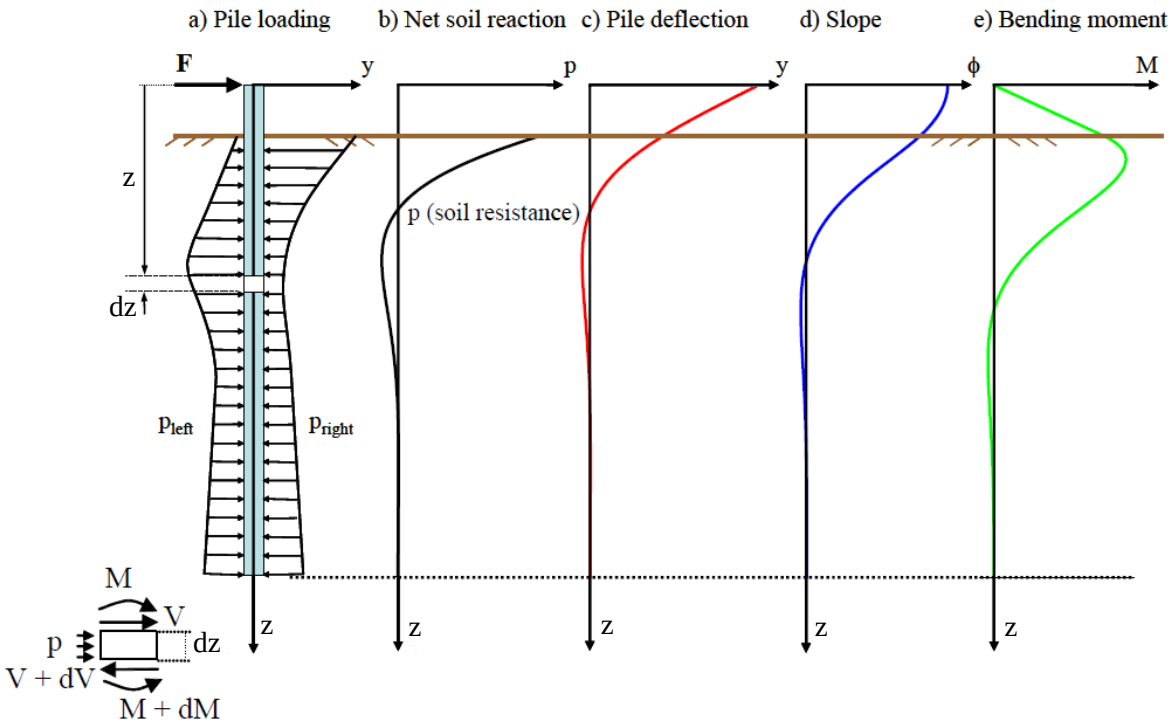


**Figure 7. 1: Relationships between pile in flexure variables.**

The model achieves a good match between the test and model computed cyclic bending moment profile. The variation between model computation and measurements for maximum cyclic moment and its location along the conductor/pile depth, yielded a maximum percentage difference of approximately 20% or less. In principle, the back-calculated bending moment profile should match the measured bending moment profile from which the *P-y* curves were developed, but comparisons could show deviations between predictions and measurements that can be significant. Possible sources of numerical and experimental errors include, uncertainties in soil strength profile, zeroing errors, the smoothing function fit to discrete data, and extensive data reductions involving numerical differentiation and integration. The net effect of such errors can be evaluated by performing a reverse analysis, by carrying out a soil-pile interaction analysis using the soil-

spring model described in preceding Chapters. Imposing pile head displacements identical to those imposed during a model test should produce ‘computed’ bending moment profiles identical to the measured bending moment profile.

The general framework for this model is easily applicable to industry applications, ranging from offshore oil and gas conductors, to offshore piles for platforms, and offshore wind turbines, since they experience fatigue stresses from the cyclic loads to which they are subjected. To recap, the model was calibrated to the harmonic motions (Test 2 (C2): M1, M2, M3 motions; Test 3 (C3): M1, M2, M3 motions), afterwards used to make predictions for random and transient motions. The focus is prediction of cyclic moments that are most relevant to fatigue life analysis (small load displacement range), although some consideration is also given to absolute min and max moment magnitudes

## Phenomenological Model

### *P-y Curves*

The *P-y* curves comprising of the initial excursion curve and the cyclic *P-y* curves, compared reasonably well between model and test results. It should be recalled that the calibrations were based the initial excursion curve, and the first unload half cycle, while the remaining cycles were determined through implementation of the degradation law. As expected, the initial excursion segment and the first cycle of the *P-y* curves showed excellent agreement with the model results derived from the fit parameters. Subsequent cycles, produced varied comparisons between model and test results. The test P-y curves sometimes shows less degradation on the reload segments compared to the unload (an example is C2 M1 P-y curve for soft clay at 5 m depth BML, see Figure 7.2a, whereas the model results show similar degradation on the reload as observed on the

unload curves. It is expected that downward ratcheting will occur in P-y space for a displacement-controlled test. It is unclear why the result from the test does not exhibit this expected trend. This could be one reason for the observed difference in the bending moment profiles, however, it is understood that there are many complex changes occurring in the soil along the depths of the pile. As the pile head displacement magnitudes increases (for M2 and M3 motion), better resolution is possible in terms of mobilized soil resistances, resulting in improved comparisons between model and measured *P-y* curves. This also results in the cyclic *P-y* curves starting to deviate from the power law trend, especially at shallow depths close to the mudline, reasons for this is not clear, however, the occurrence of gapping or high plastic behavior, might be the reason for the shape deviations observed. Figure 7.2a and 7.2b presents results of measured and model prediction for C2 M1 *P-y* curves up until depths where P-y data were extractable, for the first and final cycles ($N$ = 499 for C2 and $N$ = 999 for C3). The green line and/or symbols show results and data for cycle 1, and the red for the last cycle. Figure 7.2a presents results for the soft clay, while Figure 7.2b, the results for the stiff clay. The remaining P-y curves are presented in Appendix D.

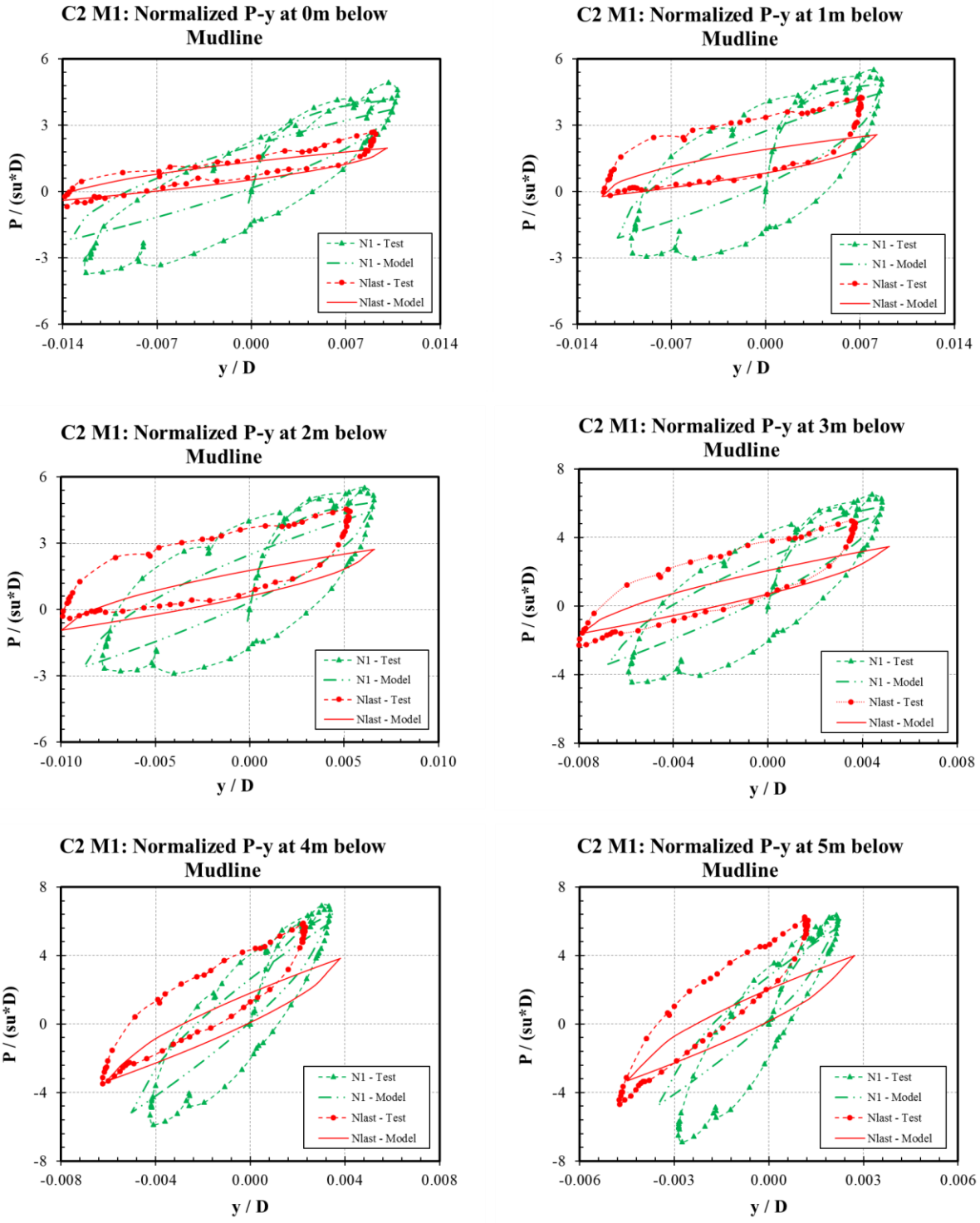


**Figure 7. 2 a: Cyclic P-y curves for test 2 M1 motion in soft clay soil for cycle 1 and cycle 499 (last cycle).**

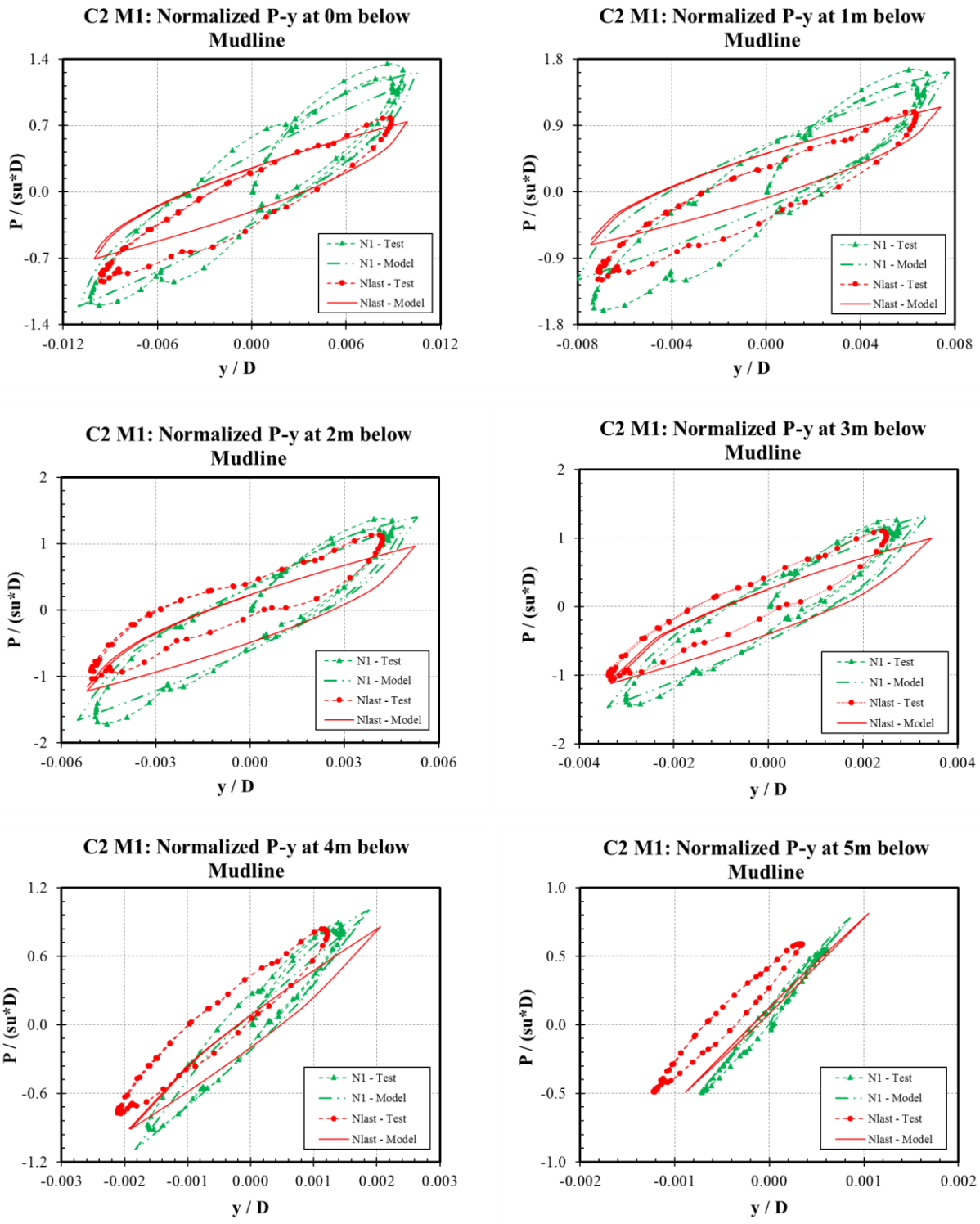


**Figure 7. 2 b: Cyclic P-y curves for test 2 M1 motion in stiff clay soil for cycle 1 and cycle 999 (last cycle).**

*Bending Moment*

The displacements are computed after generating the soil stiffness matrix and the load matrix. Through an iterative process, the displacement profile is optimized, with a tight error tolerance of 1E-10 between iterations on computed bending moments. The bending moment profile is generated through a second-order finite difference approximation of the displacement profile multiplied by (*E.I*). This is presented in Appendix C.

The match between the bending moment fits and test bending moments were reasonably close. Particularly important for fatigue analysis, is the cyclic moments profile derived from the maximum reversal moment profile, and minimum reversal moment profile. This is essential in computing the cyclic stresses required in fatigue analysis of conductors or piles. The depth of occurrence of the maximum cyclic bending moment along the pile was also compared to that from the test bending moment profiles.

The region along the pile depth where the maximum bending moment occurs is dependent on the pile head displacement magnitude. For the load range considered in this study, it occurred generally within 2 m to 12 m BML. Figure 7.3 shows the C2 M1 (Test 2, Motion 1) model results obtained for the cyclic moments which are generally in good agreement with the measured cyclic moments. Other results of the bending moments, are presented in Appendix E. Figure 7.3a shows the results for the soft clay and Figure 7.3b, the results for the stiff clays. These results present the bending moment profiles for the first cycle, the last cycle, and an intermediate cycle (N=300 or N = 500, whichever applies). In all cases considered, the differences between model and measurement maximum bending moment, do not exceed 20%. For $N$ = 1, the model adequately reproduces the test results, while for subsequent cycles, the model estimates are typically low during reload and high during unloading. These average out in the cyclic bending moment profiles.

The error computations are shown in Figure 7.4a, for the soft clay soil, and 7.4b, for the stiff clay soil.

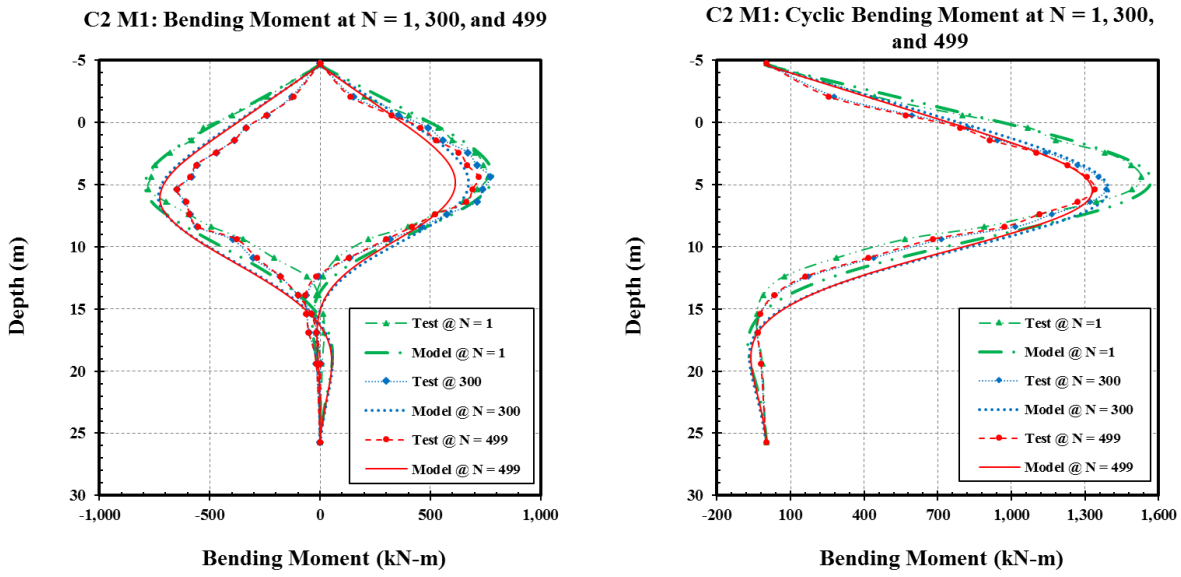


**Figure 7. 3 a: Cyclic bending moments for soft clay for test 1 motion 1 at cycles 1, 300, and 499.**

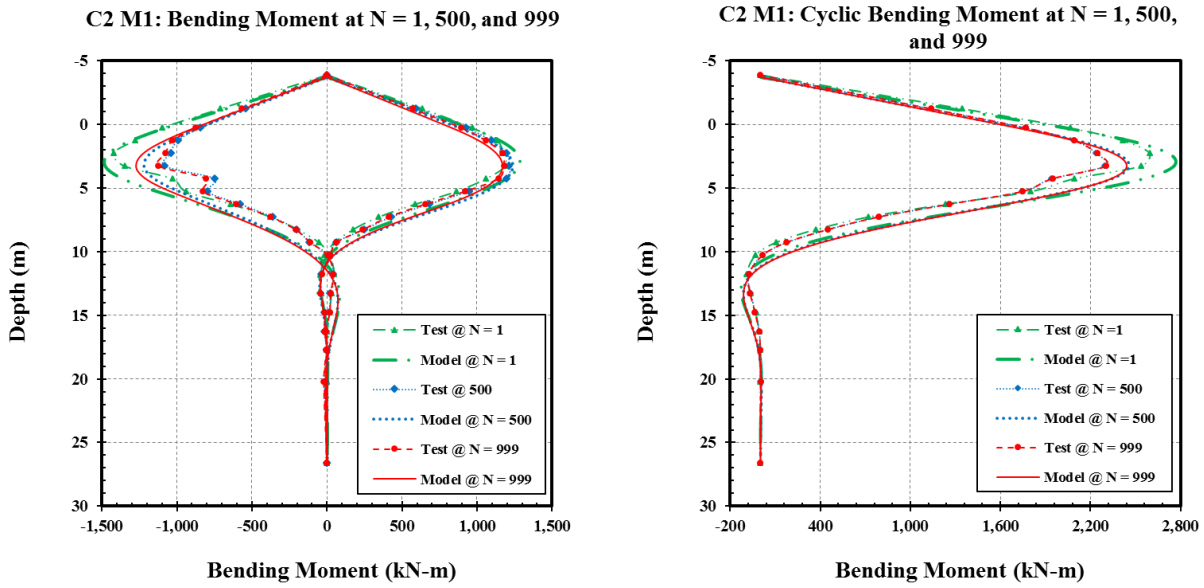


**Figure 7. 3 b: Cyclic bending moments for stiff clay for test 1 motion 1 at cycles 1, 500, and 999.**

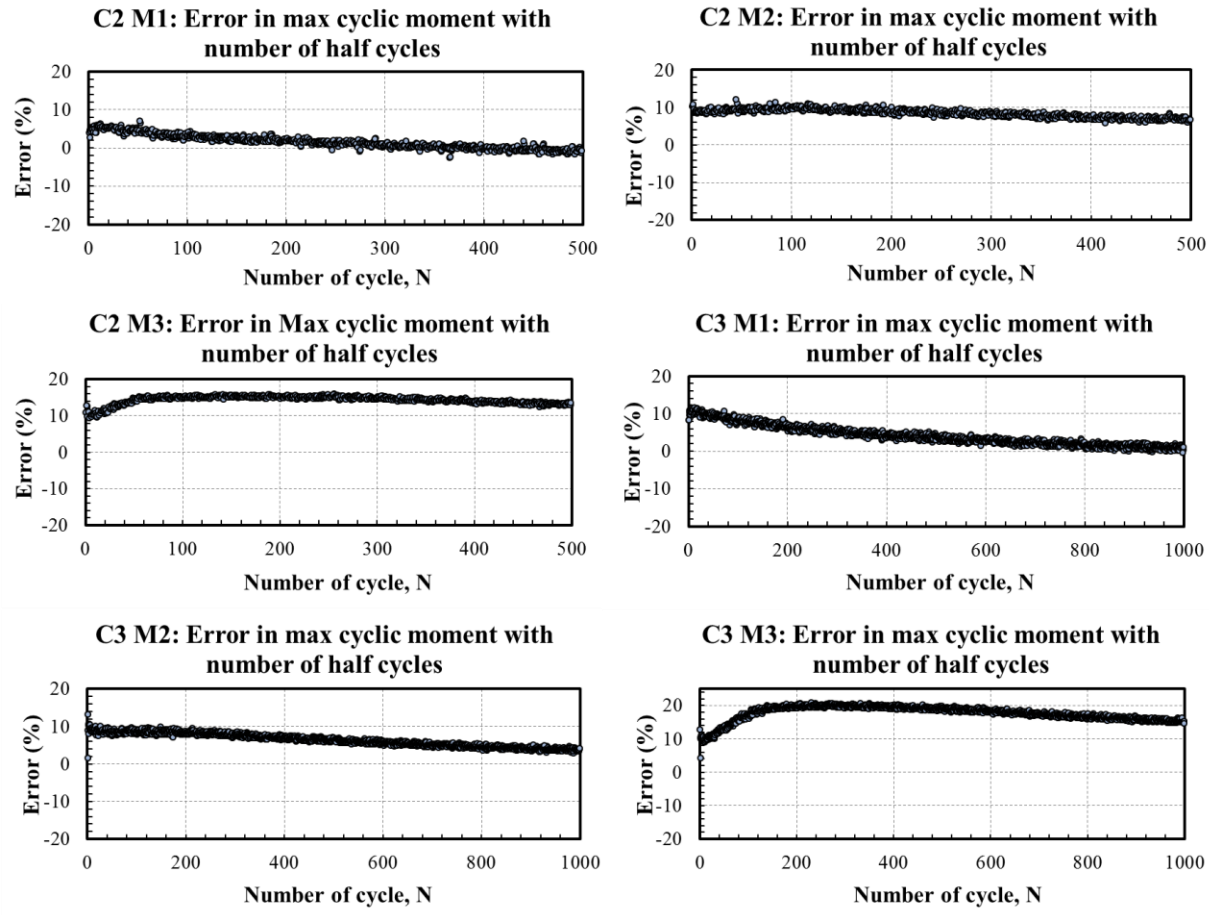


**Figure 7. 4 a: Error computations for maximum bending moment difference between test and model computations for the soft clay soil.**

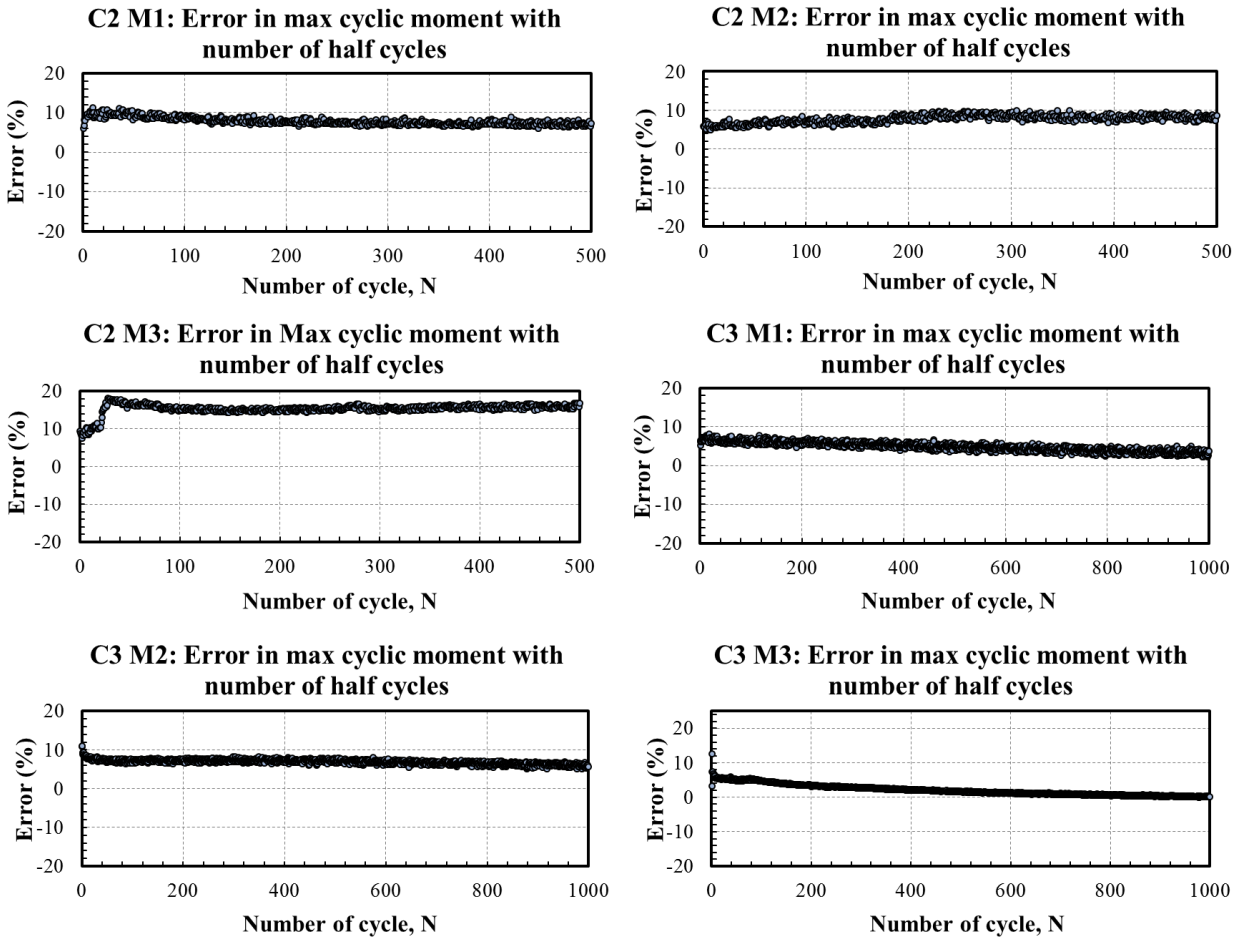


**Figure 7. 4 b: Error computations for maximum bending moment difference between test and model computations for the stiff clay soil.**

*Model Validation*

A particularly demanding test on the model is that of random loading, as it requires implementation of the stiffness degradation laws (Eqs. 3.6 and 3.7, Figure 5.7) and model parameters under irregular loading conditions for which the model was not calibrated. It is noted that the random loading in Test 4 (C4) centrifuge tests comprised 100 recurring load packets, with a repeated random load sequence applied within each packet. Figure 7.5 – Figure 7.8, show model predictions versus measured values of cyclic bending moments for packets 1, 20, 50, and 100

(packet 1 represents the first of the repeated load sequence, while packet 100, is the last repeated load sequence of the repetitive random loads). The figures show the profiles of absolute bending moment at reversals (max unload and reload), and cyclic bending moment (i.e., the change in bending moment occurring during the trough to peak displacement motion) corresponding to the first instance of cyclic displacement $\Delta y$ occurring within a specified range with a selected packet for Test C4 M1 and C4 M2 motions. Pile response is shown for four ranges of cyclic displacement for soft clay soil: Range 1, $\Delta y > 0.06$ m; Range 2, 0.06 m $\leq \Delta y < 0.04$ m; Range 3, 0.04 m $\leq \Delta y <$ 0.02 m; and Range 4, 0.02 m $\leq \Delta y < 0.00$ m. For the stiff clay soils the ranges are: Range 1, $\Delta y >$ 0.08 m; Range 2, 0.08 m $\leq \Delta y < 0.06$ m; Range 3, 0.06 m $\leq \Delta y < 0.04$ m; and Range 4, 0.04 m $\leq$ $\Delta y < 0.00$ m. Figure 7.5 - Figure 7.8 shows the result using parameters from C2M3 and C3M3, for the displacement ranges (Range 1 – 4) shown. The exact displacement corresponding to the first cycle, within each load packet is not exactly the same, considering that these are random motions, however, falls within the ranges shown above.

The model computation results were compared to the random test results from the same testing program. This was done in a bid to evaluate how the model works for conditions different from which the model was calibrated to, and evaluate its performance with conditions not exactly that it was calibrated and formulated from. The model was not calibrated to the random test data. The results of these are presented in Figure 7.5 a-d, for the soft clay soil subjected to M1 motions on conductor 4 (C4), and Figure 7.6 a-d for the soft clay soil subjected to M2 motions on conductor 4 (C4). Figure 7.7 a-d, presents the results for the stiff clay soil subjected to M1 motions on conductor 4 (C4), while Figure 7.8 a-d presents the results for the stiff clay soil subjected to M2 motions on conductor 4 (C4). To further evaluate the capability of this phenomenological model an attempt was made to reproduce the results presented by Zhang et al. (2017) with the

displacement limits considered for this study. Figure 7.9 shows the comparisons between the model computation and the results presented by Zhang et al. (2017). Even though the pile diameter is beyond what this model was calibrated to, the results compared pretty impressively within the limits of the pile head displacement this model was calibrated to. The results presented in here where carried out using C2 M1 test calibrated parameters. The results presented in Zhang et al. (2017) were generated from load-controlled simulations. However, since the model was built as a displacement control model, the pile head displacement presented in Zhang et al. (2017) was utilized as the load control at the pile head. The generated displacement, bending moment and shear force profiles along the depth of the pile utilizing the soil-springs from the presented empirical model, were compared to the results presented in Zhang et al. (2017) and presented in Figure 7.9.

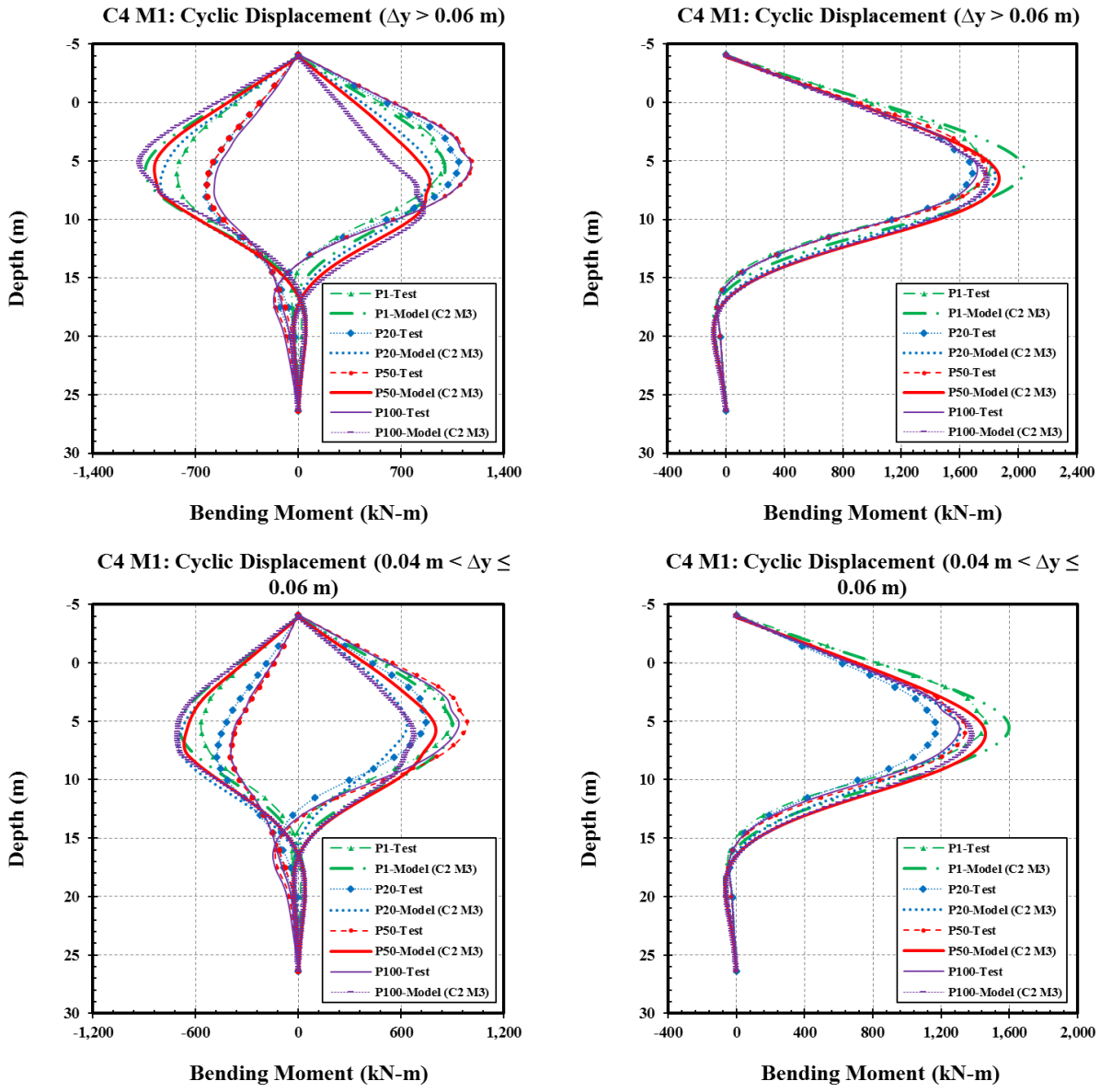


**Figure 7. 5 a: Model bending moment using parameter from C2M3 comparison to C4M1 (random motion) for cyclic displacements greater than 0.04 m for soft clay soil.**

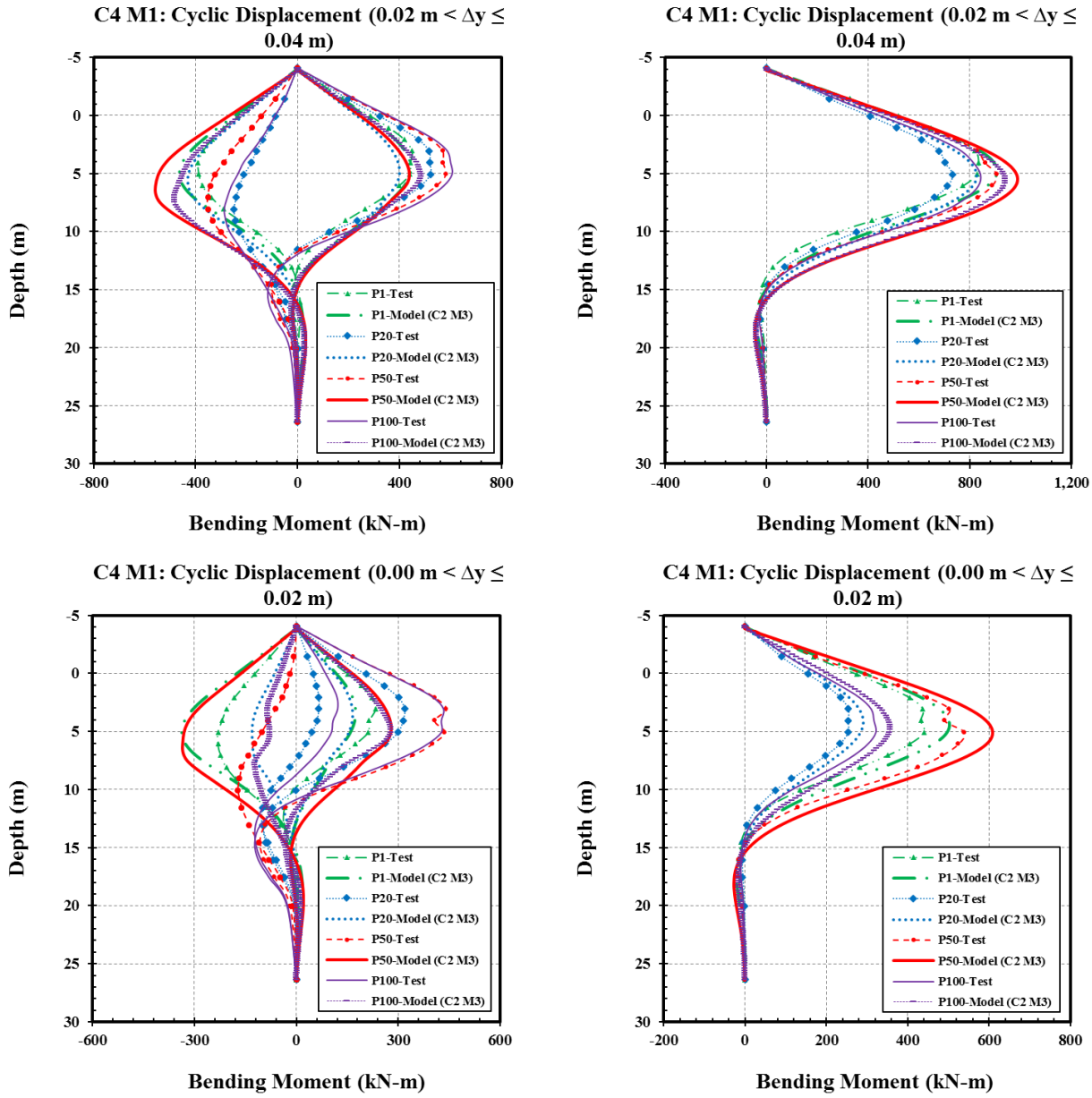


**Figure 7. 5 b: Model bending moment using parameter from C2M3 comparison to C4M1 (random motion) for cyclic displacements lesser than or equal 0.04 m for soft clay soil.**

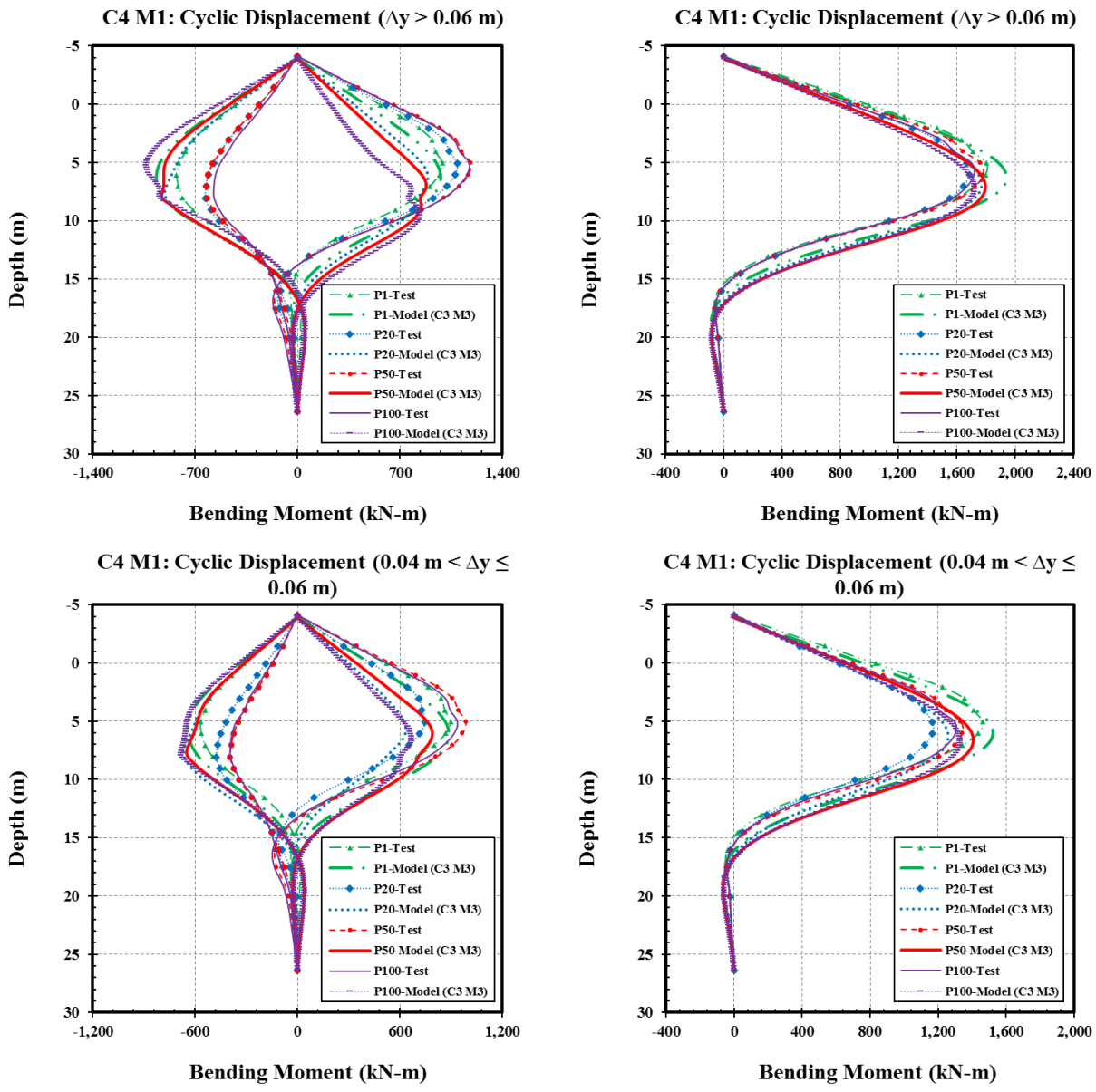


**Figure 7. 5 c: Model bending moment using parameter from C3M3 comparison to C4M1 (random motion) for cyclic displacements greater than 0.04 m for soft clay soil.**

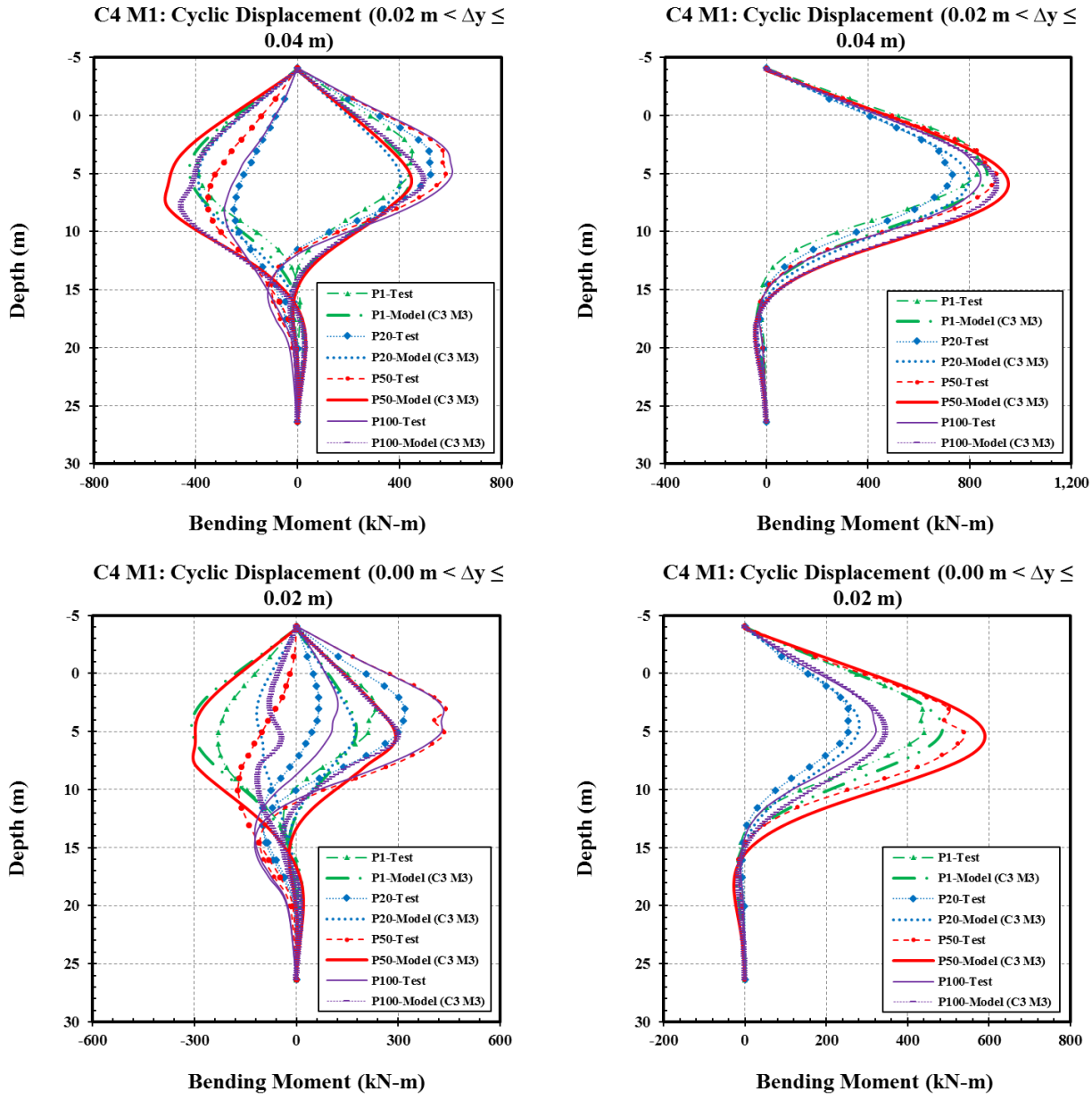


**Figure 7. 5 d: Model bending moment using parameter from C3M3 comparison to C4M1 (random motion) for cyclic displacements lesser than or equal 0.04 m for soft clay soil.**

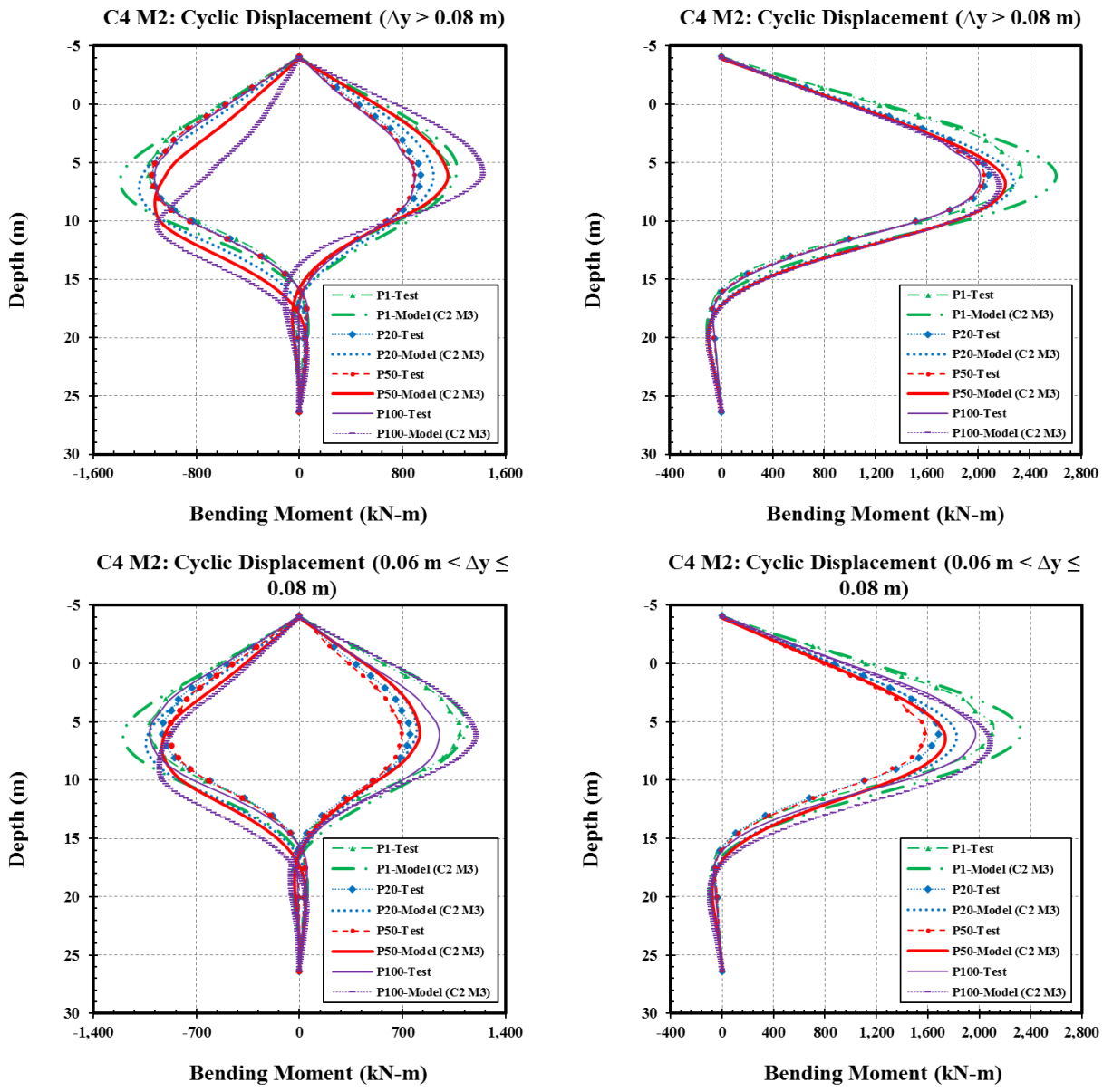


**Figure 7. 6 a: Model bending moment using parameter from C2M3 comparison to C4M2 (random motion) for cyclic displacements greater than 0.06 m for soft clay soil.**

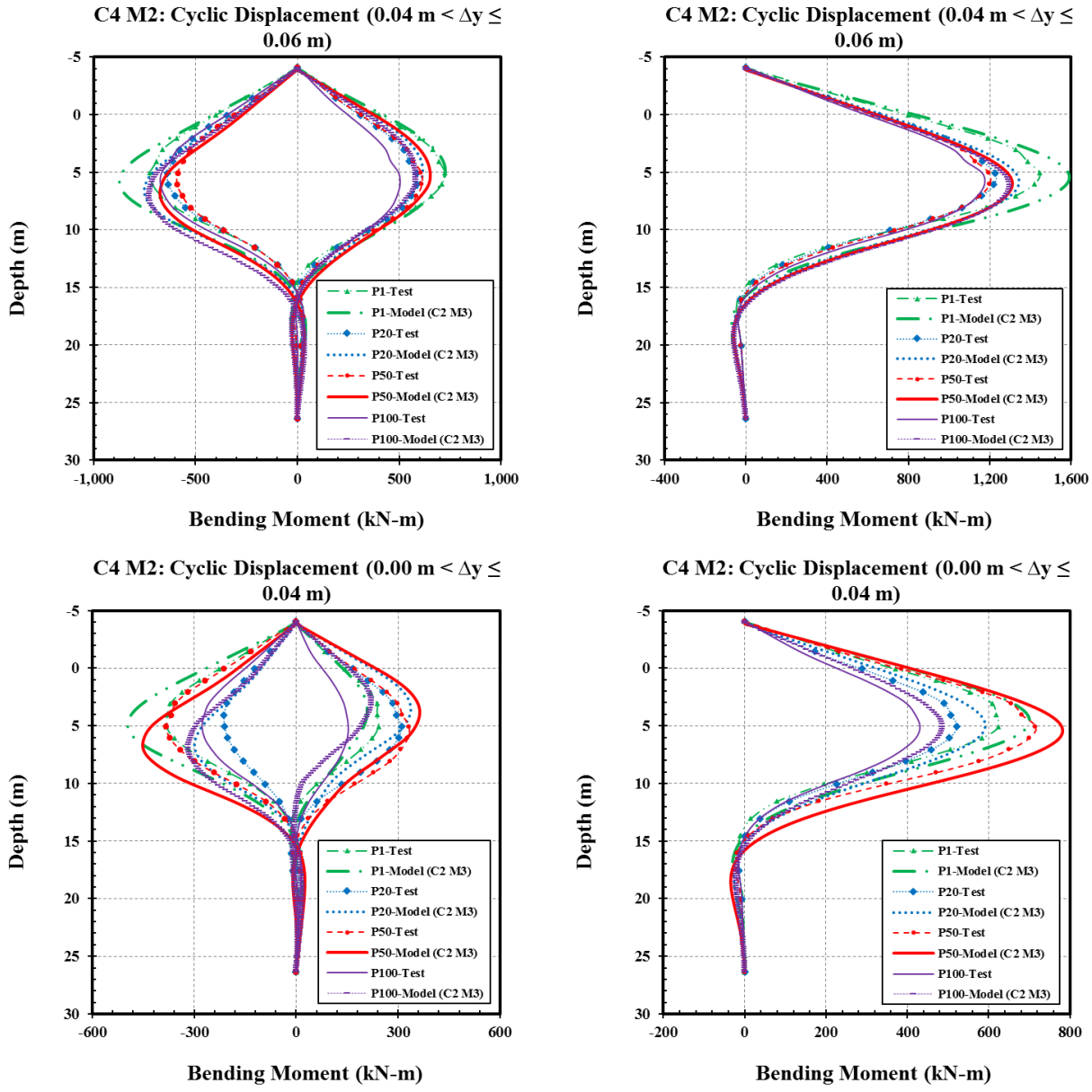


**Figure 7. 6 b: Model bending moment using parameter from C2M3 comparison to C4M2 (random motion) for cyclic displacements lesser than or equal 0.06 m for soft clay soil.**

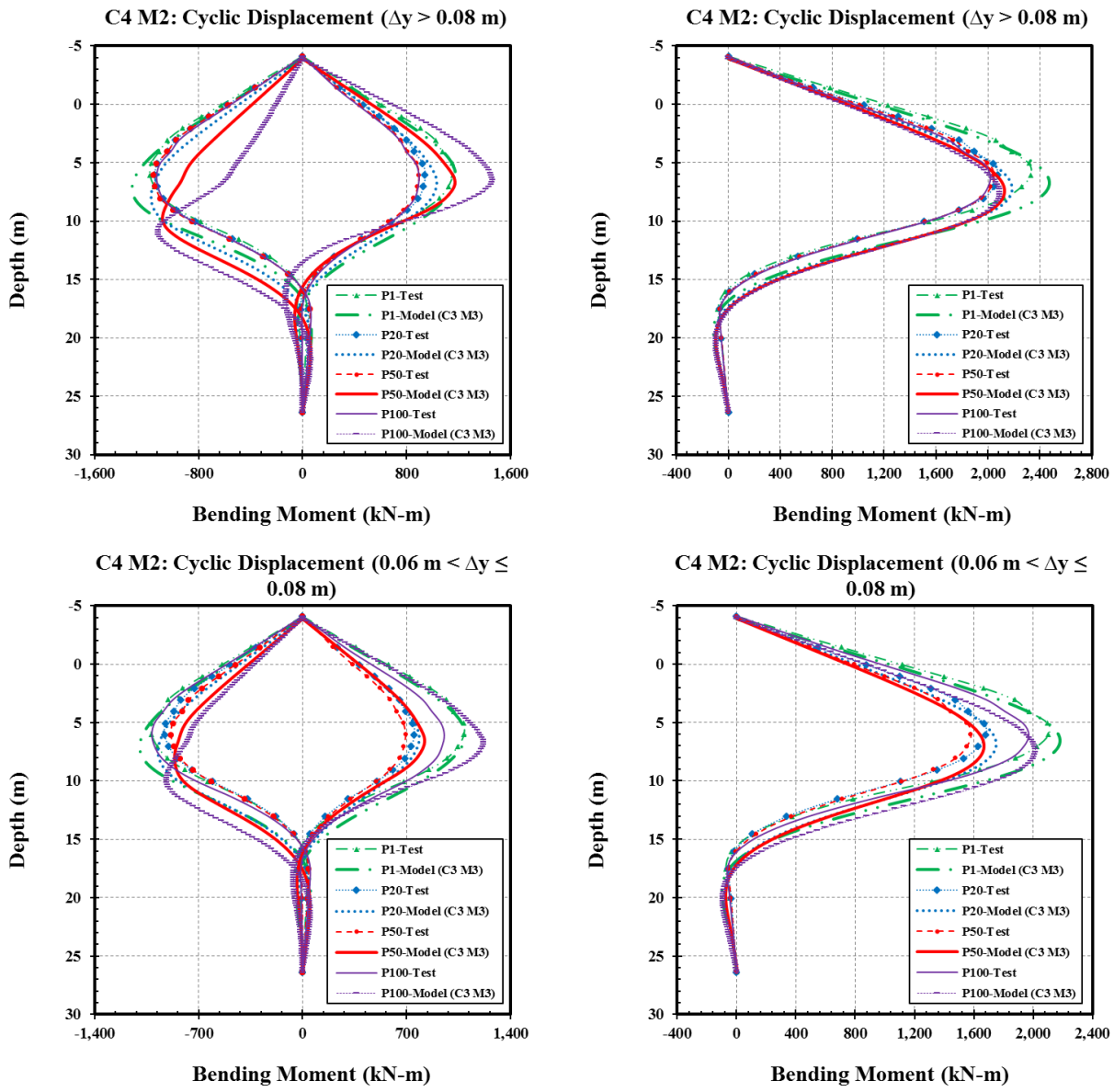


**Figure 7. 6 c: Model bending moment using parameter from C3M3 comparison to C4M2 (random motion) for cyclic displacements greater than 0.06 m for soft clay soil.**

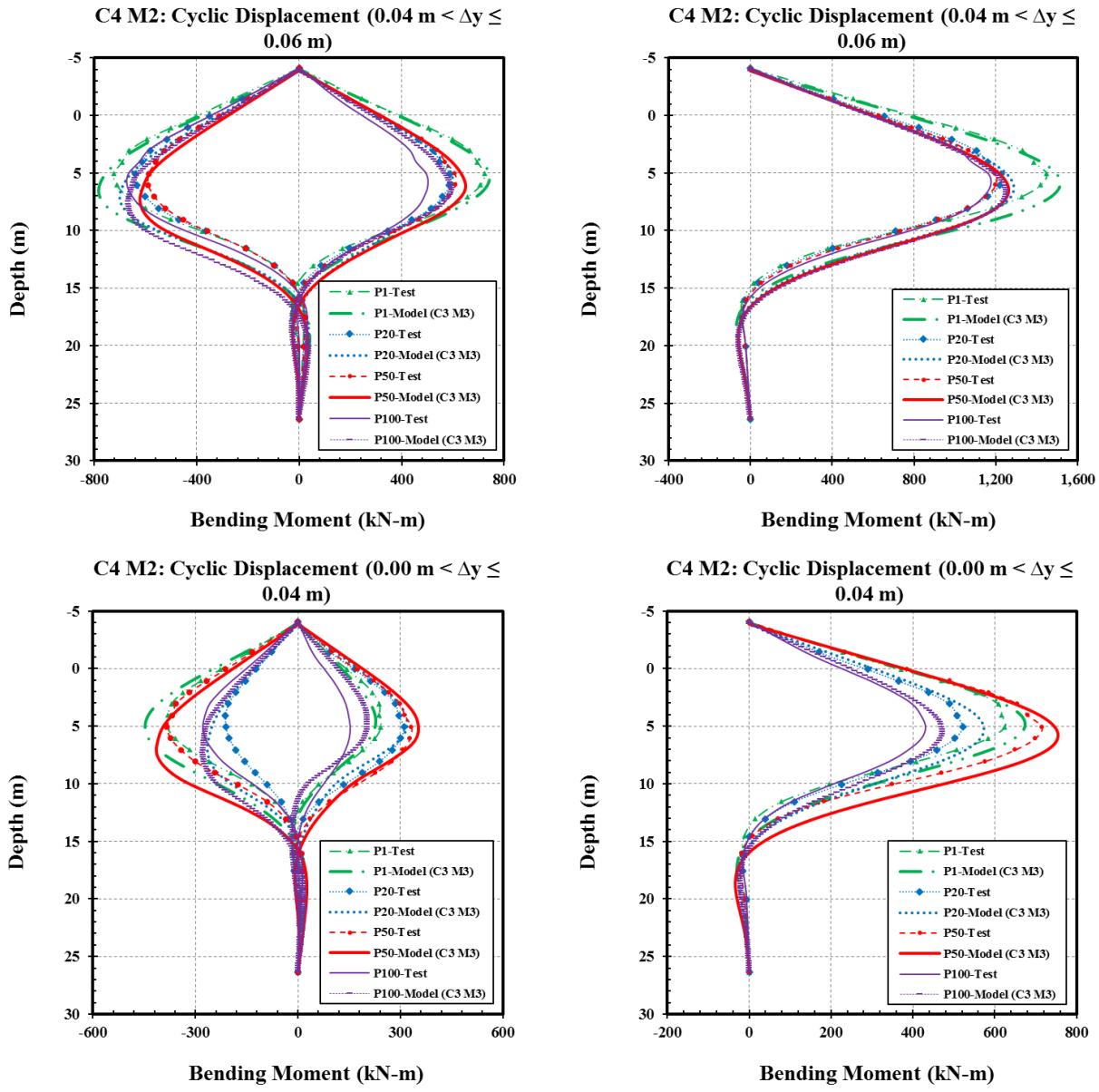


**Figure 7. 6 d: Model bending moment using parameter from C3M3 comparison to C4M2 (random motion) for cyclic displacements lesser than or equal 0.06 m for soft clay soil.**

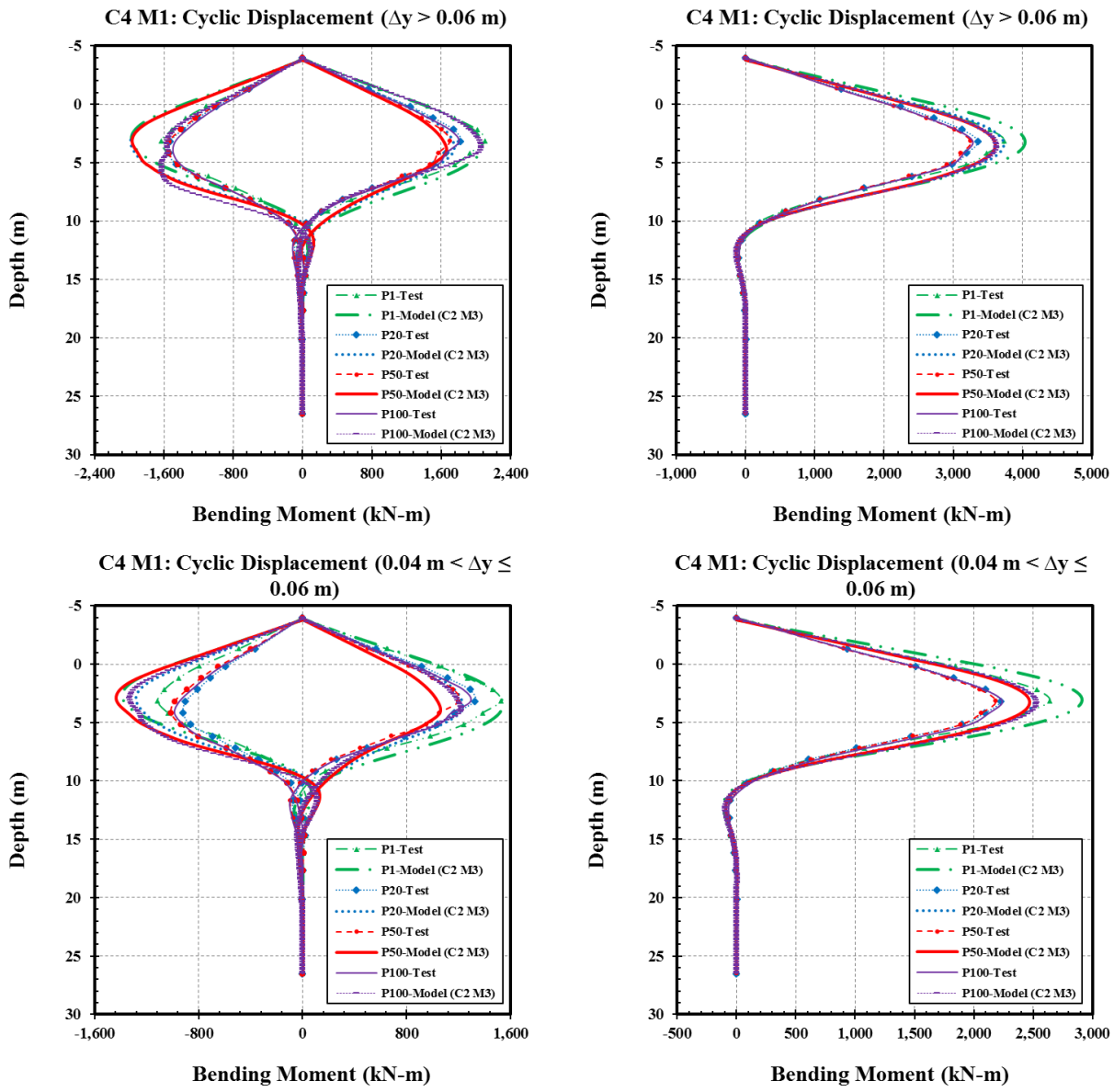


**Figure 7. 7 a: Model bending moment using parameter from C2M3 comparison to C4M1 (random motion) for cyclic displacements greater than 0.04 m for stiff clay soil.**

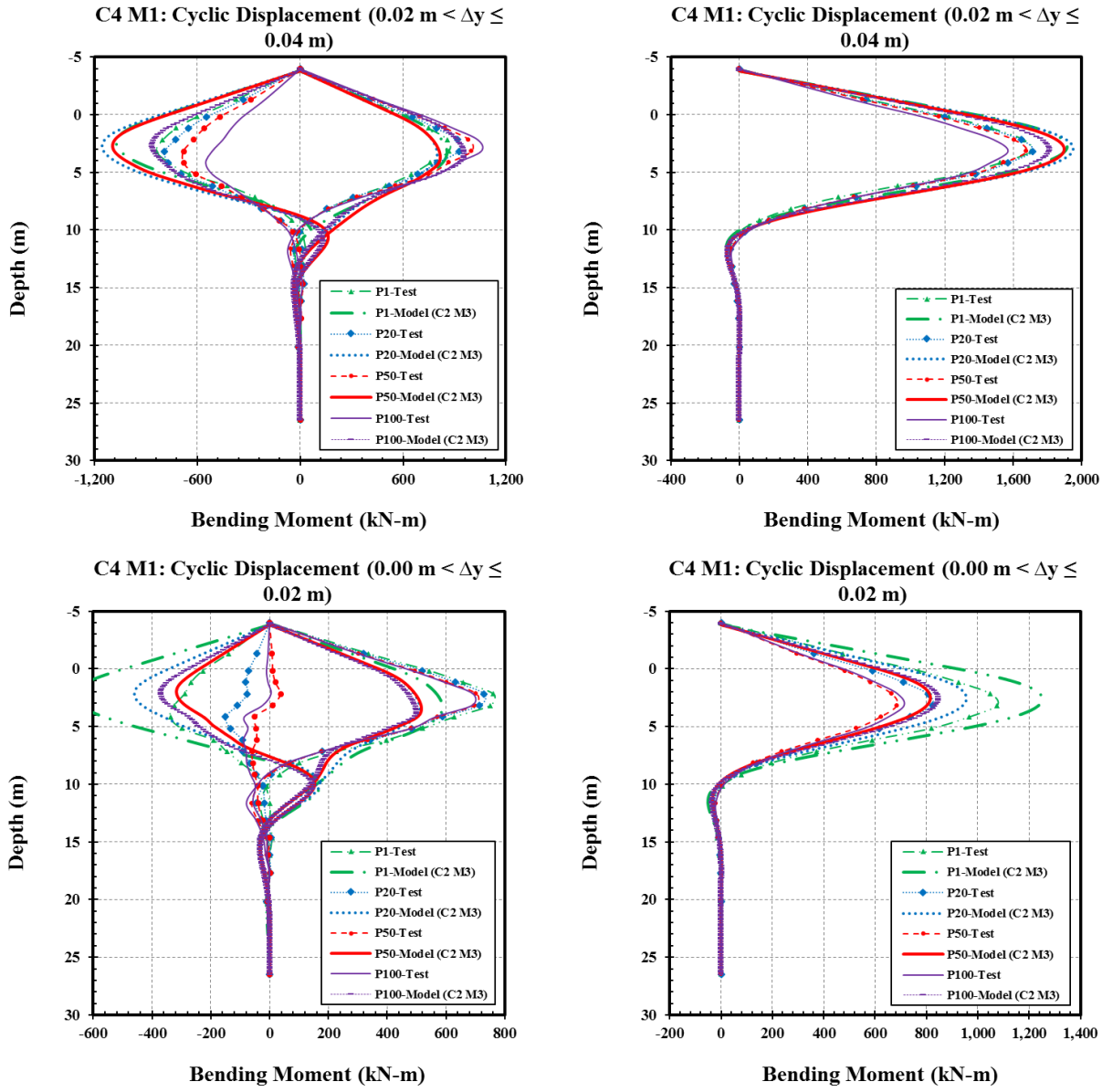


**Figure 7. 7 b: Model bending moment using parameter from C2M3 comparison to C4M1 (random motion) for cyclic displacements lesser than or equal 0.04 m for stiff clay soil.**

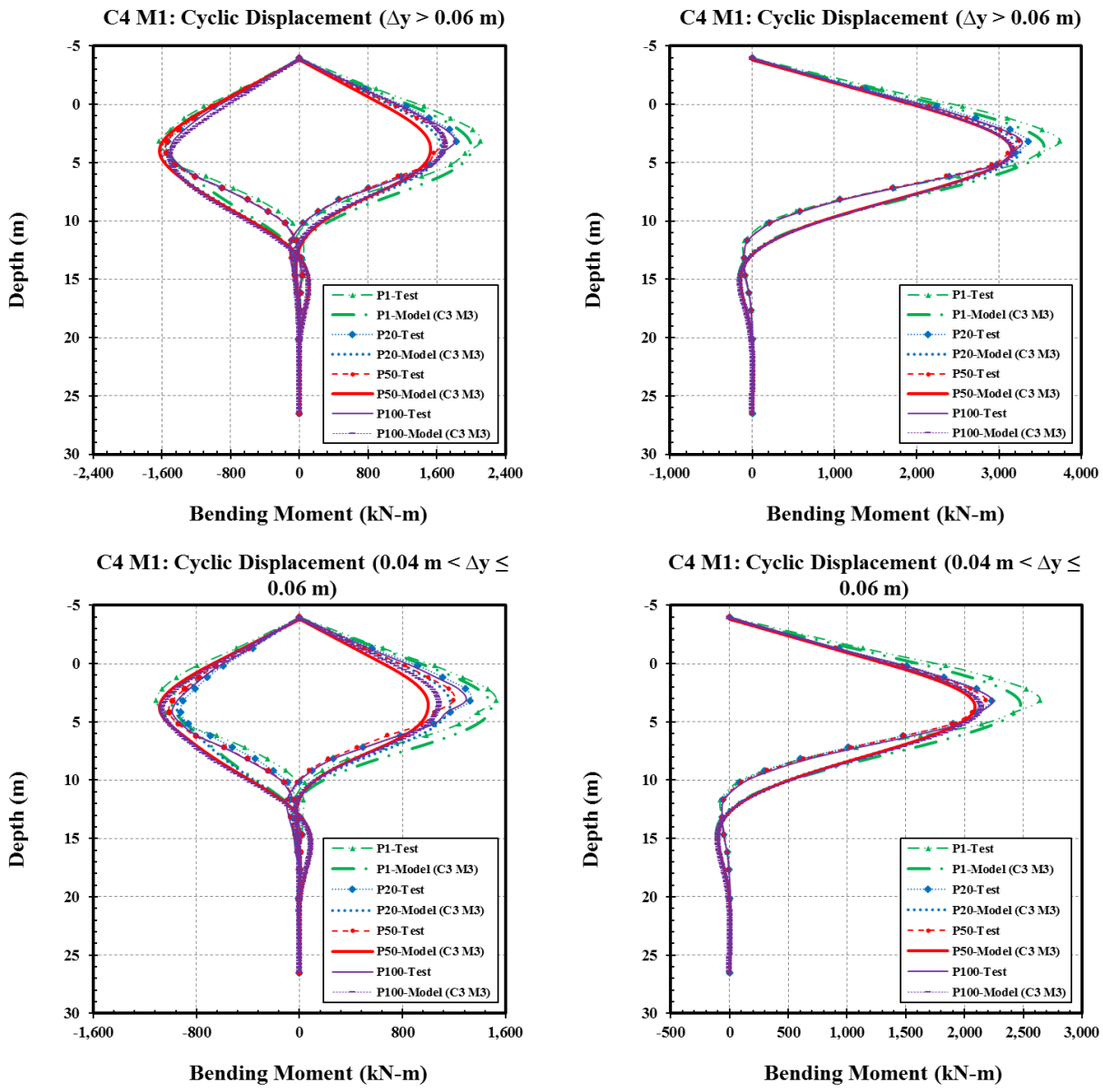


**Figure 7. 7 c: Model bending moment using parameter from C3M3 comparison to C4M1 (random motion) for cyclic displacements greater than 0.04 m for stiff clay soil.**

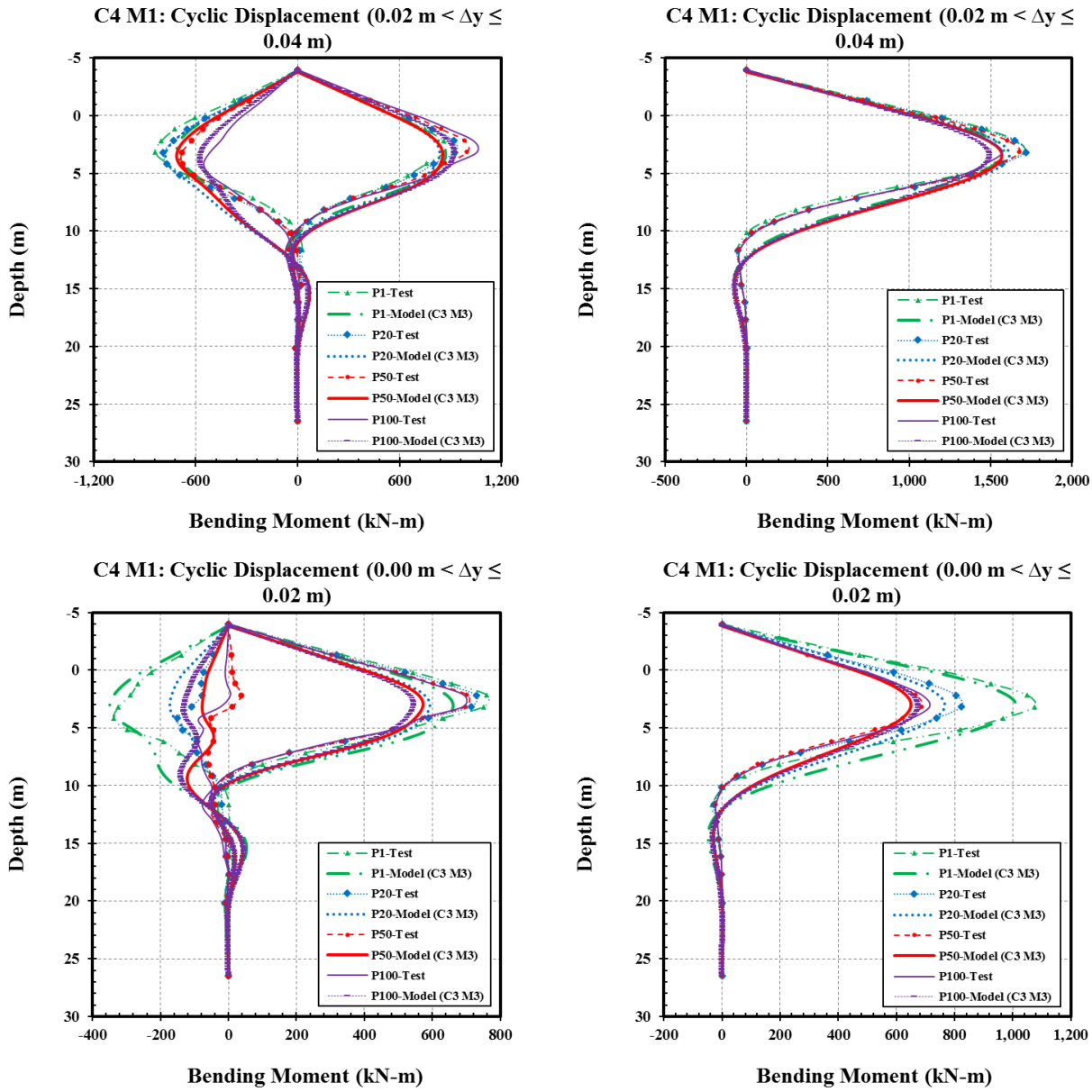


**Figure 7. 7 d: Model bending moment using parameter from C3M3 comparison to C4M1 (random motion) for cyclic displacements lesser than or equal 0.04 m for stiff clay soil.**

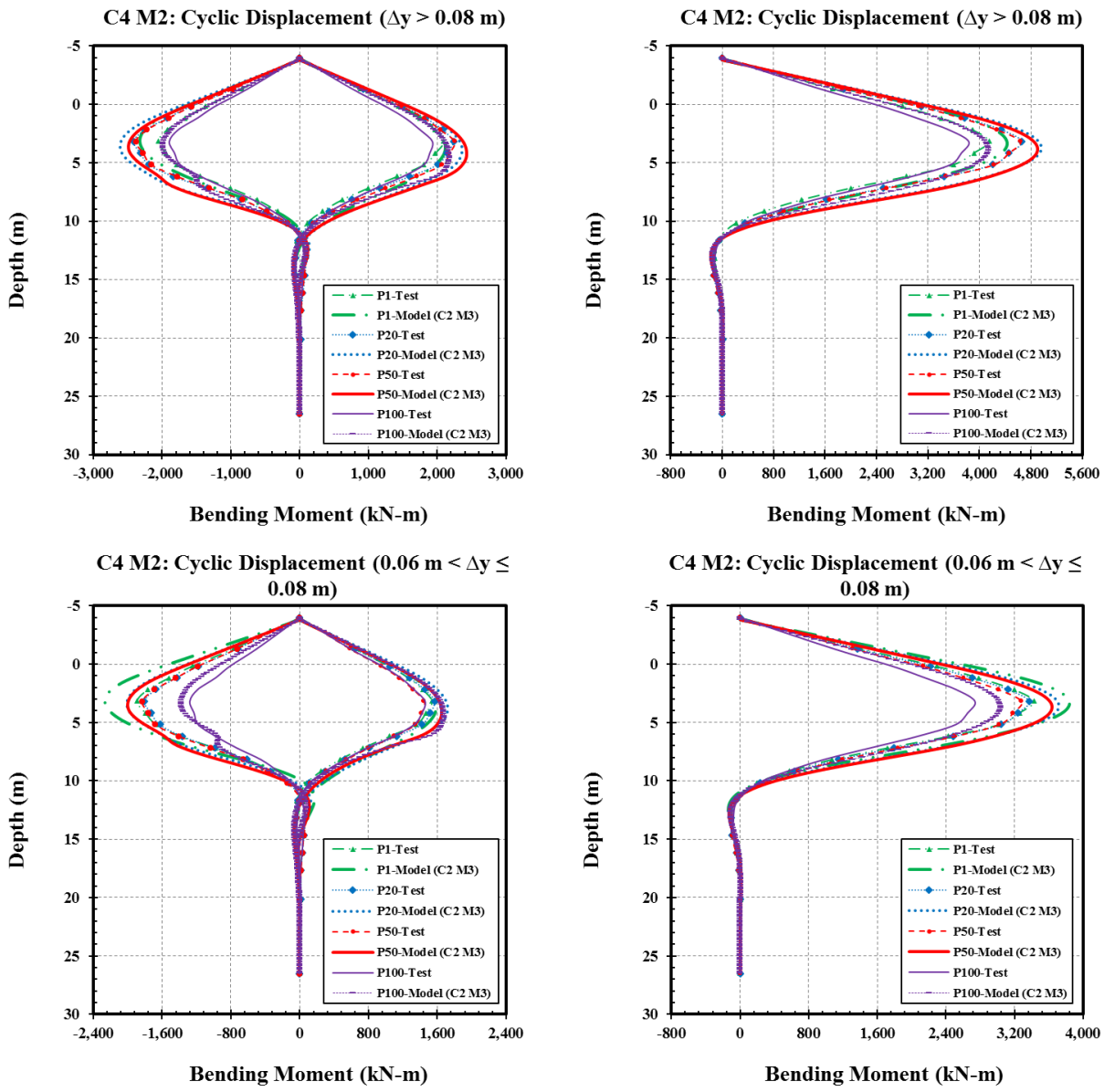


**Figure 7. 8 a: Model bending moment using parameter from C2M3 comparison to C4M2 (random motion) for cyclic displacements greater than 0.06 m for stiff clay soil.**

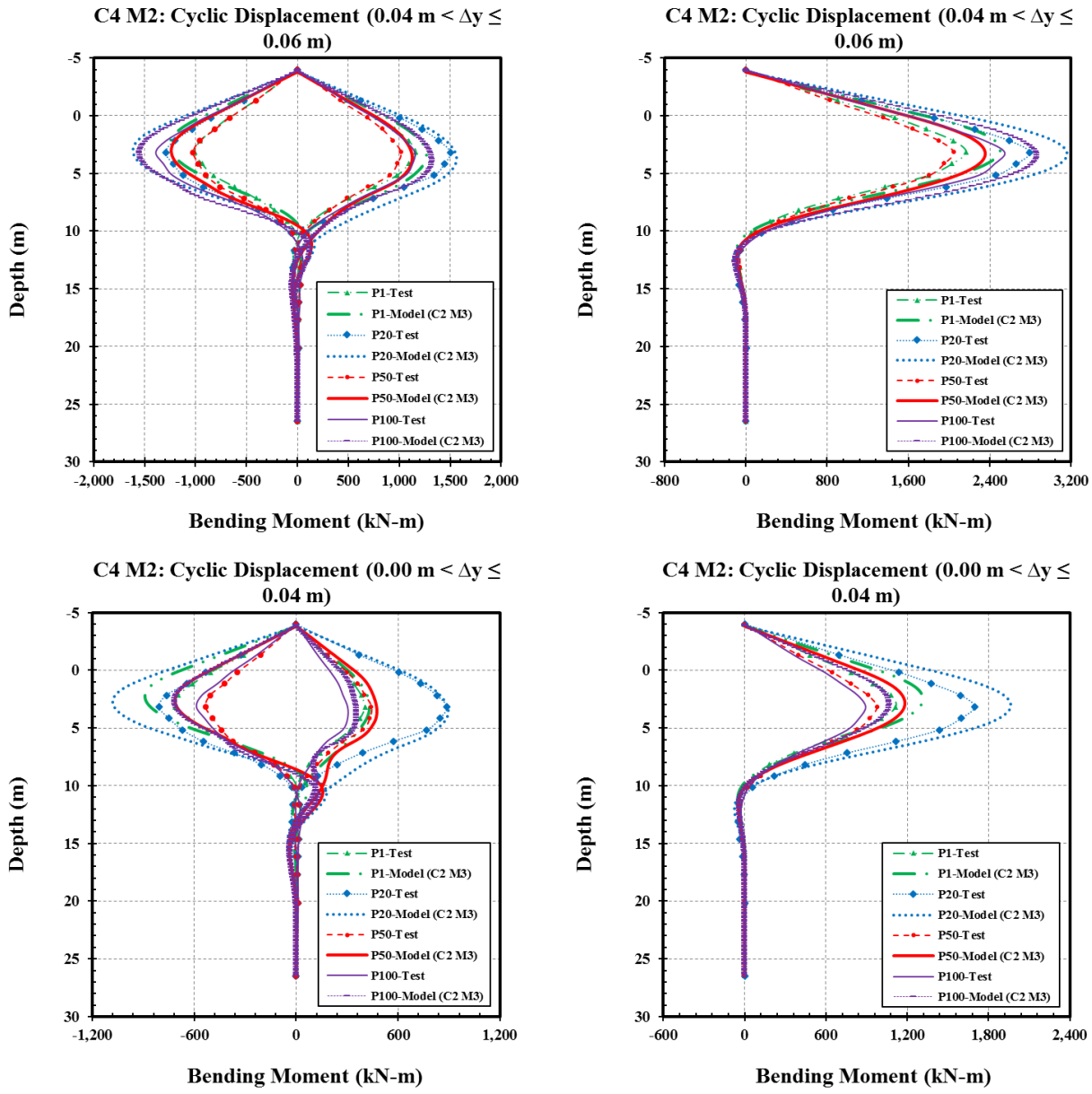


**Figure 7. 8 b: Model bending moment using parameter from C2M3 comparison to C4M2 (random motion) for cyclic displacements lesser than or equal 0.06 m for stiff clay soil.**

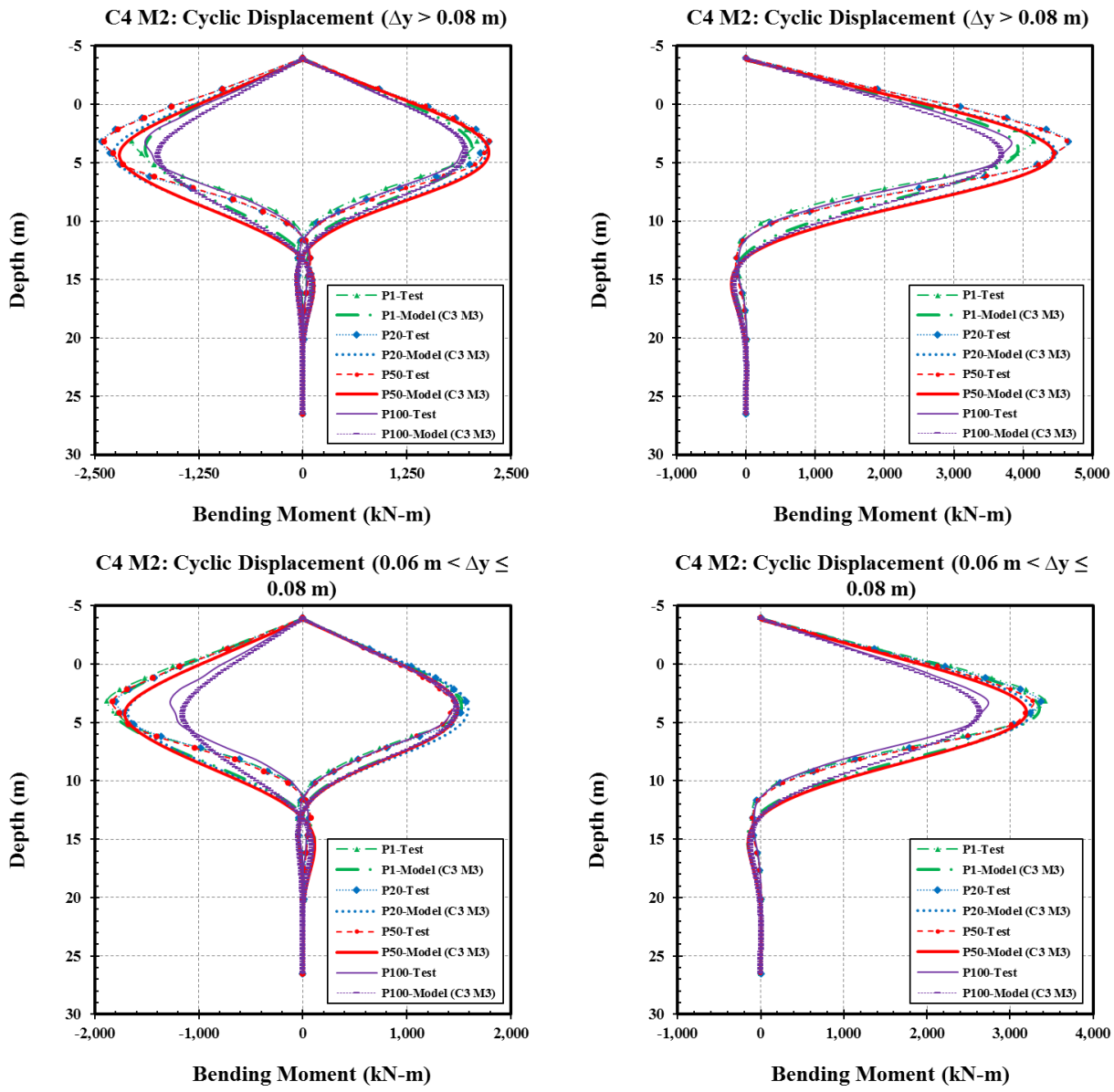


**Figure 7. 8 c: Model bending moment using parameter from C3M3 comparison to C4M2 (random motion) for cyclic displacements greater than 0.06 m for stiff clay soil.**

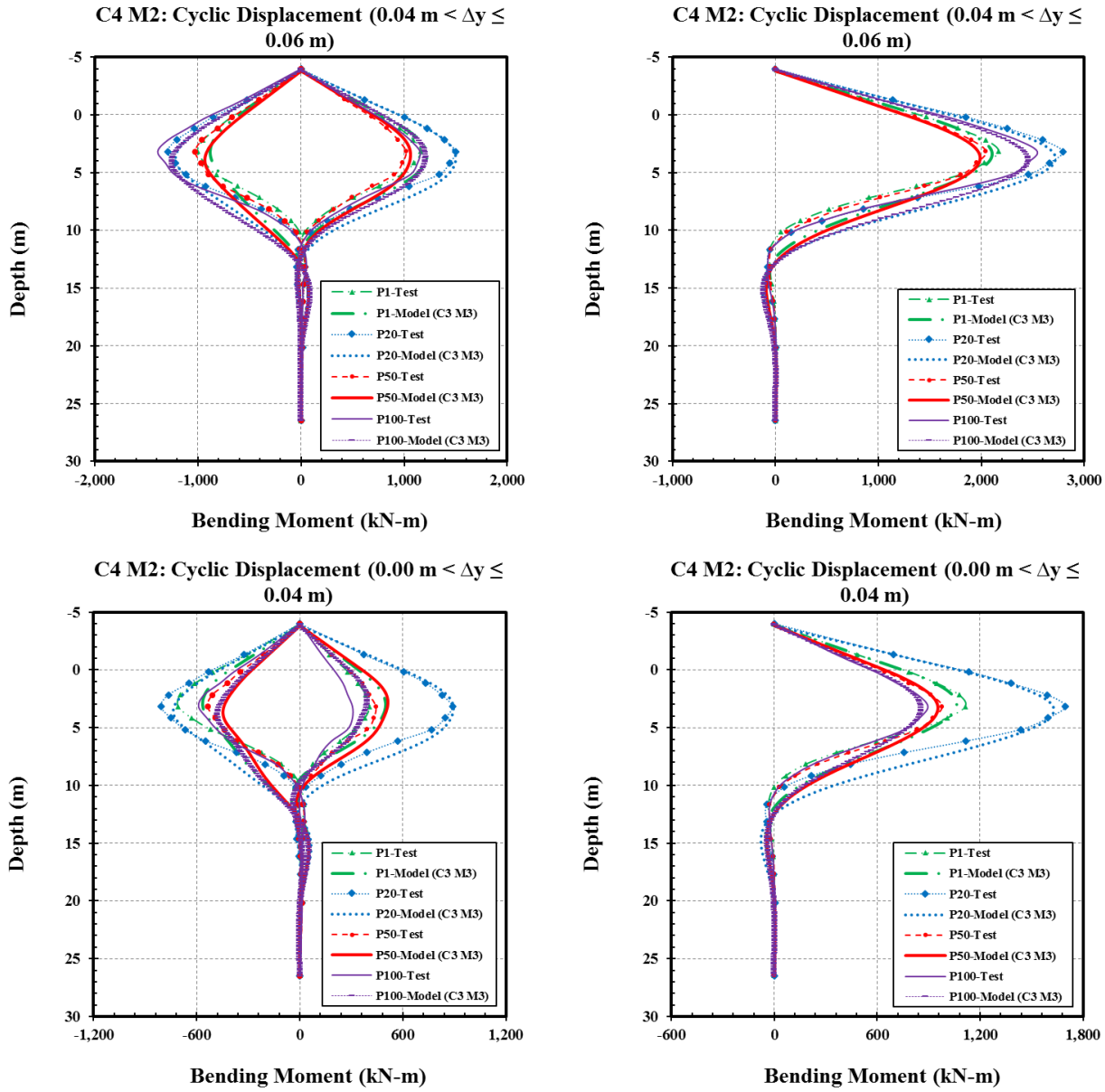


**Figure 7. 8 d: Model bending moment using parameter from C3M3 comparison to C4M2 (random motion) for cyclic displacements lesser than or equal 0.06 m for stiff clay soil.**

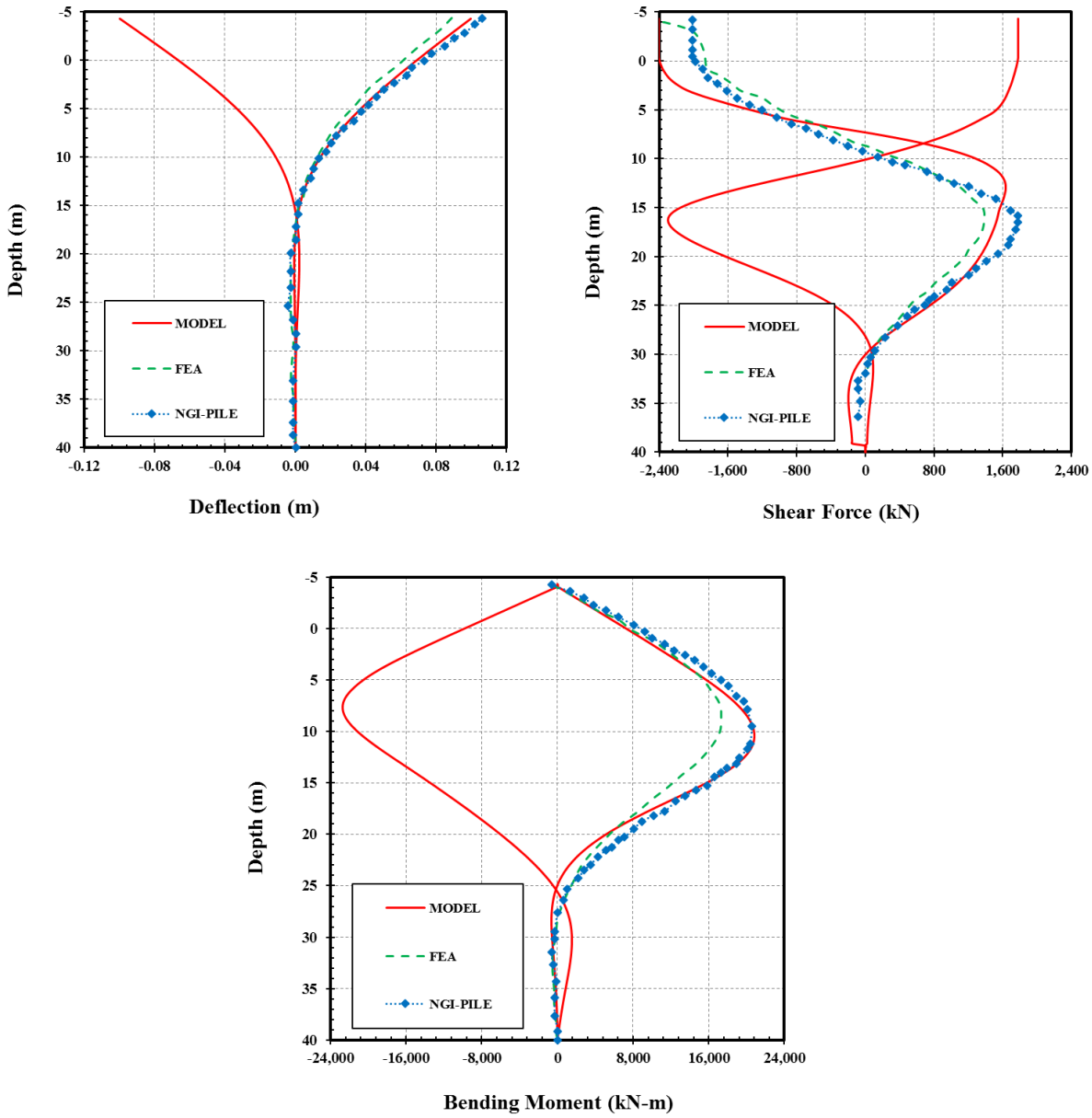


**Figure 7. 9: Comparison of model result to result and data present in Zhang, et al. (2017).**

Fatigue Life

Improving the fatigue life estimates of the of the conductor or pile when the structure is subjected to cyclic load, is an integral part of this research work. The fatigue life of the centrifuge test for the harmonic motions (C2M1, C2M2, C2M3, C3M1, C3M2, and C3M3) and random motions (C4M1 and C4M2) in the soft and stiff clays was compared to the results of the model described in the preceding sections. The results of the fatigue analysis are presented below in Figure 7.10a and 7.10b, and Figure 7.11a and 7.11b.

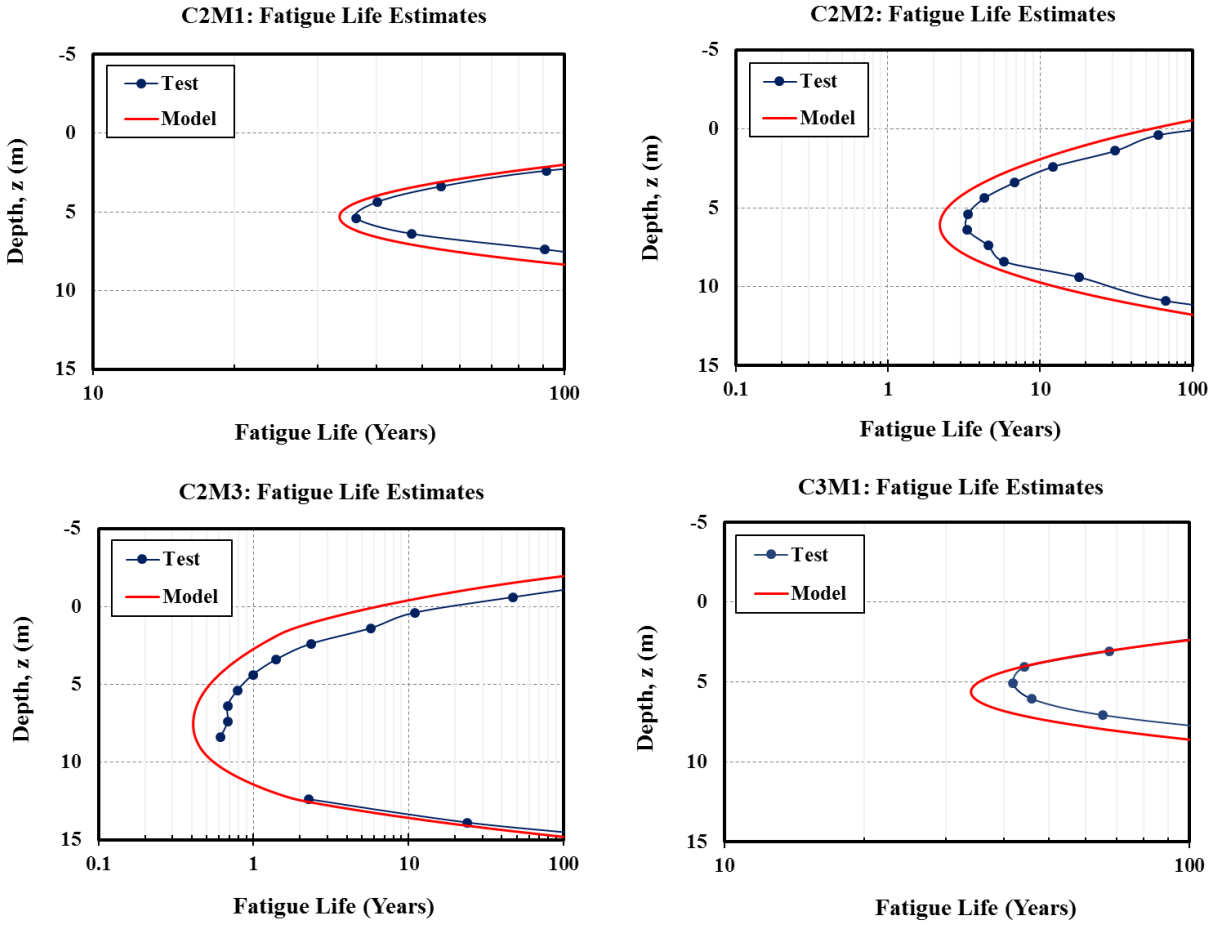


**Figure 7. 10 a: Fatigue life comparison between test and model for symmetric harmonic motions in soft clay soil.**

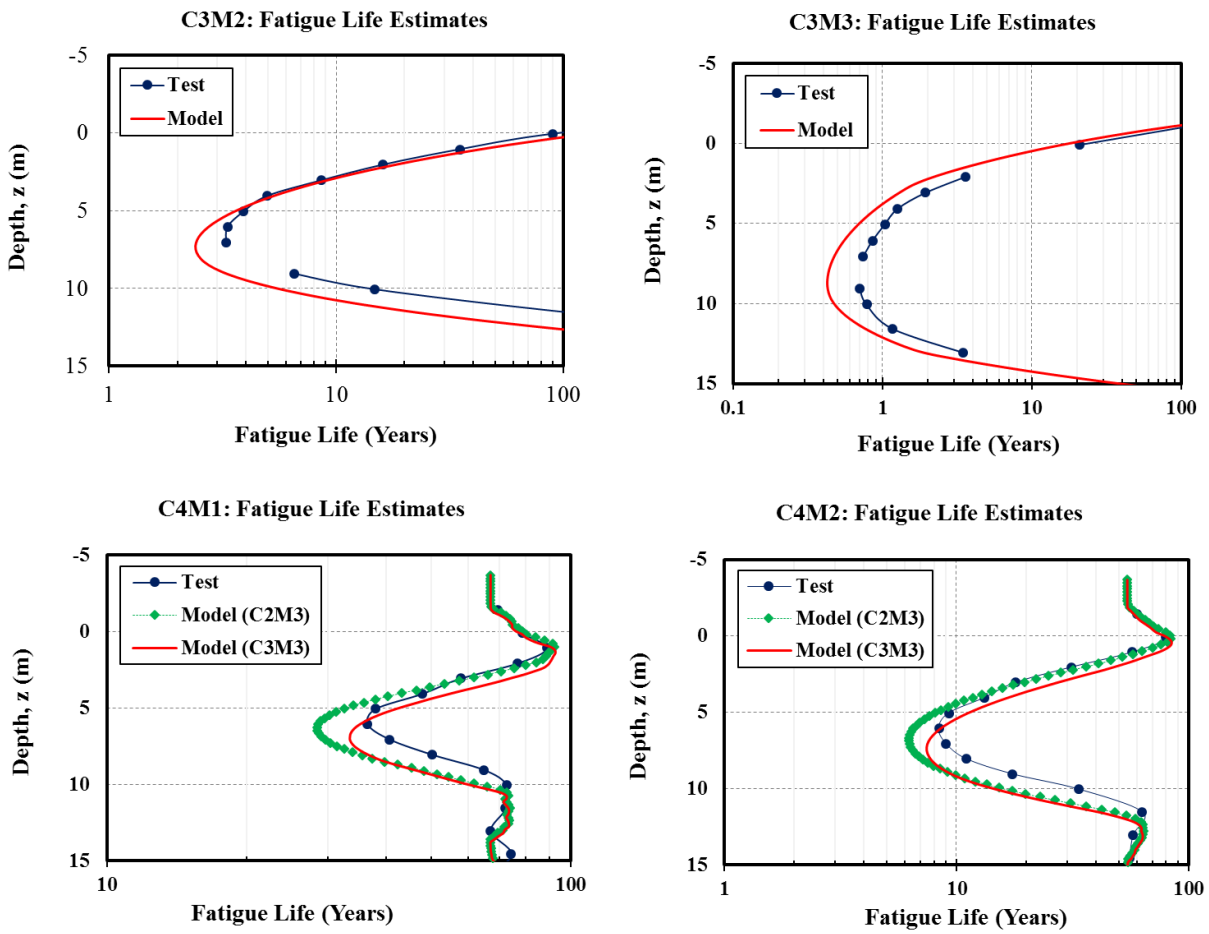


**Figure 7. 10 b: Fatigue life comparison between test and model for non-symmetric harmonic motions in soft clay soil.**

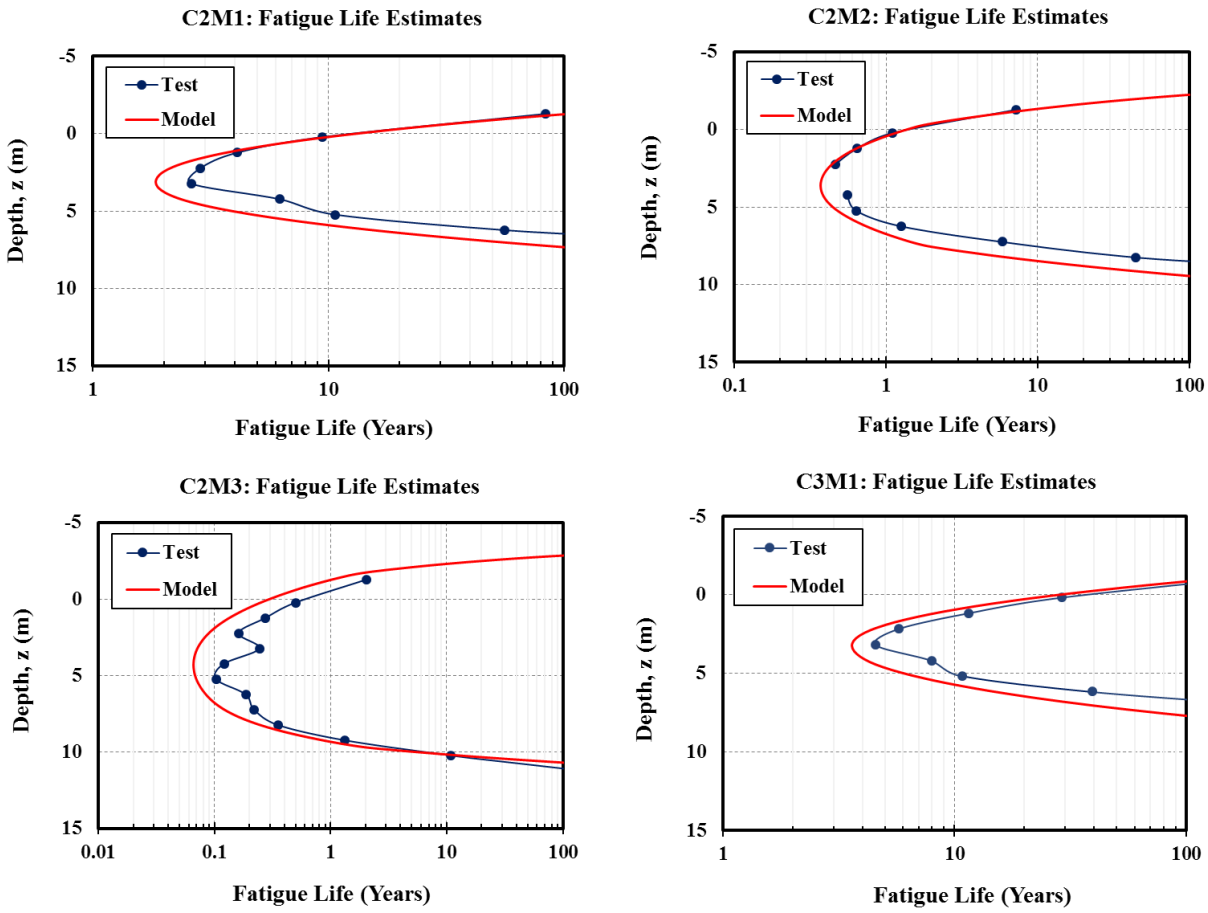


**Figure 7. 11 a: Fatigue life comparison between test and model for symmetric harmonic motions in stiff clay soil.**

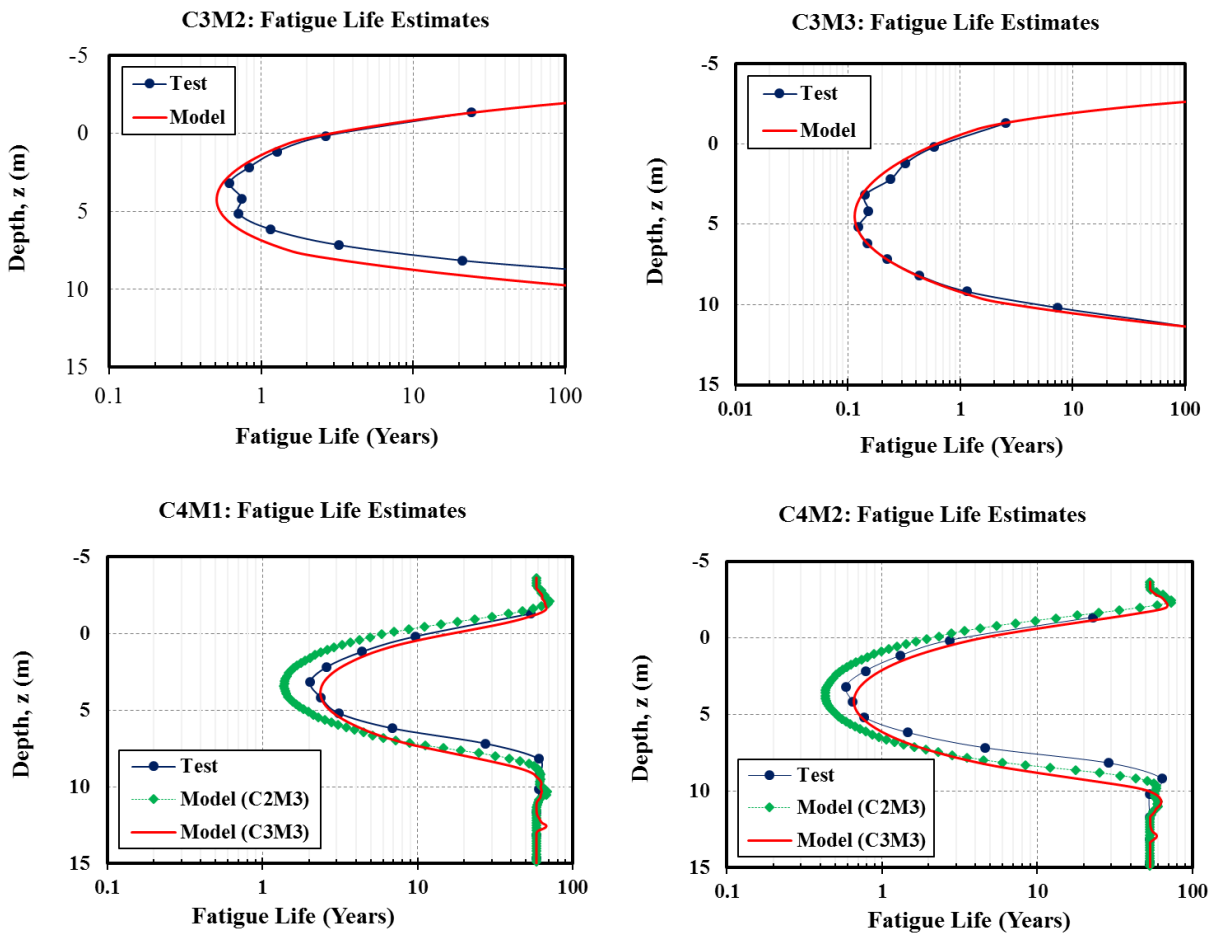


**Figure 7. 11 b: Fatigue life comparison between test and model for non-symmetric harmonic motions in stiff clay soil.**

Bounding Surface Model

The working sequence of this bounding surface model is presented succinctly here, at the onset of loading (initial state), the resistance is zero ($P = P_{\alpha} = P_{in} = 0$), prior to any load application. Once loading commences, the behavior is elastic, until the soil resistance reaches the yield surface ($P = P_{in} = P_y$). At this point plastic behavior sets in, leading have some plastic loads. As plastic loading continues in the same loading path, $P_{in}$ does not change, and the yield surfave elvolves according to the kinematic hardening law preented in Eq. 6.5. Id the pile load is been reversed, with unloading, the initial slope is the elastic modulus and the behavior remains in the elastic region until the forces reaches the lower yield surface, controlled by Eq. 6.3a. The plastic unloading begins, at the start of plastic unloading again, the soil resistance, $P = P_{in} = P_y$ This unloading and reloading sequence continuous it repetitive cycles until the loading on the structure ends. The secant stiffness generated from the P-y curves then become an input for the interaction equation (Eq. 7.1). Below are results for a case load employing the bounding surface model introduced in Chapter VI, linked to the Matlab finite difference model for solving the interaction between the conductor / pile and soil (Appendix C).

The load cases here are presented for a pile, installed in soft clay soil with a harmonic load of 2.5 % D, 5 % D, and 10 %D applied at the pile head, each for 500 load cycles. The pile dimensions are same as the conductors employed in the centrifuge tests (L = 30.5 m, Embedded length = 25.74 m, D = 0.9631 m). The strength profile for the centrifuge soft clay test bed was applied (Figure 4.7a). Figure 7.12 a and Figure 7.12 b presents the result for this load case compared to the centrifuge test results (C2 M1, C2 M2, and C2 M3 – with pile head displacement approximately *0.025D*, *0.05D*, and *0.1D* respectively), for cycle 1, 300 and 499. D represents the pile diameter. The bending moments are presented in Figure 7.12a and Figure 7.12b presents the

error (difference between the model and test maximum cyclic bending moment) trends with half cycles (every half cycle increment). The basic model input parameters are listed below.

Model inputs:

The model inputs include, physical constants; Soil, Pile, and Model properties parameters. These are listed below.

**Physical Constants:**

Acceleration due to gravity, g = 9.81 $m/s^2$

Unit weight of water = 10 $kN/m^3$

Pile Properties:

Pile diameter, D = 0.9631 m

Young's modulus of Pile material, Ep = 208 E6 kPa

**Soil Properties:**

$\varepsilon_{50} = 0.006$ (Strain corresponding to 50 % of the maximum principal stress difference from an undrained compression test).

Yield strain = 0.01 %

Specific gravity of Kaolin, Gs = 2.64

Poisson's ratio = 0.45

Undrained shear strength profile, su (Figure 4.7a)

**Model Parameters:**

The model parameters ($P_{ult}$, $K_e$, $P_{yield}$, C, Dam), discussed in Chapter VI.

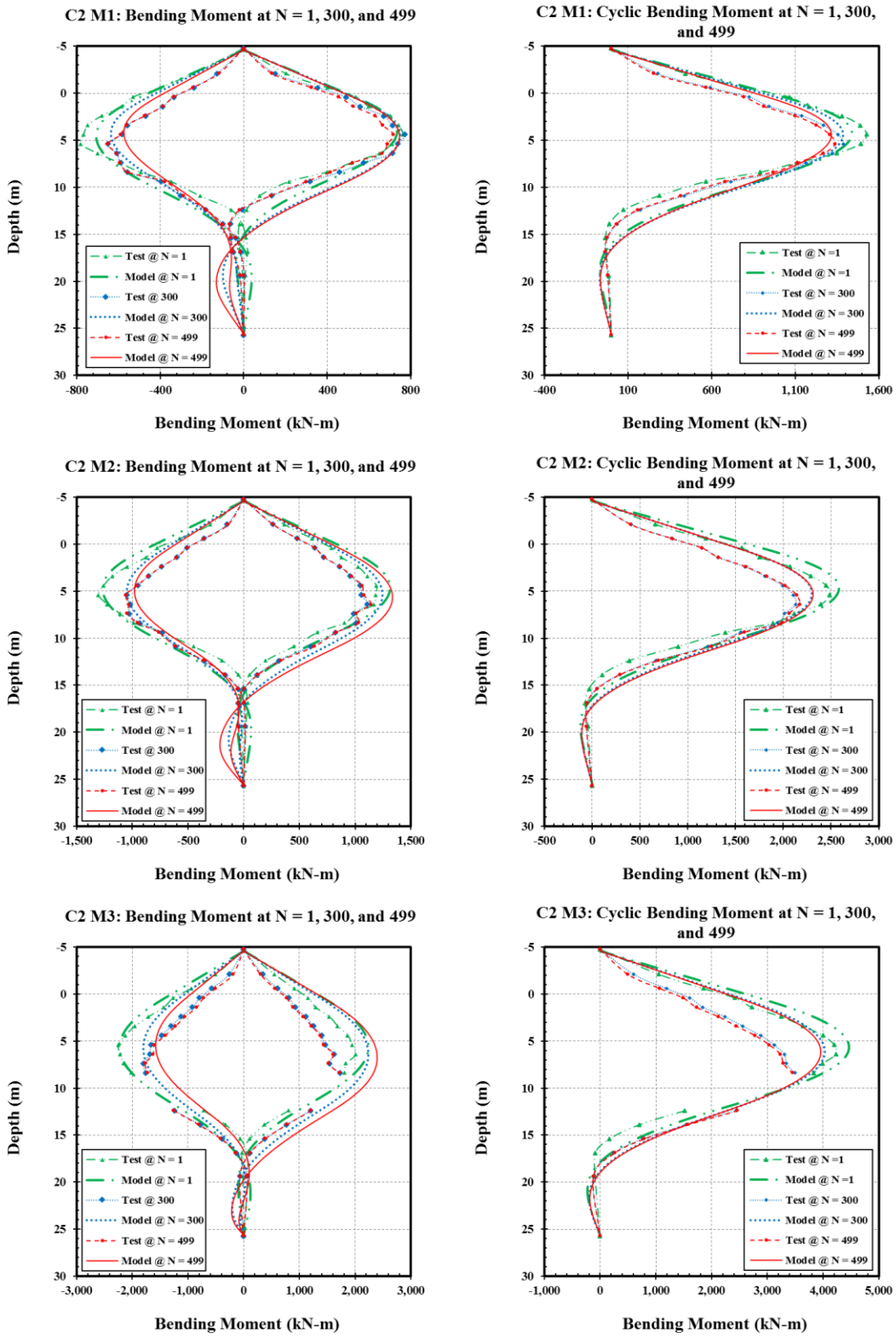


**Figure 7.12 a: Comparison between centrifuge test data and BSP model results.**

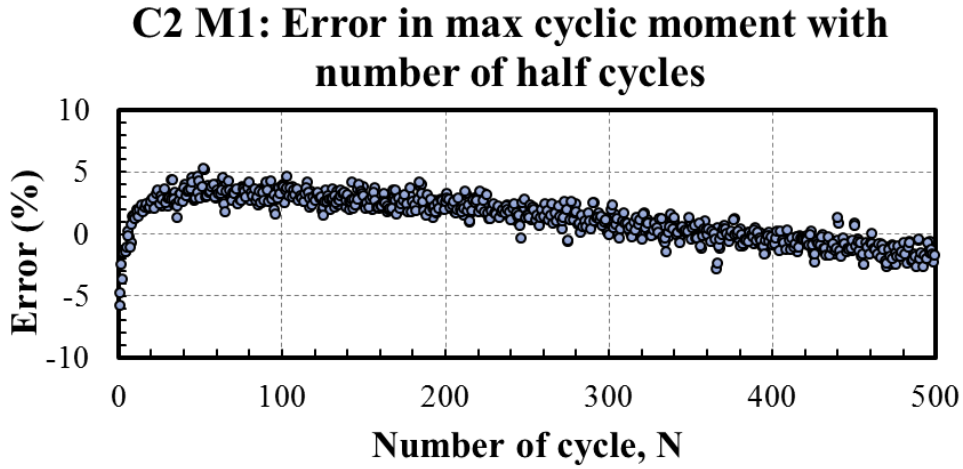


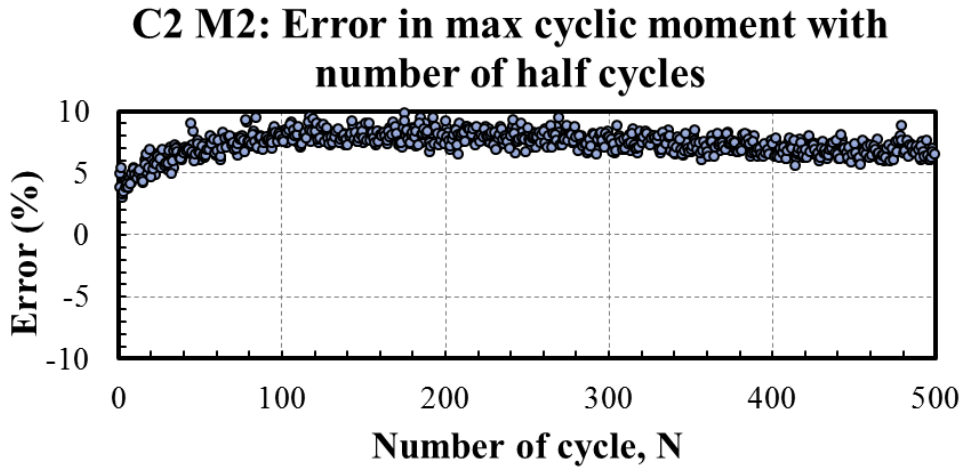


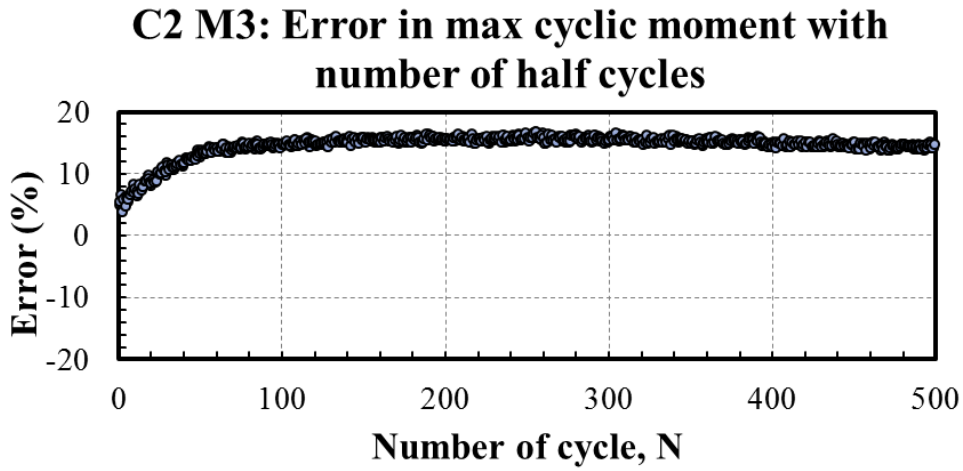


**Figure 7.12 b: Error estimates between the max. cyclic test and model moment for test 2 (C2) M1, M2, and M3 motions.**

# CHAPTER VIII

# SUMMARY AND CONCLUSIONS

Soil-structure interaction is a complex problem arising from nonlinear behavior of clays that degrades under dynamic loading. A comprehensive soil model specific to fatigue assessment of offshore piles and conductors has been described for both soft and stiff clays. Two (2) types of models were considered and described inhere (phenomenological and plasticity model).

## The Phenomenological Model

(1) The initial excursion curve associated with initial small-scale monotonic loading,

(2) Cyclic degradation in stiffness from the initial excursion curve, and

(3) Steady state condition of essentially uniform lateral stiffness under sustained cyclic fatigue loading.

The model was formulated with a view toward maintaining an economy of input parameters, while achieving an acceptable level of accuracy in predicting the cyclic bending moments that develop in the pile. With this view in mind, no attempt was made to simulate certain aspects of behavior, such as the extreme stiffness degradation occurring near the mudline (Figure 5.5) that do not significantly impact bending moments. Within the range of the conductor/pile head displacements (up to 0.15$D$) considered in this study, this model will predict the cyclic $P$-$y$ curves along the pile depths, as well as the deflection profile of the pile and bending moment profiles, using the soil springs presented. This model seeks to capture also the progressive degradation of soil stiffness under the cyclic load application, as the system goes through a transient to a steady

state. An appealing feature of the phenomenological model is its ability to reproduce such complex behavior with relatively few parameters (5 per spring) which can be derived with minimal subjectivity. A summary of the model equations is presented in Table 3.1. While measured soil resistance and the associated model input parameters appear to be dependent on depth, displacement level, and previous load history, the proposed model utilizes only depth-dependent parameters (Table 5.3). Although the displacement level and previous load history appear to have some effect on soil response, simple rules for incorporating these effects into the model do not appear feasible. Thus, the approach adopted herein is to perform multiple analyses for different sets of model parameters corresponding to different displacement levels and load histories. This approach produces a range of predicted bending moments that typically varies by approximately 20%. Noting that fatigue damage is proportional to a high power of stress range, the effect of this variability is not necessarily insignificant, but likely within the acceptable bounds of uncertainty for most fatigue life assessments. Fatigue life assessments were carried out using this model outputs. This model showed great agreement with the test computed fatigue life for harmonic and random motions in soft and stiff clay test bed presented in Figure 7.10a to 7.11b.

Some key aspects of this model include the following:

- Normalized model soil resistance ($P$) by undrained shear strength time pile diameter ($s_u$D), which is more effective than by ultimate lateral resistance $P_{ult}$, since the latter adds another layer of uncertainty in predictions without materially improving the model performance.
- The initial small excursion curve is adequately modeled by the hyperbolic relationship in Eq. 3.1. The parameters $K_{max}$ and $f$ for this equation are depth-dependent, as shown in Table 5.3.

These parameters also show dependency on the test series, which could be a consequence of disturbance in the test footprint due to prior loading.

- Unload-reload loops are adequately modeled by the power law relationship in Eq. 3.2, except in cases of large displacements at shallow depths. The power law parameters $K_0$ and $n$ are depth depth-dependent and are obtained from curve fits for the first unload cycle.
- The selected stiffness degradation law (Eq. 3.6) permits updating of the stiffness after each load reversal, rendering the model well suited to random loading. Stiffness degradation is characterized in terms of a parameter $t$, which increases with increasing magnitude of cyclic displacement $\Delta y_{cyc}$.
- Effects of previous load history are not captured in this model, and the test results do show that this has an effect on the soil stiffness. However, using sets of model parameters derived from experimental data in pristine versus previously disturbed soil profiles permits one to bracket the uncertainty associated with this effect.

The Bounding Surface Model

The elastic, plastic, and tangent elastoplastic stiffness of the soil. The yield surface and bounding surface. This formulation has the attractiveness of being linked to key fundamental soil parameters. These soil parameters can be based on labouratory test results or empirical correlations available in the literature or practice. Utilizing this model requires more computational effort and time to run, compared with the empirical model.

This study has presented great insight into the behavior of this soil-structure interaction challenge and also presented a great model that captures and reproduces vital behavior of the interaction existing between the conductor and the soil when loaded cyclically.

## Recommendations

Preliminary investigation into the above improvements show distinct improvement in the model in regard to the ability to accurately track the evolution of *P-y* curves under cyclic loading. However, further investigation is needed to determine whether added model complexity leads to significant improvement in the predictive capabilities of the model in regard to cyclic bending stresses. Further, it is emphasized that the *P-y* parameters reported in this study are derived from model tests in a low plasticity, low sensitivity clay. Caution should especially be exercised in applying these parameters to high plasticity or sensitive soils, which are likely to experience different levels of stiffness degradation under cyclic loading. Parameters specific to such soils can be used in conjunction with model presented in this paper can be determined either from instrumented pile load tests or, arguably more economically, from the *P-y* element test developed by Zakeri et al. (2017).

Possible future improvements to the model include:

- Expressing the cyclic unload-reload stiffness parameters $K_0$ and $n$ as functions of load cycle in addition to depth.
- Expressing the stiffness degradation parameter $t$ as a function of load cycle in addition to the magnitude of cyclic displacement.

- The improvement of the damage law in the applied uniaxial plasticity model to better capture the observed trends on the cyclic P-y curves under displacement or load control mechanism.

# REFERENCES


4subsea. (n.d.). Retrieved from https://www.4subsea.com/solutions/well-drilling-and-intervention/conductor-analysis/

API. (2011). API Recommended Practice 2GEO/ISO 19901-4, Geotechnical and Foundation Design Considerations. *1st Edition*. American Petroleum Institute (API).

ASTM E1049-85. (2017). Standard Practices for Cycle Counting in Fatigue Analysis. *ASTM International*. doi:10.1520/E1049-85R17

Aubeny, C., & Biscontin, G. (2009). Seafloor-Riser Interaction Model. *International Journal of Geomechanics 9(3)*, 133-141.

BSEE. (n.d.). *Deepwater Development Systems in the Gulf of Mexico Basic Options*. Retrieved January 18, 2018, from https://www.bsee.gov/site-page/deepwater-development-systems-in-the-gulf-of-mexico-basic-options

Choi, J. I., Kim, M. M., & Brandenberg, S. J. (2015). Cyclic p-y Plasticity Model Applied to Pile Foundations in sand. *Journal of Geotechnical and Geoenvironmental Engineering, ASCE*, 141(5):04015013,1-9. doi:10.1061/(ASCE)GT.1943-5606.0001261

Choi, J. I., Kim, M. M., & Brandenberg, S. J. (2016). Erratum for "Cyclic p-y Plasticity Model Applied to Pile Foundations in sand". *Journal of Geotechnical and Geoenvironmental Engineering, ASCE*, 142(6): 08216001. doi:10.1061/(ASCE)GT.1943-5606.0001261

Clukey, E. C., Aubeny, C. P., Zakeri, A., Randolph, M. F., Sharma, P. P., White, D. J., . . . Cerkovnik, M. (2017). A perspective on the state of knowledge regarding soil-pipe interaction of SCR fatigue assessmeents. *Offshore Technology Conference*, (pp. OTC-27564-MS). Houston.

Dafalias, Y. F. (1986). Bounding Surface Plasticityy. I: Mathematical Foundation and Hypoplasticity. *Journal of Engineering Mechanics, ASCE,* 966-987.

DNVGL-RP-C203. (2016). Fatigue design of offshore steel structures. Retrieved from https://rules.dnvgl.com/docs/pdf/DNVGL/RP/2016-04/DNVGL-RP-C203.pdf

Doman, L. (2017, September 17). *US Energy Information Administration (EIA)*. Retrieved April 16, 2019, from https://www.eia.gov/todayinenergy/detail.php?id=32912

Doyle, E. H., Dean, E. R., Sharma, J. S., Bolton, M. D., Valsangkar, A. J., & Newlin, J. A. (2004). *Centrifuge Model Tests on Anchor Piles for Tension Leg Platforms.* Offshore Technology Conference, OTC-16845-MS. doi:10.4043/16845-MS

El-Reedy, M. A. (2012). Offshore Structures: Design, Construction and Maintenance. 1. Elsevier Inc.

EWEA. (2013). *Deep Water The next step for offshore wind energy*. Retrieved January 18, 2018, from http://www.ewea.org/fileadmin/files/library/publications/reports/Deep_Water.pdf

Hodder, M., White, D., & Cassidy, M. (2009). Effect of Remolding and Reconstitution on the Touchdown Stiffness of a Steel Catenary Riser: Observation from Centrifuge Modeling. *Proceeding, Offshore Technology Conference,* (pp. OTC-19871). Houston.

Idriss, I. M., Dobry, R., Doyle, E. H., & Singh, R. D. (1976). Behavior of soft clays under earthquake loading conditions. *8th Offshore Technology Conference, OTC 2671,* (pp. 605-617). Houston.

Idriss, I. M., Dobry, R., Doyle, E. H., & Singh, R. D. (1978). Nonlinear Behavior of soft clays during cyclic loading. *Geotechnical engineering division, Proceedings of the American Society of Civil Engineers, Vol. 104, No. GT12,* 1429-1445.

Jaiswal, V., & Healy, B. (2016, November 01). *DNV GL Technology Week Latest Developments in Fatigue Analysis of Wellhead Systems.* Retrieved from https://www.dnvgl.us/Downloads/TW16-Latest-Developments_tcm14-80212.pdf

Jeanjean, P. (2009). Reassessment of P-y curves for soft clays from centrifuge testing and finite element modeling. *Offshore Technology Conference, OTC 20158.* Houston.

Jeanjean, P., Zhang, Y., Zakeri, A., & Andersen, K. (2017). A Framework for Monotnic P-Y Curves in Clays (Keynote Lecture). *Offshore Site Investigation & Geotechnics Committee 8th International Conference "Smarter Solutions for Future Offshore Developments".* London.

King, G. W. (1990, September 01). Drilling Engineering for Subsea Development Wells. *SPE Journal of Petroleoum Technology, 42*(09), 1176-1183. doi:https:/doi.org/10.2118/18687-PA

Krieg, R. D. (1975). A Pratical Two Surface Plasticity Theory. *Journal of Applied Mechanics, ASME*, 641-646.

Lorents, R. (2012). *Wellhead Fatigue Analysis Surface casing cement boundary condition for subsea wellhead fatigue analytical models.* Retrieved from https://core.ac.uk/download/pdf/30843853.pdf

Matlock, H. (1970, January 01). Correlation for Design of Laterally Loaded Piles in Soft Clay. Offshore Technology Conference, OTC-120-MS. doi:10.40431204-MS

Matlock, H., & Reese, L. C. (1962). Generalized solutions for laterally loaded piles. *Transactions of the American Society of Civil Engineers, 127(1),* 1220-1247.

McCarron, W. O. (2015). Bounding surface model for soil resistance to cyclic lateral pile displacements with arbitrary direction. *Elsevier*, 47-55.

McClelland, B., & Focht, J. A. (1958). Soil modulus for laterally loaded piles. *Transactions of the American Society of Civil Engineers, 123(1),* 1049-1063.

Milberger, L. J., Yu, A., Hosie, S., & Hines, F. (1991). Structural requirements for the effective transfer of environmental loadings in a subsea wellhead system. *Offshore Technology Conference.* Houston.

Movik, H. (2006). Fatigue damages at wellhead. *Underwater Technology Conference.* Bergen: Norway.

Murff, J. D., & Hamilton, J. M. (1993). P-Ultimate for Undrained Analysis of Laterally Loaded Piles. *Journal of Geotechnical Engineering. 119. 10.1061/(ASCE)0733-9410(1993)119:1(91).*

Newcomb, T. (2017). *7 of the World's Biggest and Baddest offshore structures.* Retrieved January 18, 2018, from http://www.popularmechanics.com/technology/infrastructure/g2926/7-of-the-biggest-offshore-structures/

O'Neil, M. W., & Murchison, J. M. (1983). *An Evaluation of p-y Relationships in Sands.* Houston: American Petroleum Institute, API.

Ovesen, M. (2012). Seminar - subsea wellhead fatigue. *Petroleum Safety Authority (PSA).* Norway.

Reese, L. C., Cox, W. R., & Koop, F. D. (1975, January 01). Field Testing and Analysis of Laterally Loaded Piles in Stiff Clay. Houston, Texas: Offshore Technology Conference, OTC-2312-MS. doi:10.4043/2312-MS

Schofield, A. N. (1980). Cambridge Geotechnical Centrifuge Operations. *Geotechnique 20*, 227-268. doi:https://doi.org/10.1680/geot.1980.30.3.227

Stevens, J. B., & Audibert, J. M. (1979). Re-Examination of P-y Curve Formations. *Offshore Technology Conference, OTC 3402.* Houston.

World Union of Concerned Scientists Science for a Healthy Planet and Safer. (2018). *A Short History of Energy, The Old Days*. Retrieved January 18, 2018, from https://www.ucsusa.org/clean_energy/our-energy-choices/a-short-history-of-energy.html

Yuan, F., White, D. W., & O'Loughlin, S. D. (2016). The Evolution of Seabed Stiffness During Cyclic Movement in a RIser Touchdown Zone on Soft Clay. *Geotechnique*, P. 161.

Zakeri, A. E., Clukey, E., Kebadze, B., Jeanjean, P., Piercey, G., Templeton, J., . . . Aubeny, C. (2015). Recent Advances in Soil Response Modeling for Well Conductor Fatigue Analysis and Development of New Approaches. Houston: Offshore Technology Conference, OTC.

Zakeri, A., Clukey, E. C., Kebadze, B. E., & Jeanjean, P. (2016a). Fatigue analysis of offshore well conductors: Part I – Study overview and evaluation of Series 1 centrifuge tests in normally consolidated to lightly over-consolidated kaolin clay. *Applied Ocean Research 57*, 78-95.

Zakeri, A., Clukey, E. C., Kebadze, B. E., & Jeanjean, P. (2016b). Fatigue Analysis of Offshore Well Conductors: Part II - Development New Approaches for Conductor Fatigue Analysis in Clays and Sands. *Applied Ocean Research 57*, 96-113.

Zhang, Y., Andersen, K., Jeanjean, P., Mirdamadi, A., S Gundersen, A., & Jostad, H. (2017). A framework for cyclic p-y curves in clay and application to pile design in GoM. *Offshore Site Investigation and Geotechnics (OSIG), Society of Underwater Technology (SUT) conference.* London.

APPENDIX A

HYPERBOLIC CURVE FIT TO INITIAL PILE EXCURSION

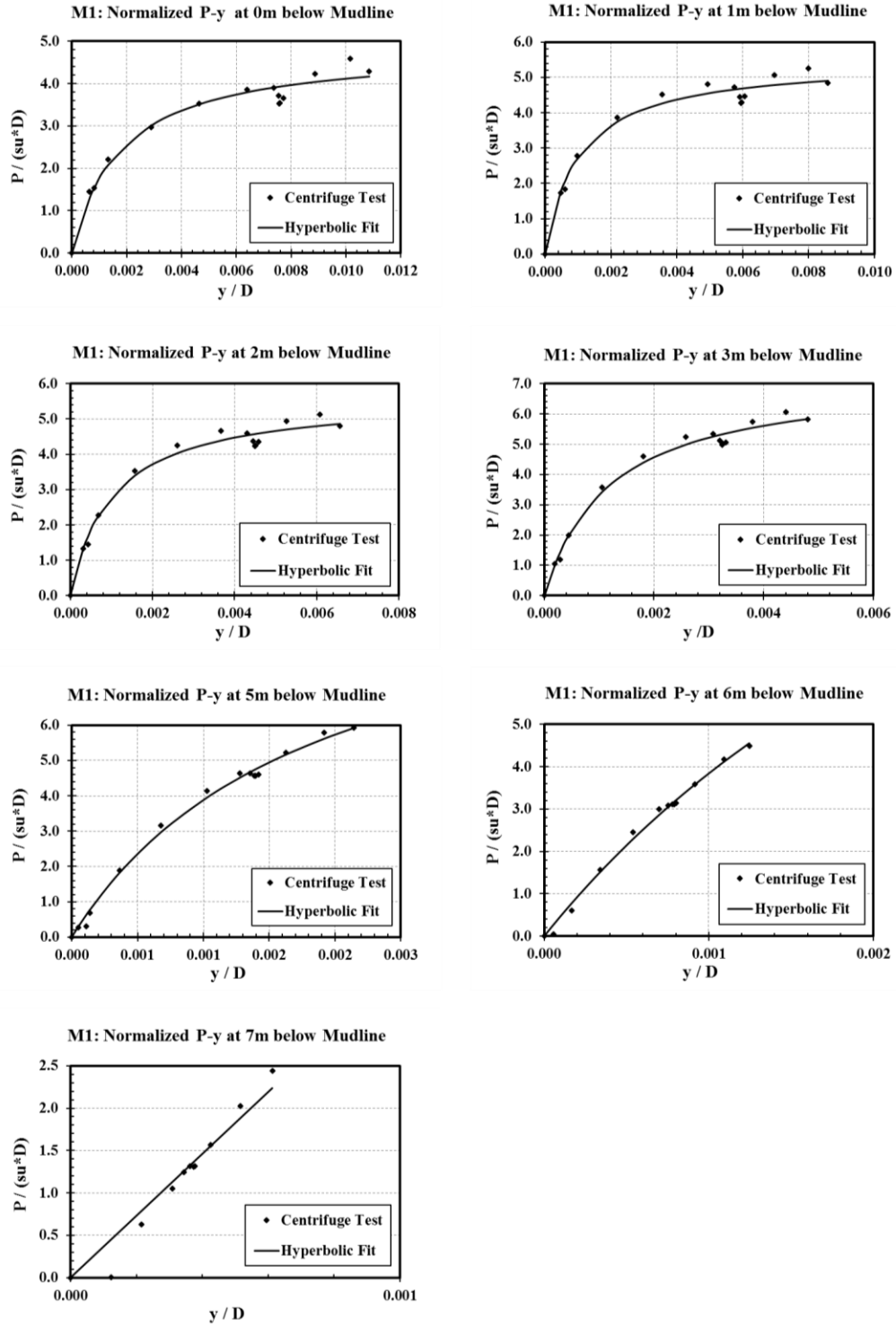


**Figure A.1: Soft Clay Initial Excursion curve fit for Test 2 (C2) M1 Motion.**

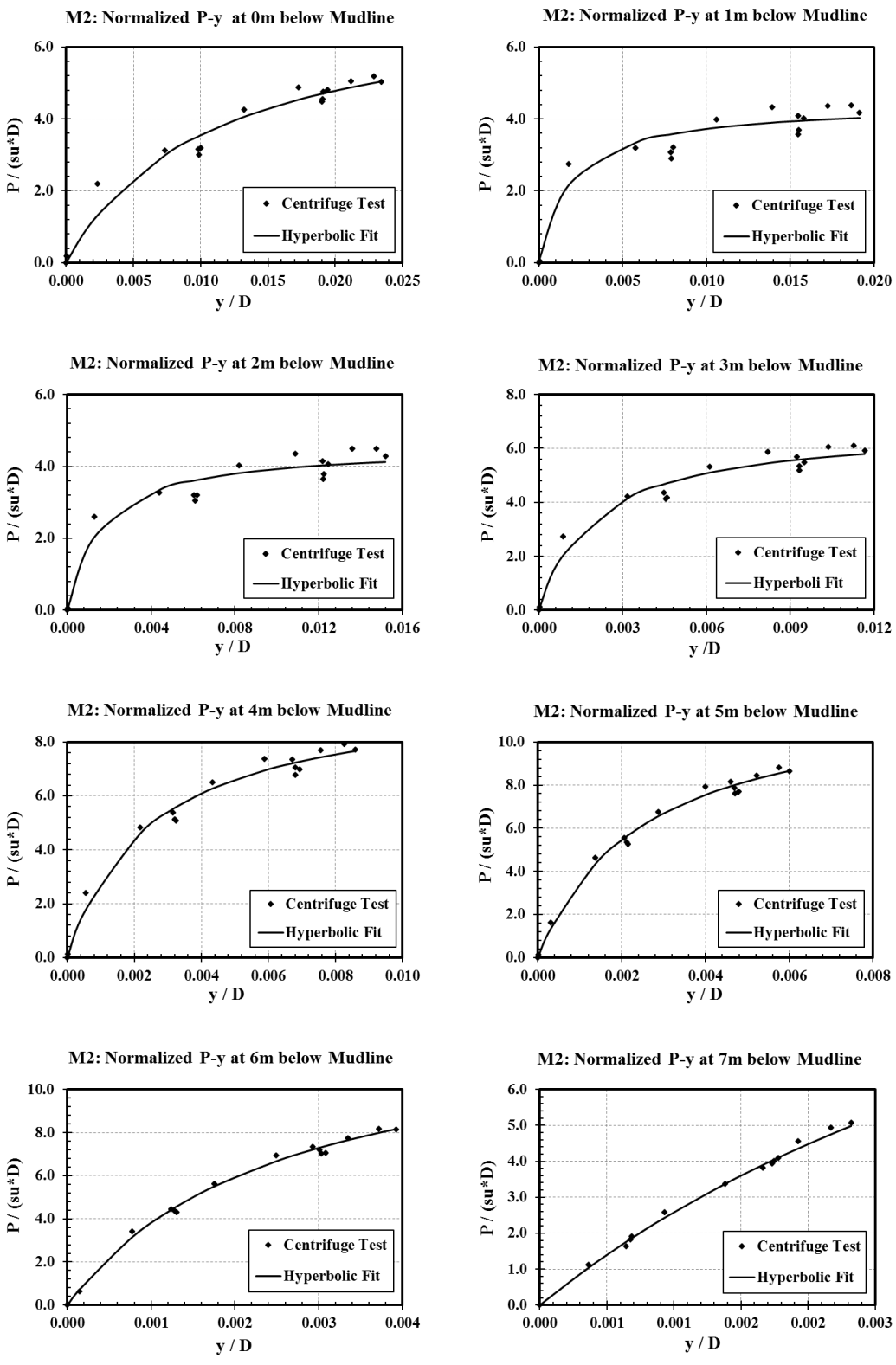


**Figure A.2: Soft Clay Initial Excursion curve fit for Test 2 (C2) M2 Motion.**

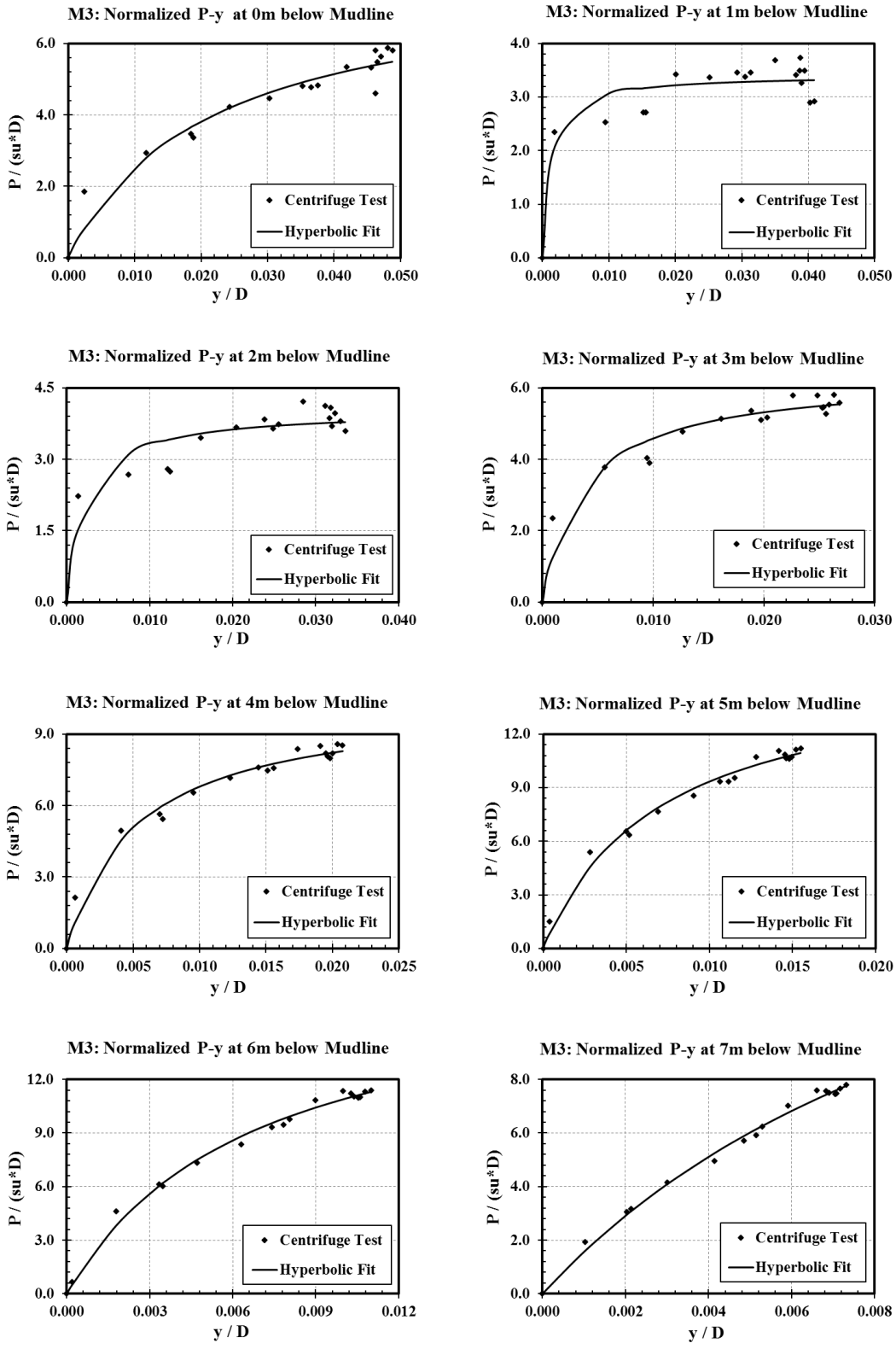


**Figure A.3: Soft Clay Initial Excursion curve fit for Test 2 (C2) M3 Motion.**

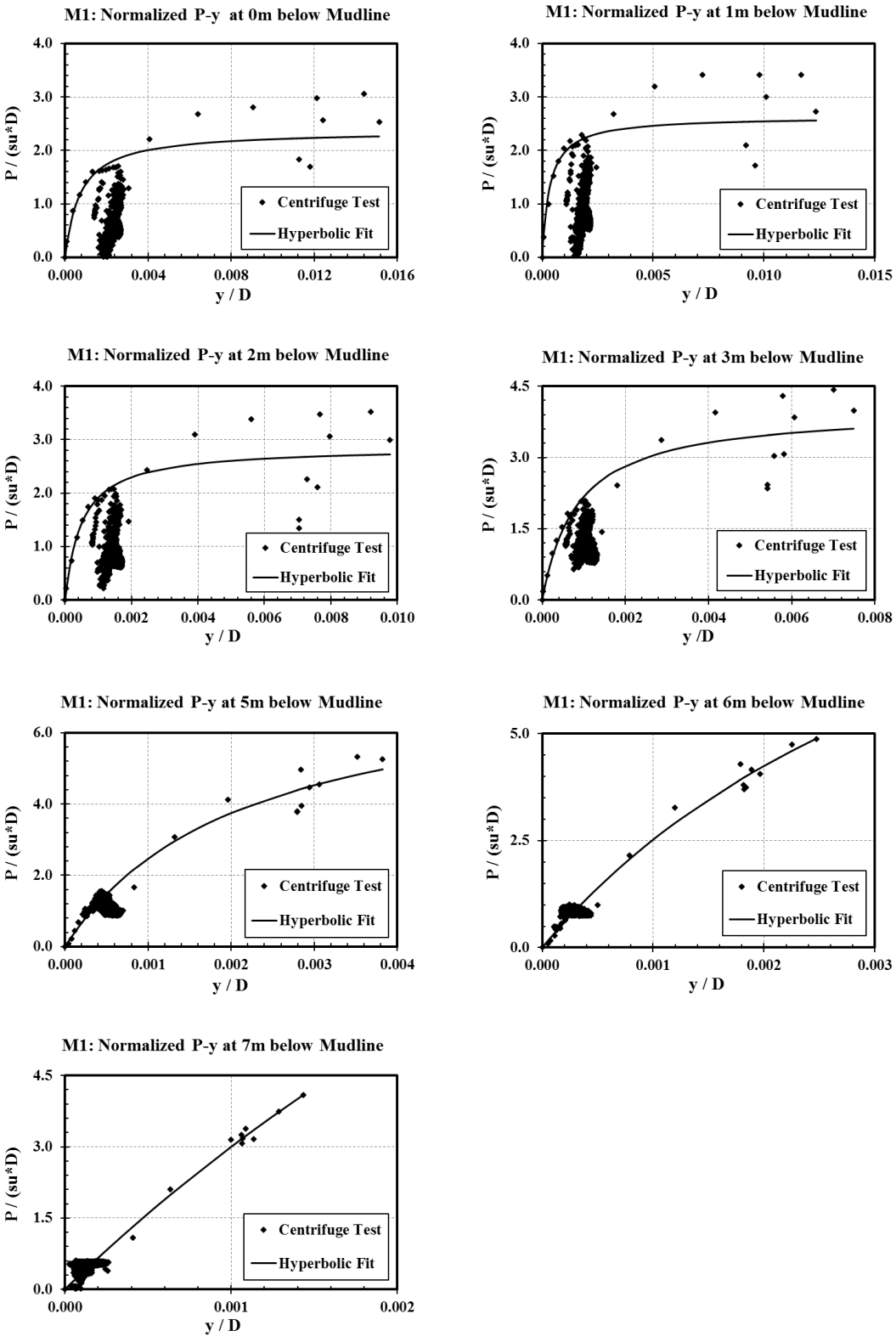


**Figure A.4: Soft Clay Initial Excursion curve fit for Test 3 (C3) M1 Motion.**

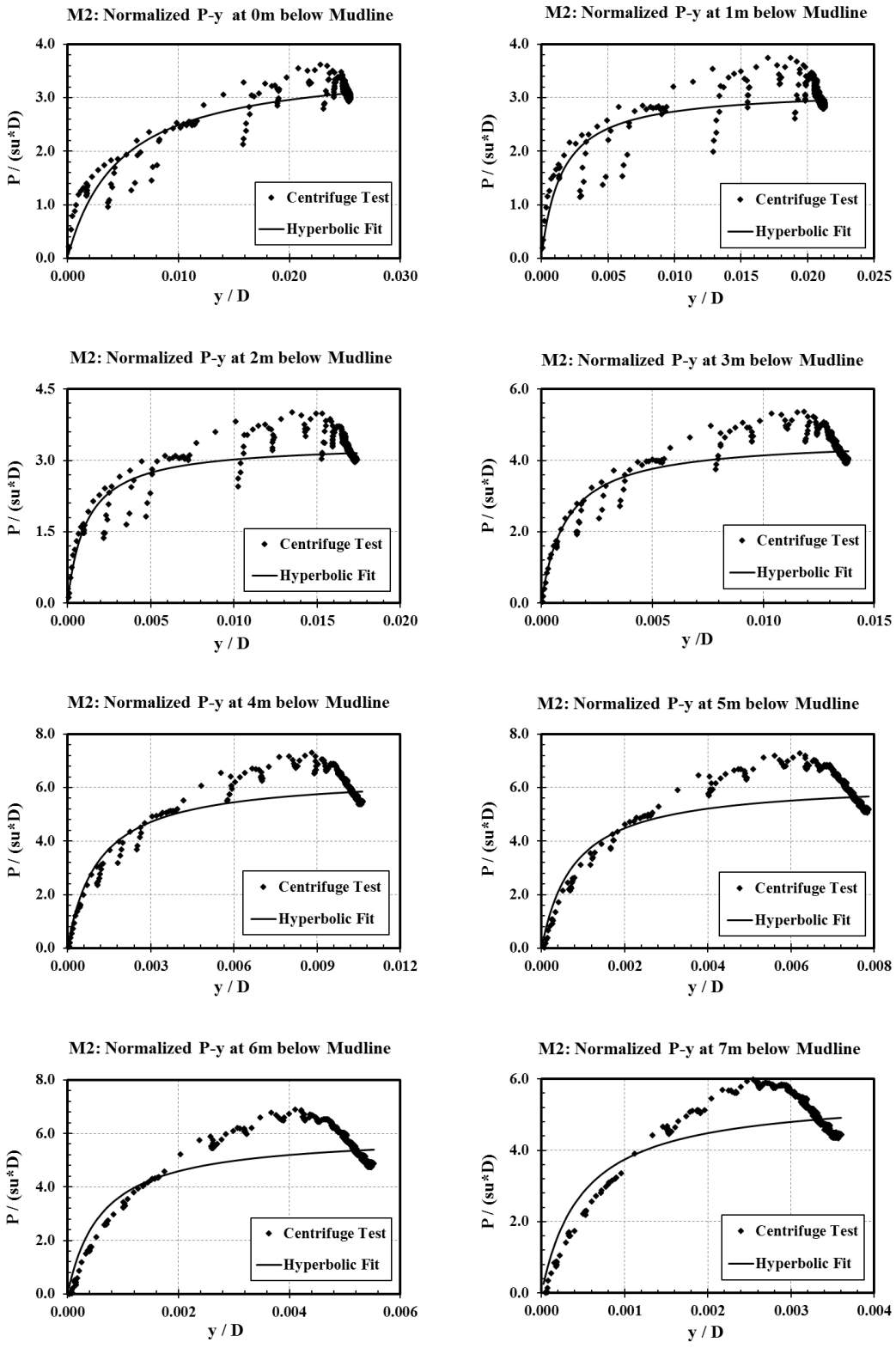


**Figure A.5: Soft Clay Initial Excursion curve fit for Test 3 (C3) M2 Motion.**

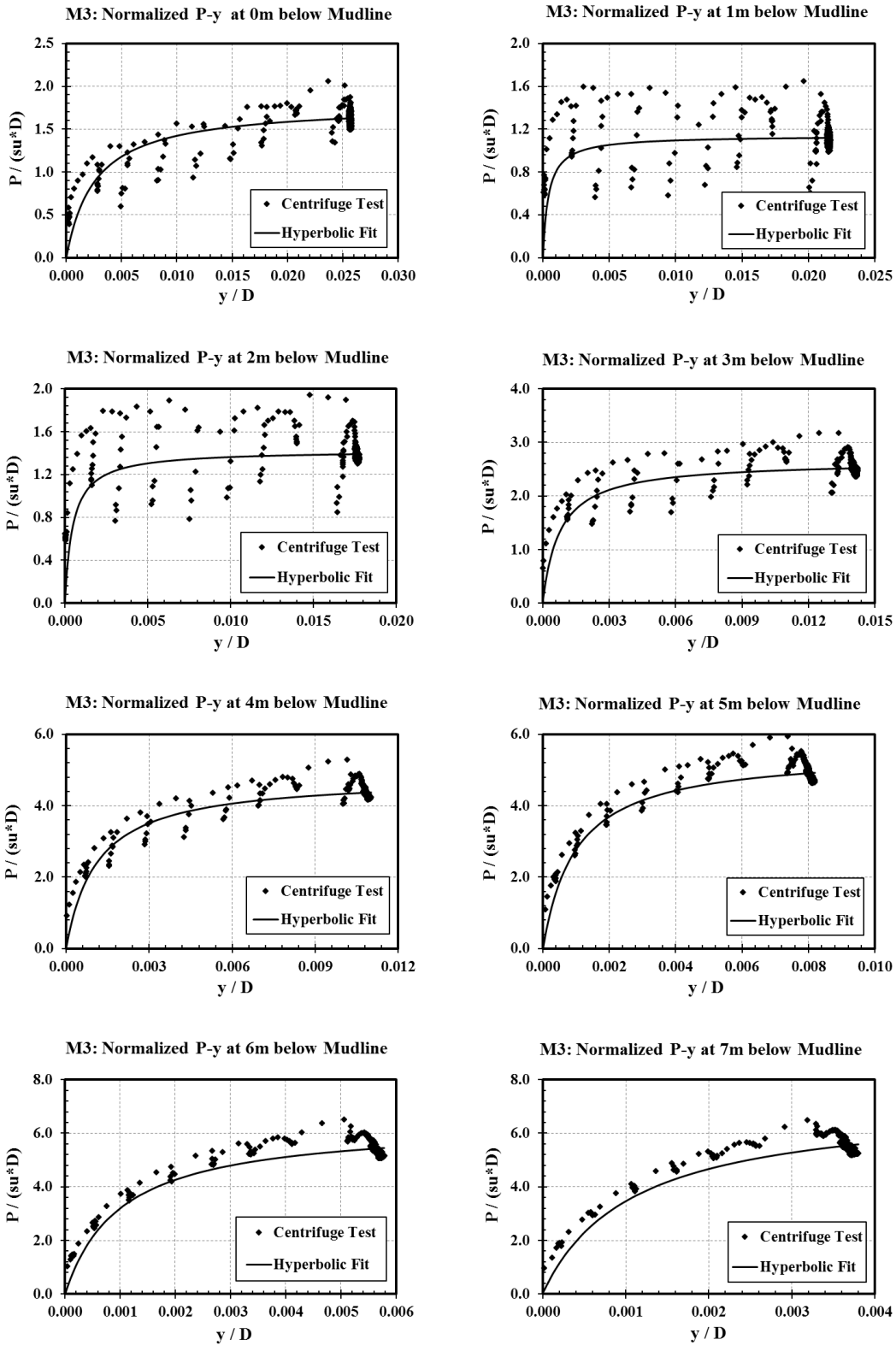


**Figure A.6: Soft Clay Initial Excursion curve fit for Test 3 (C3) M3 Motion.**

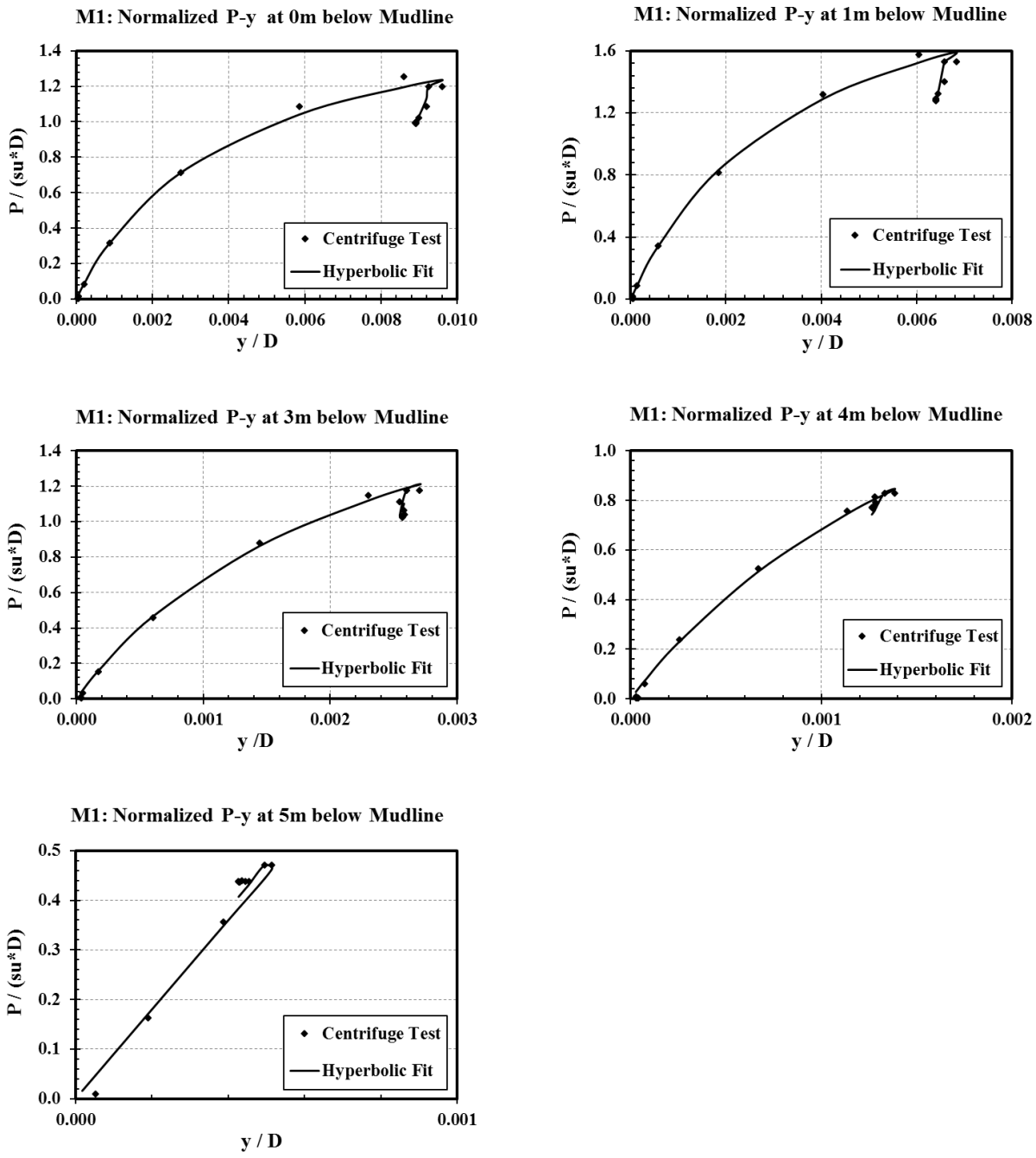


**Figure A.7: Stiff Clay Initial Excursion curve fit for Test 2 (C2) M1 Motion.**

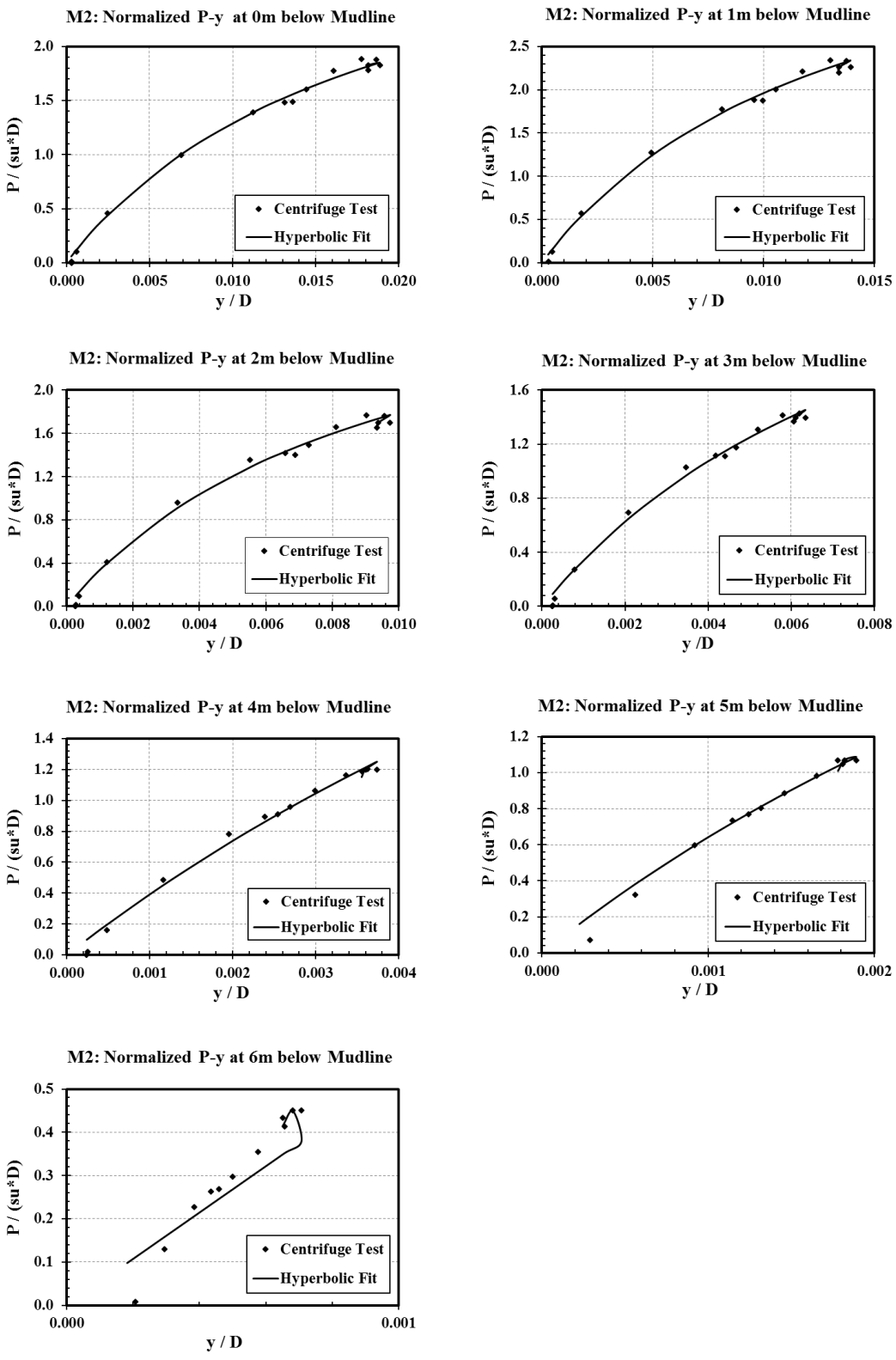


**Figure A.8: Stiff Clay Initial Excursion curve fit for Test 2 (C2) M2 Motion.**

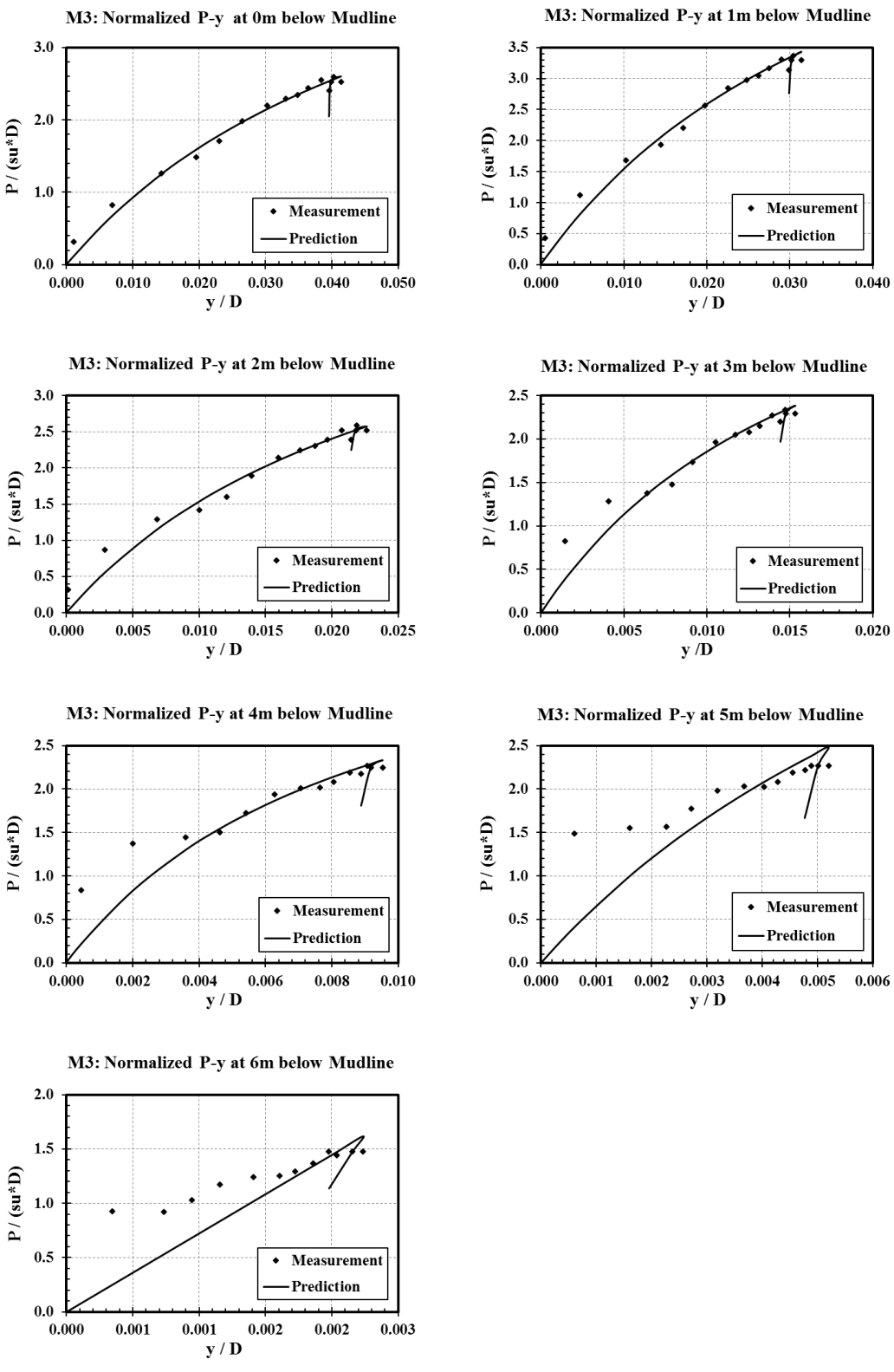


**Figure A.9: Stiff Clay Initial Excursion curve fit for Test 2 (C2) M3 Motion.**

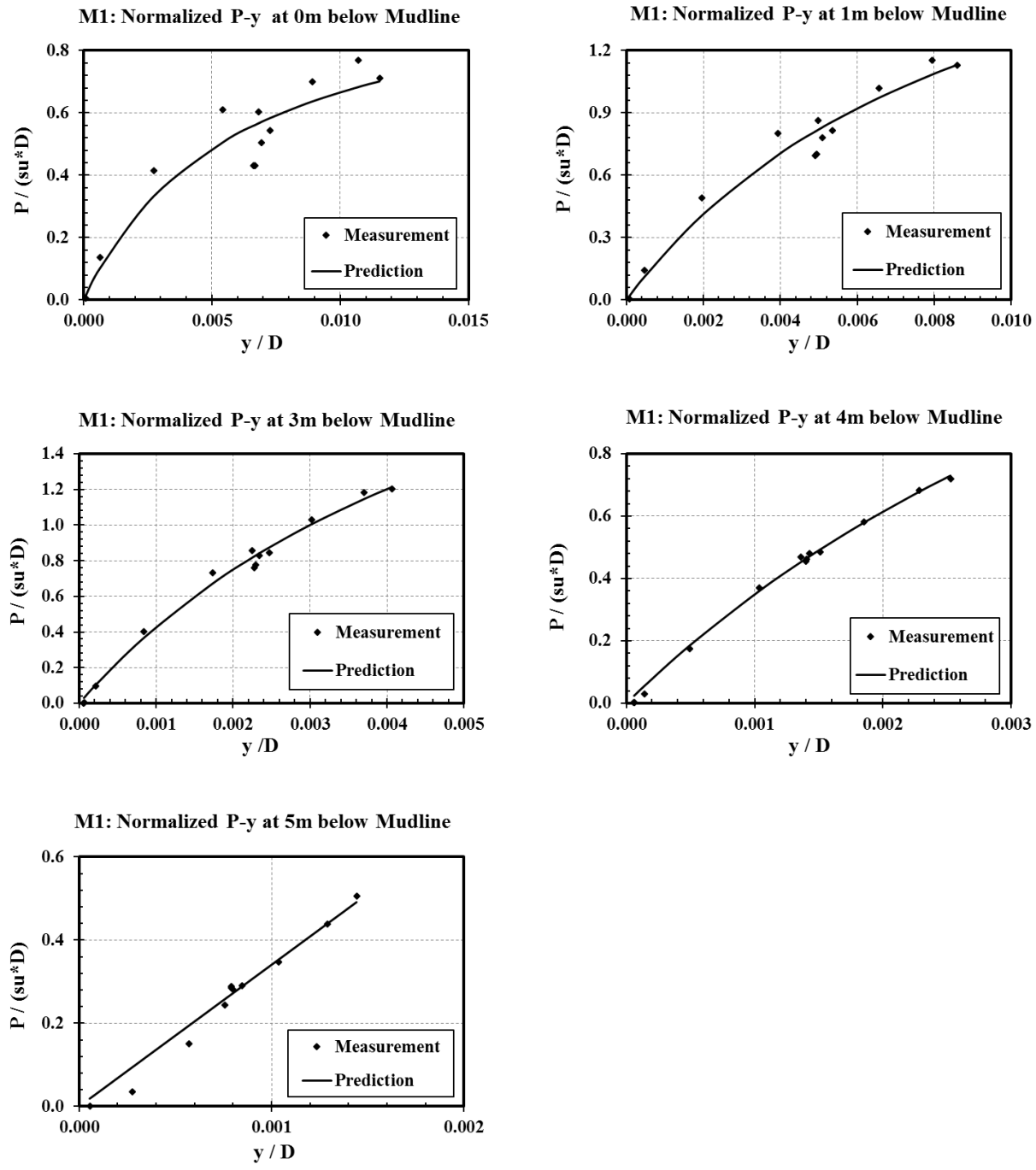


**Figure A.10: Stiff Clay Initial Excursion curve fit for Test 3 (C3) M1 Motion.**

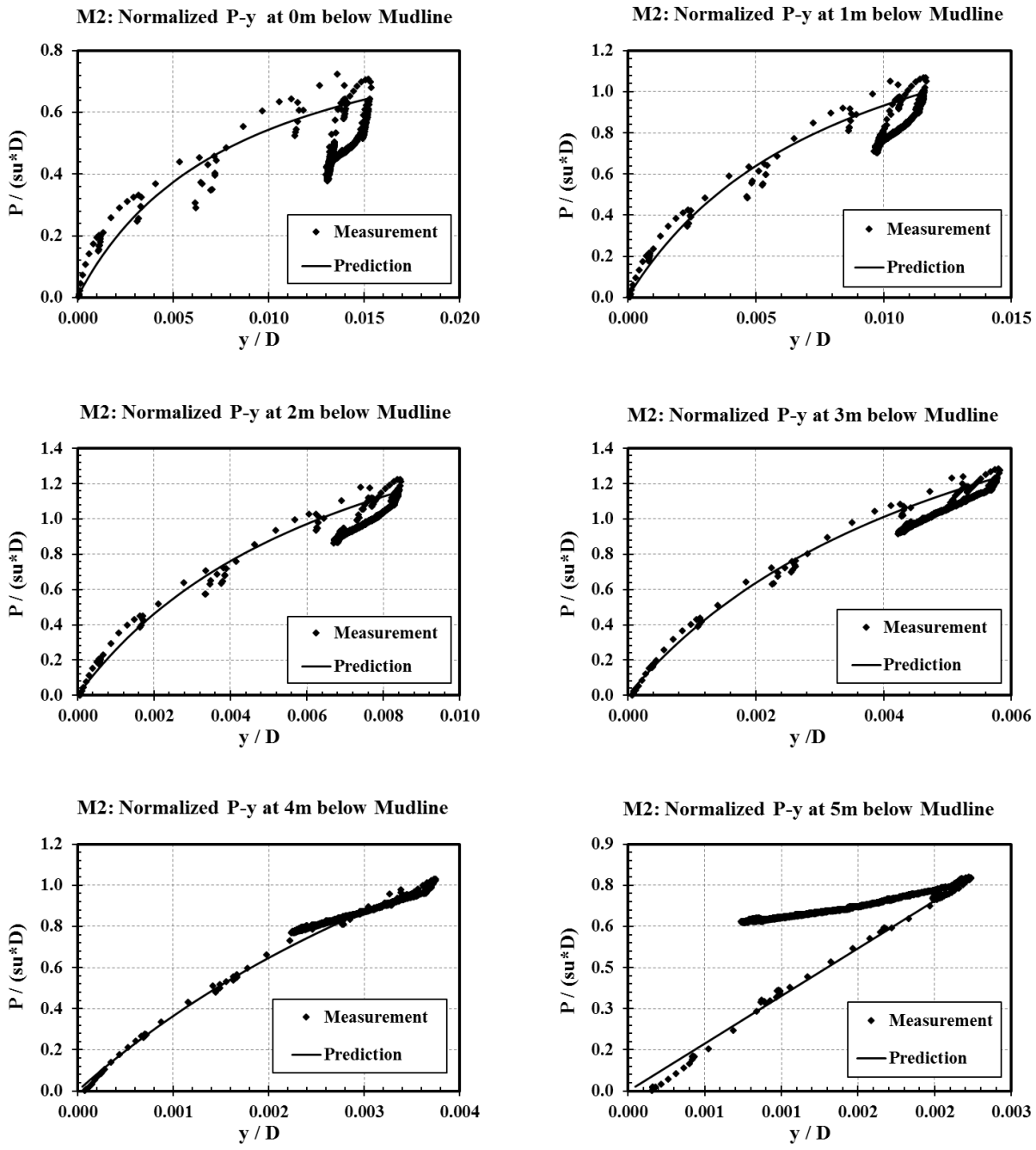


**Figure A.11: Stiff Clay Initial Excursion curve fit for Test 3 (C3) M2 Motion.**

# APPENDIX B

## POWER LAW CURVE FIT TO THE INITIAL UNLOAD CURVE

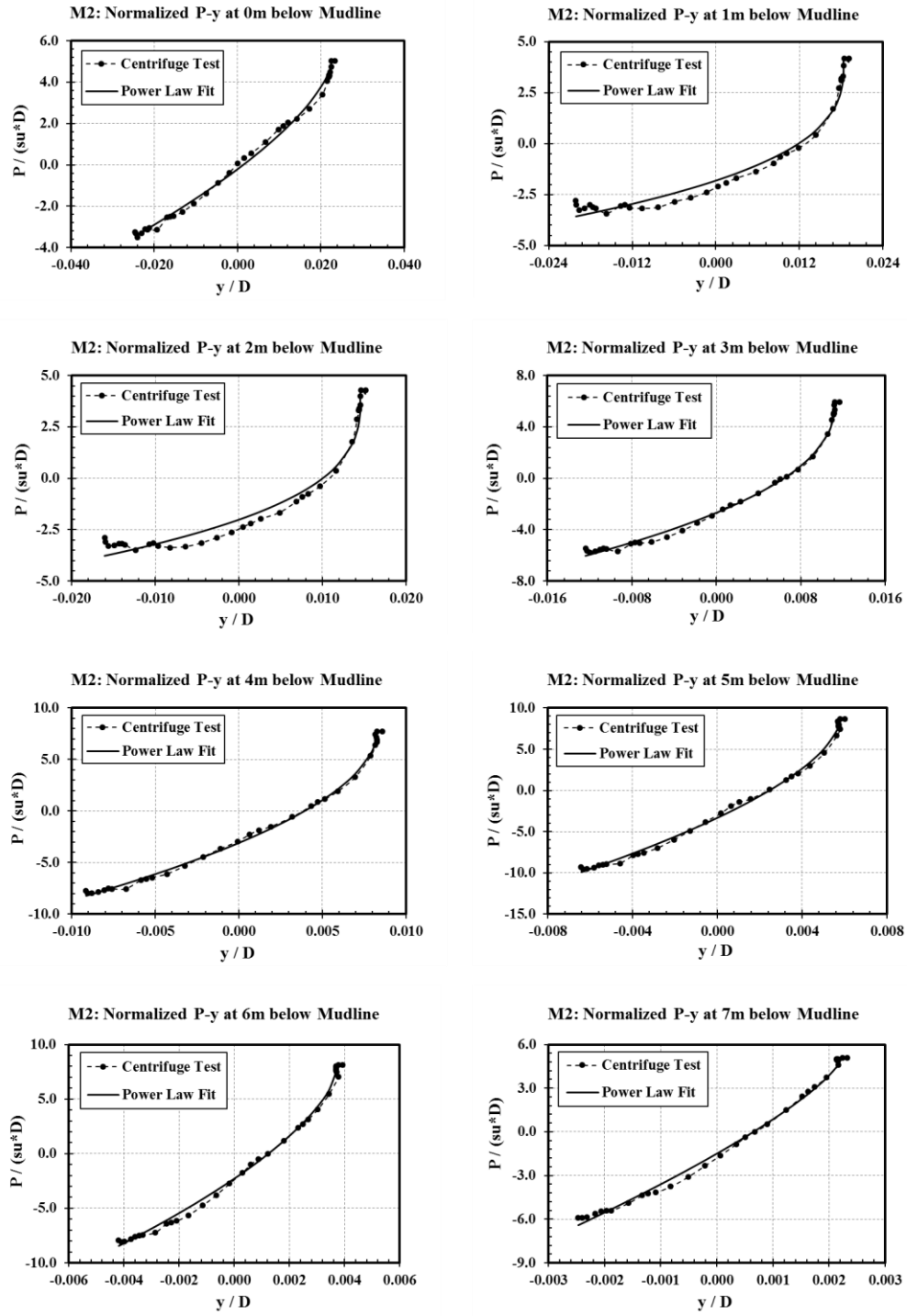


**Figure B.1: Soft Clay Initial Unload curve fit for Test 2 (C2) M2 Motion.**

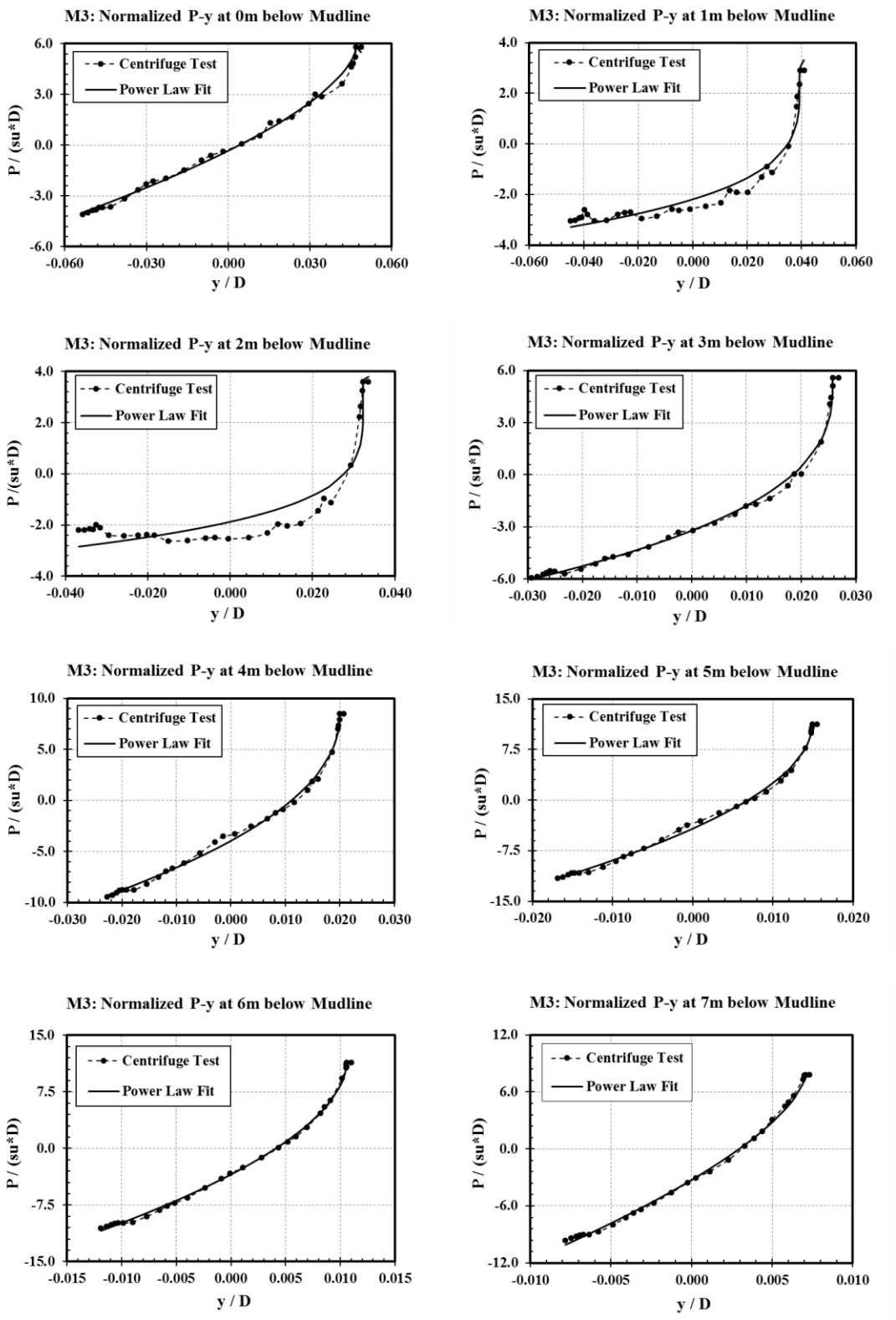


**Figure B.2: Soft Clay Initial Unload curve fit for Test 2 (C2) M3 Motion.**

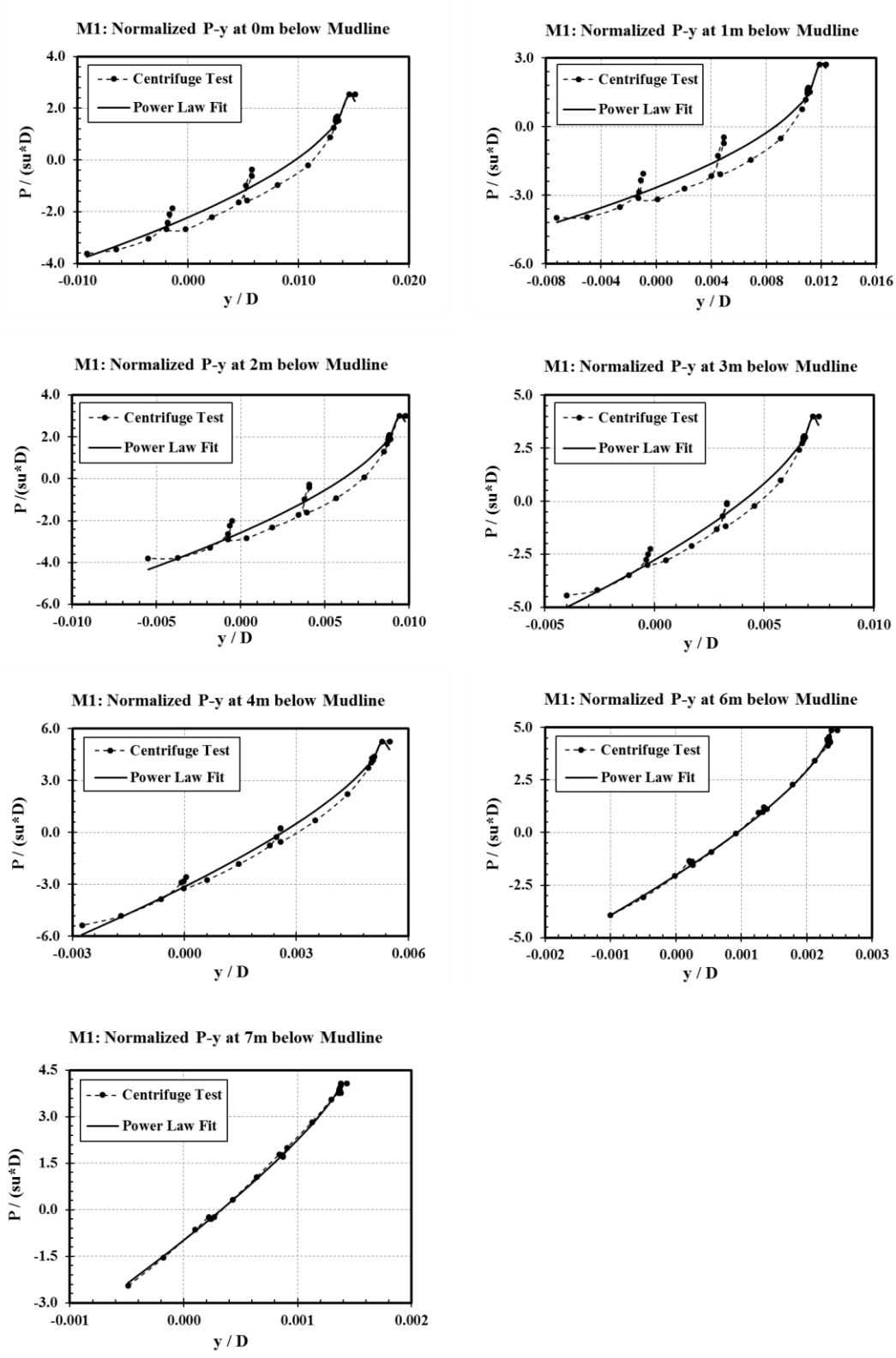


**Figure B.3: Soft Clay Initial Unload curve fit for Test 3 (C3) M1 Motion.**

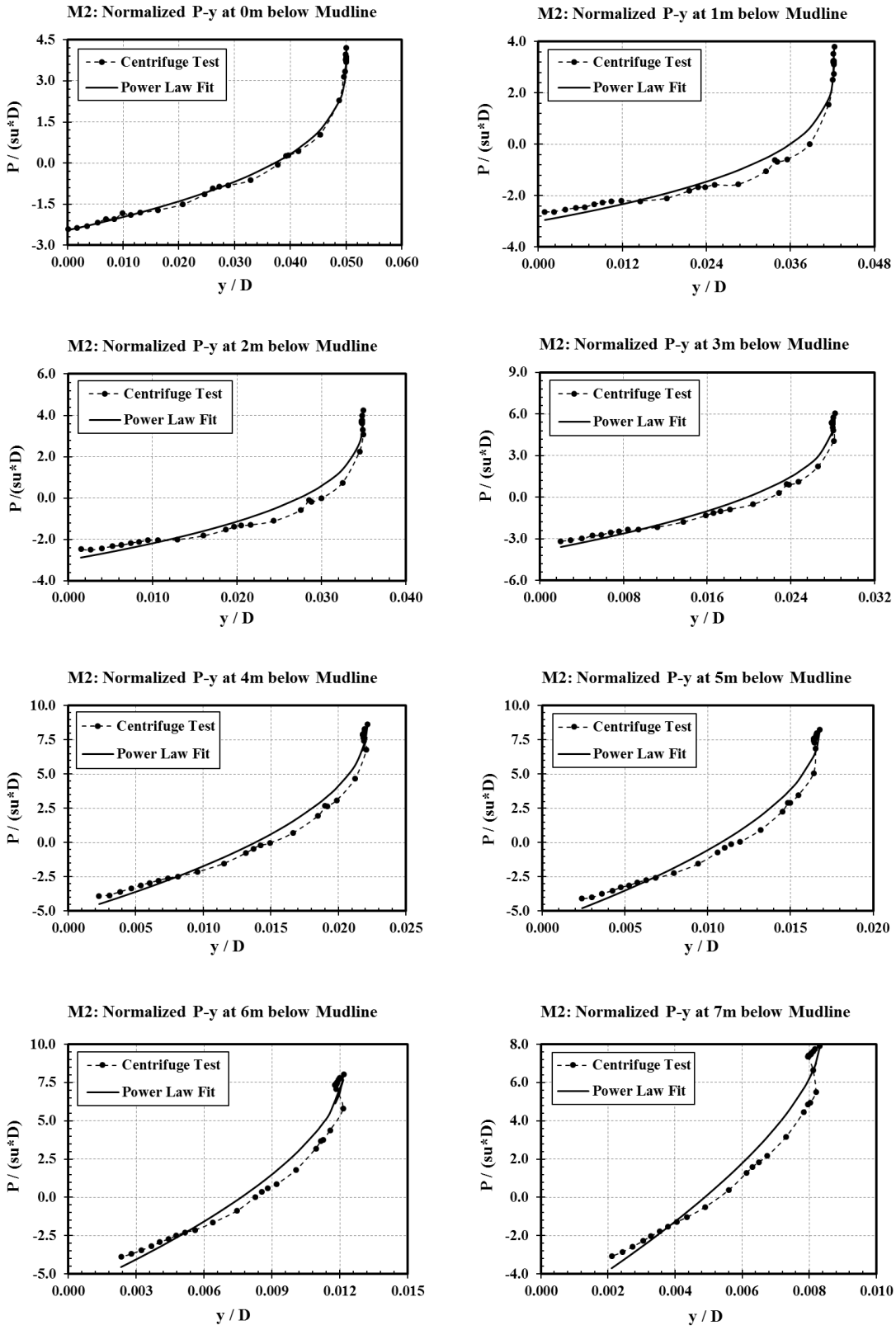


**Figure B.4: Soft Clay Initial Unload curve fit for Test 3 (C3) M2 Motion.**

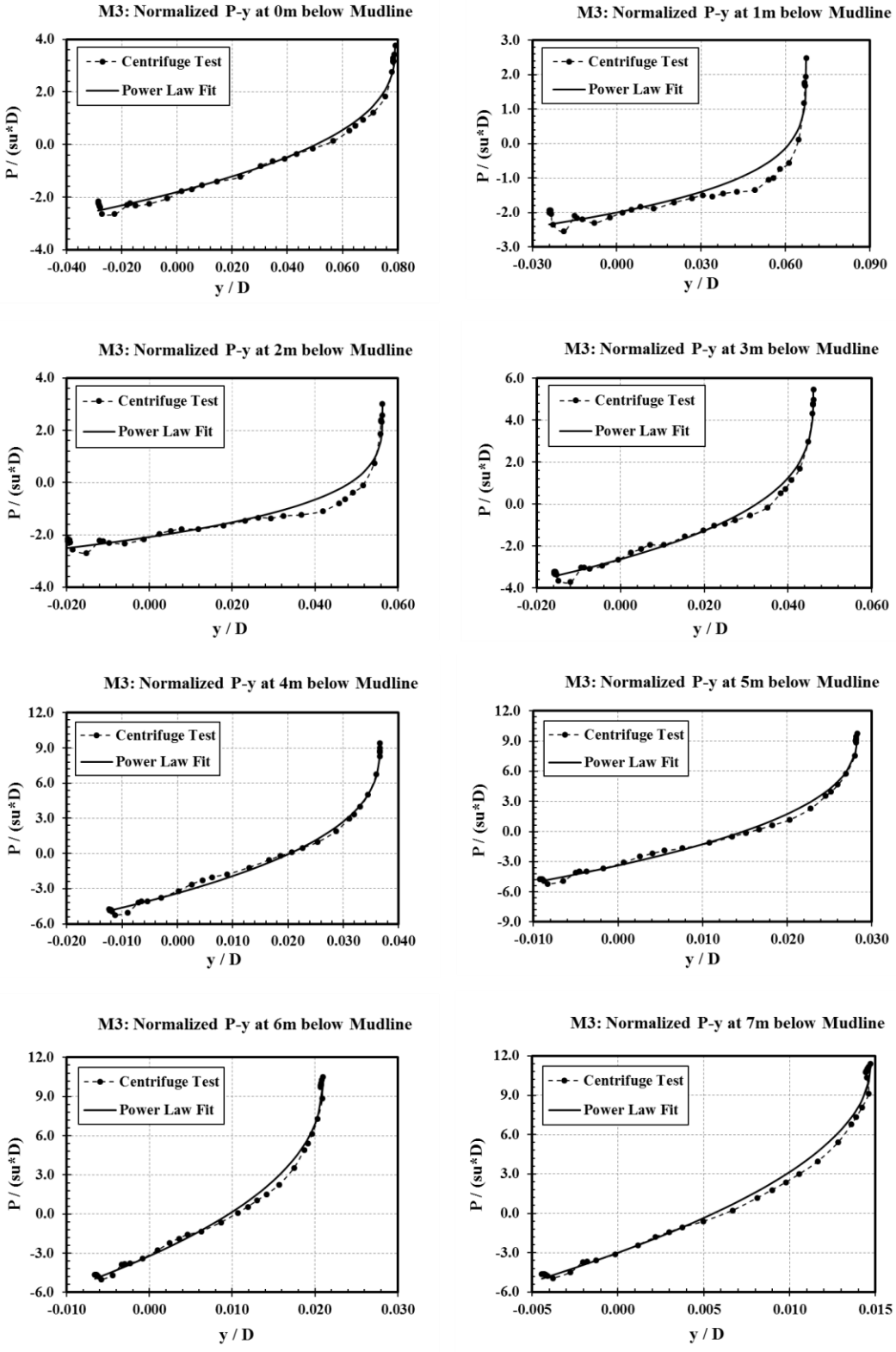


**Figure B.5: Soft Clay Initial Unload curve fit for Test 3 (C3) M3 Motion.**

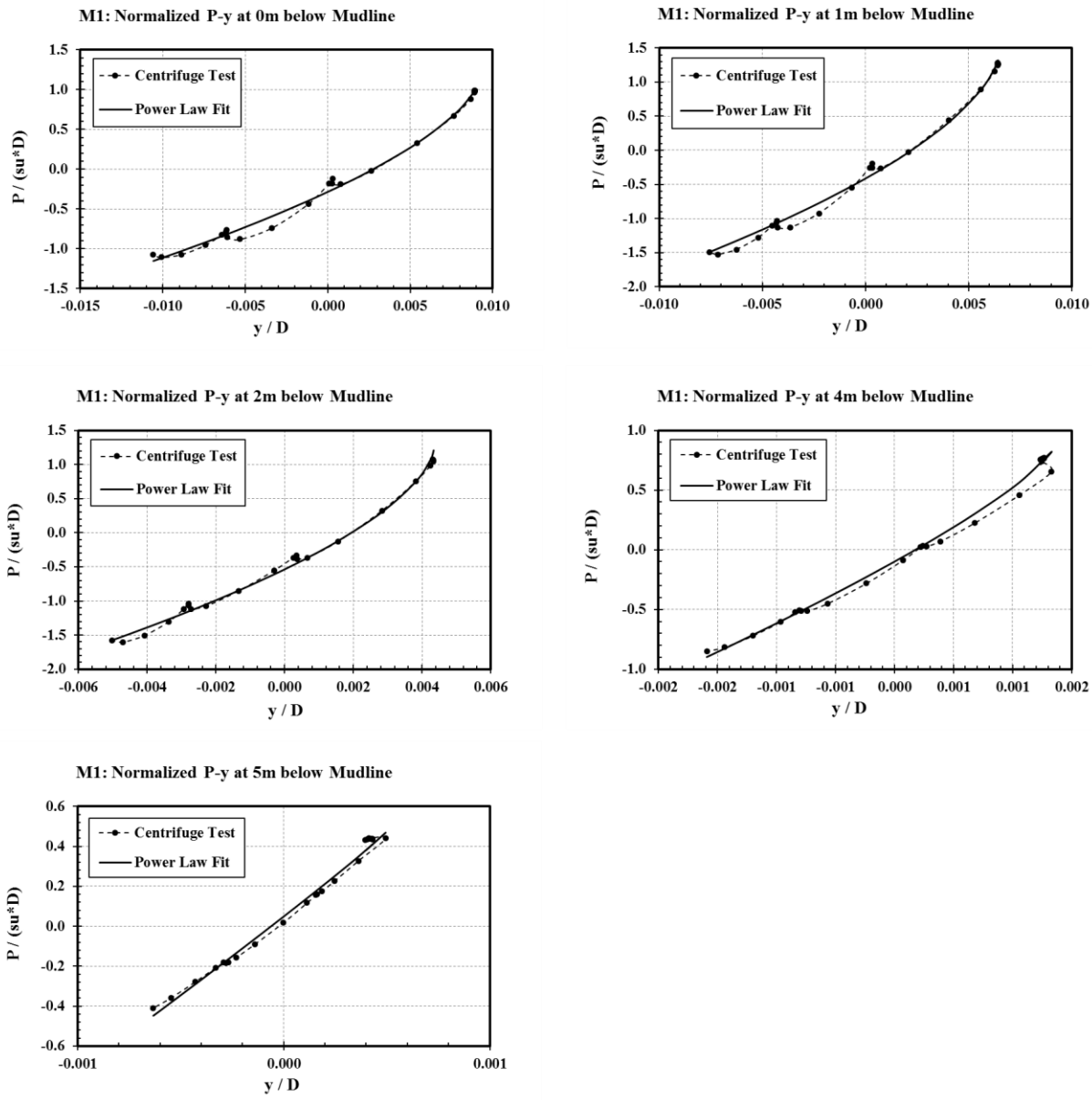


**Figure B.6: Stiff Clay Initial Unload curve fit for Test 2 (C2) M1 Motion.**

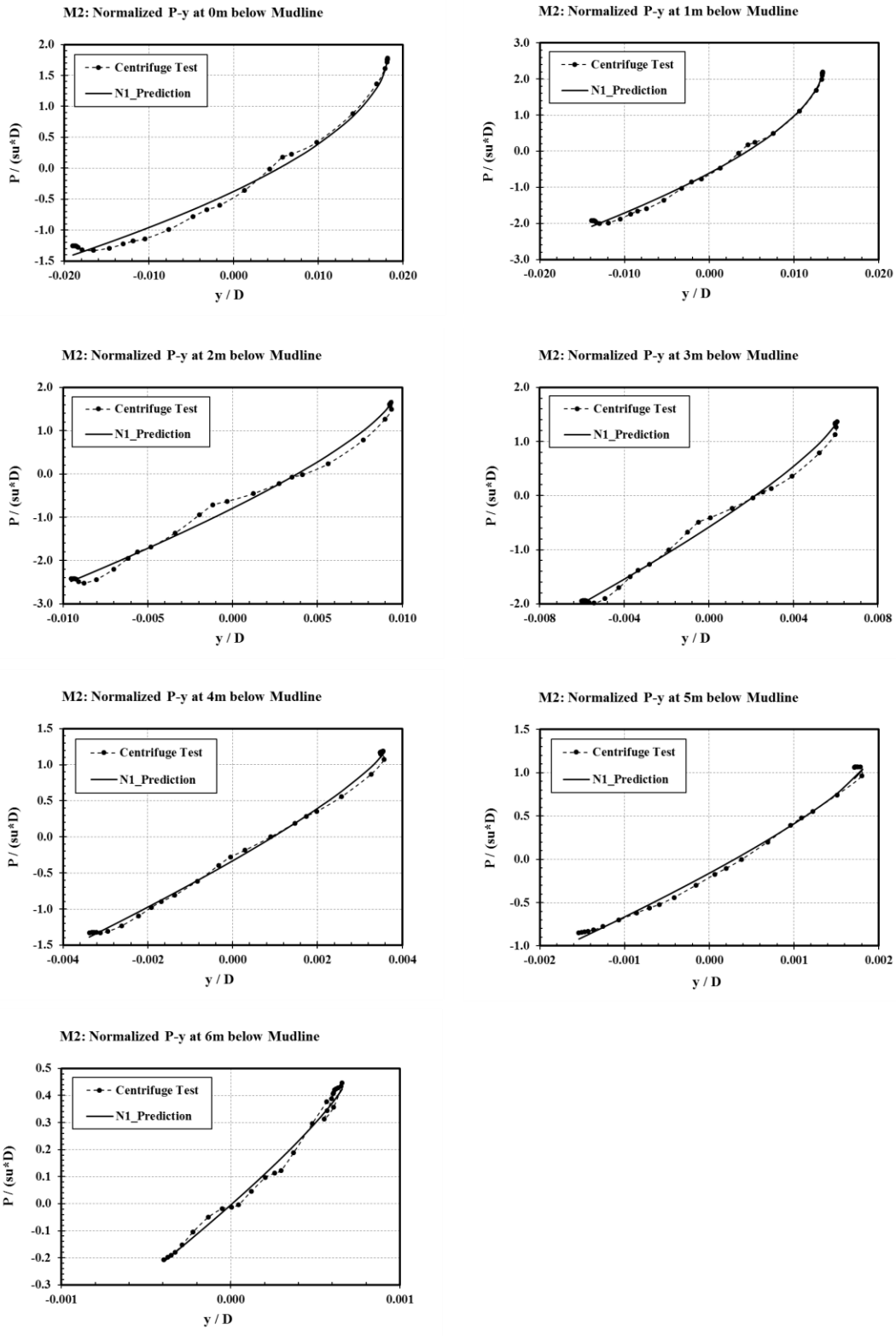


**Figure B.7: Stiff Clay Initial Unload curve fit for Test 2 (C2) M2 Motion.**

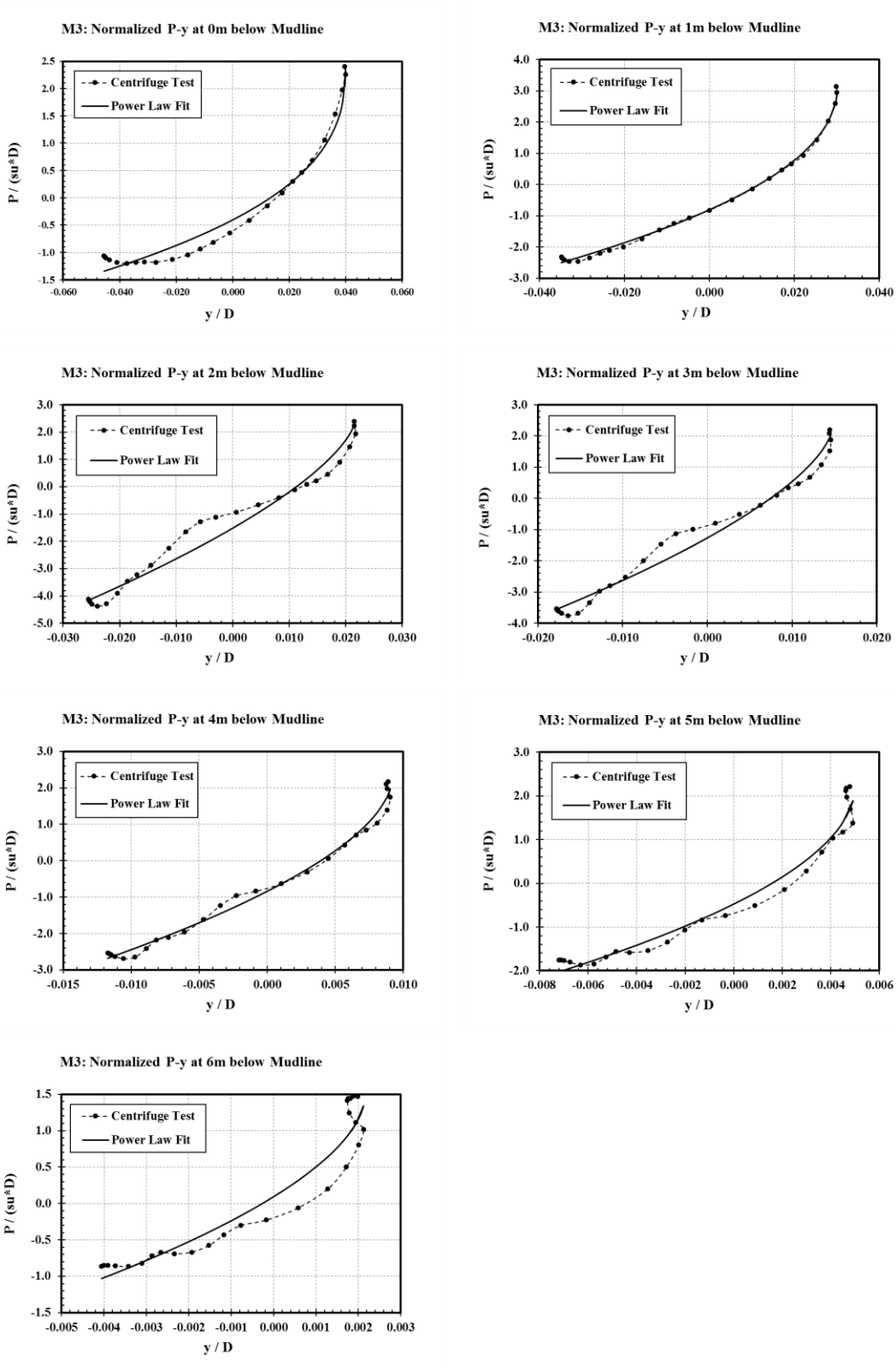


**Figure B.8: Stiff Clay Initial Unload curve fit for Test 2 (C2) M3 Motion.**

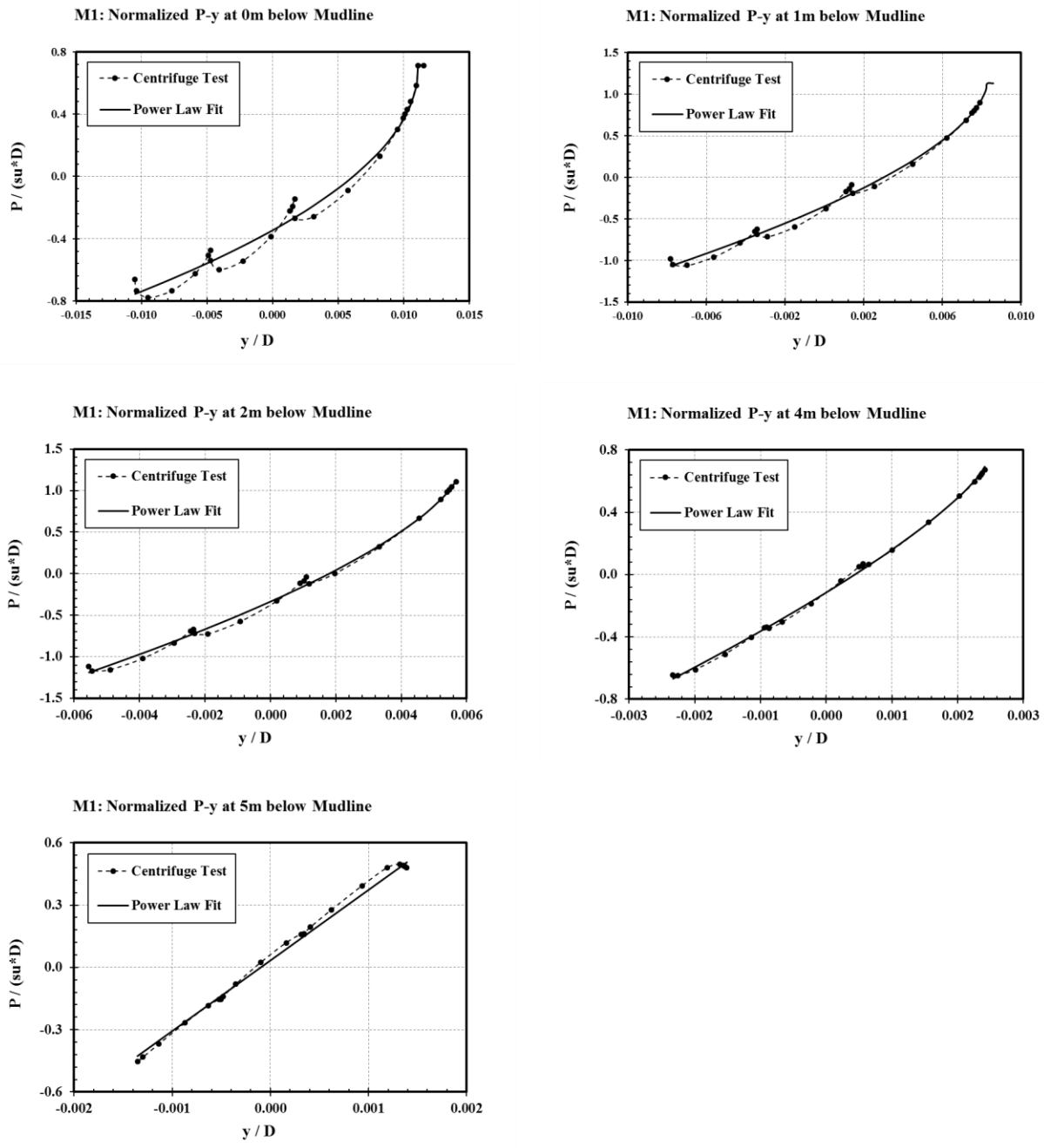


**Figure B.9: Stiff Clay Initial Unload curve fit for Test 3 (C3) M1 Motion.**

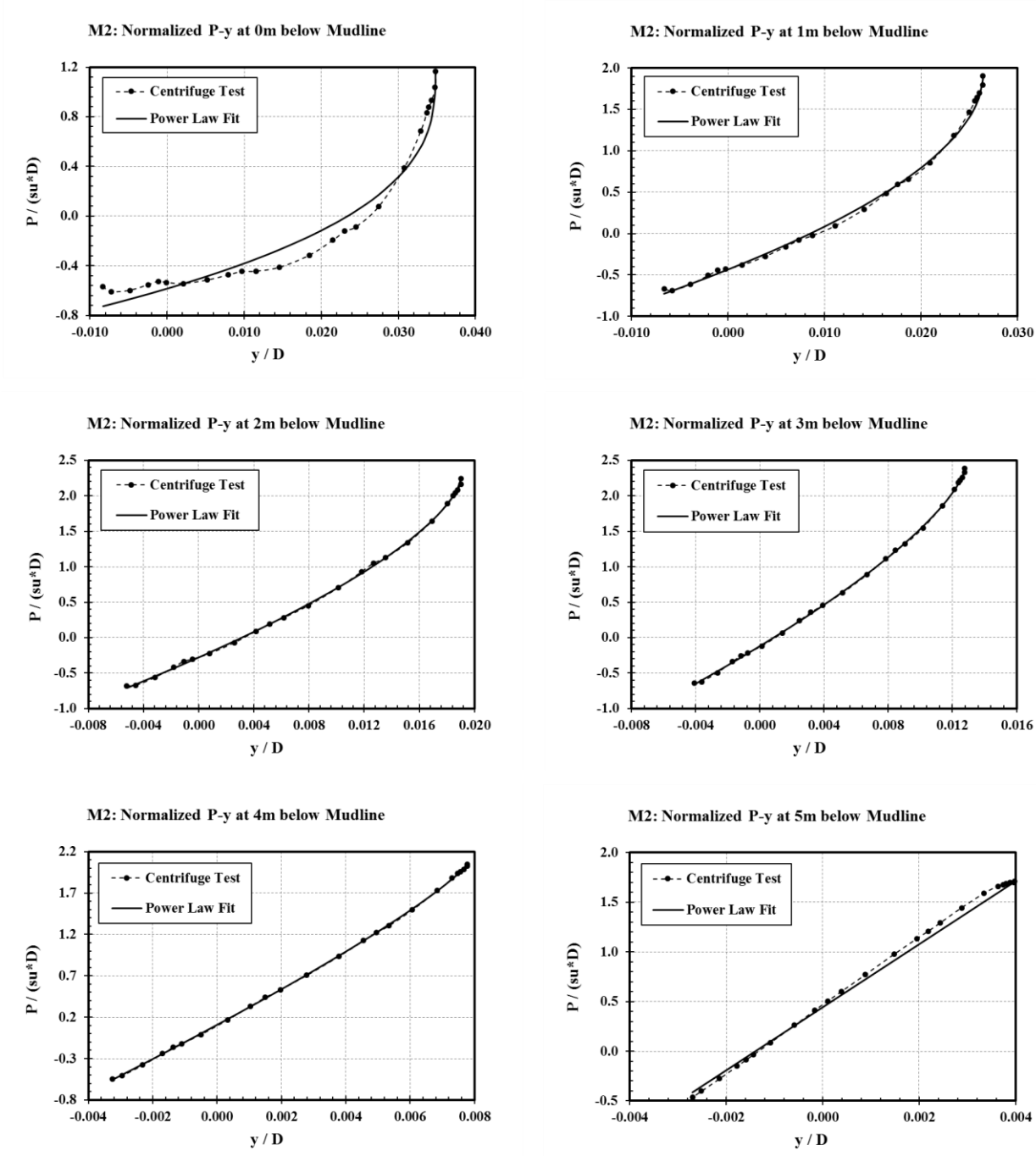


**Figure B.10: Stiff Clay Initial Unload curve fit for Test 3 (C3) M2 Motion.**

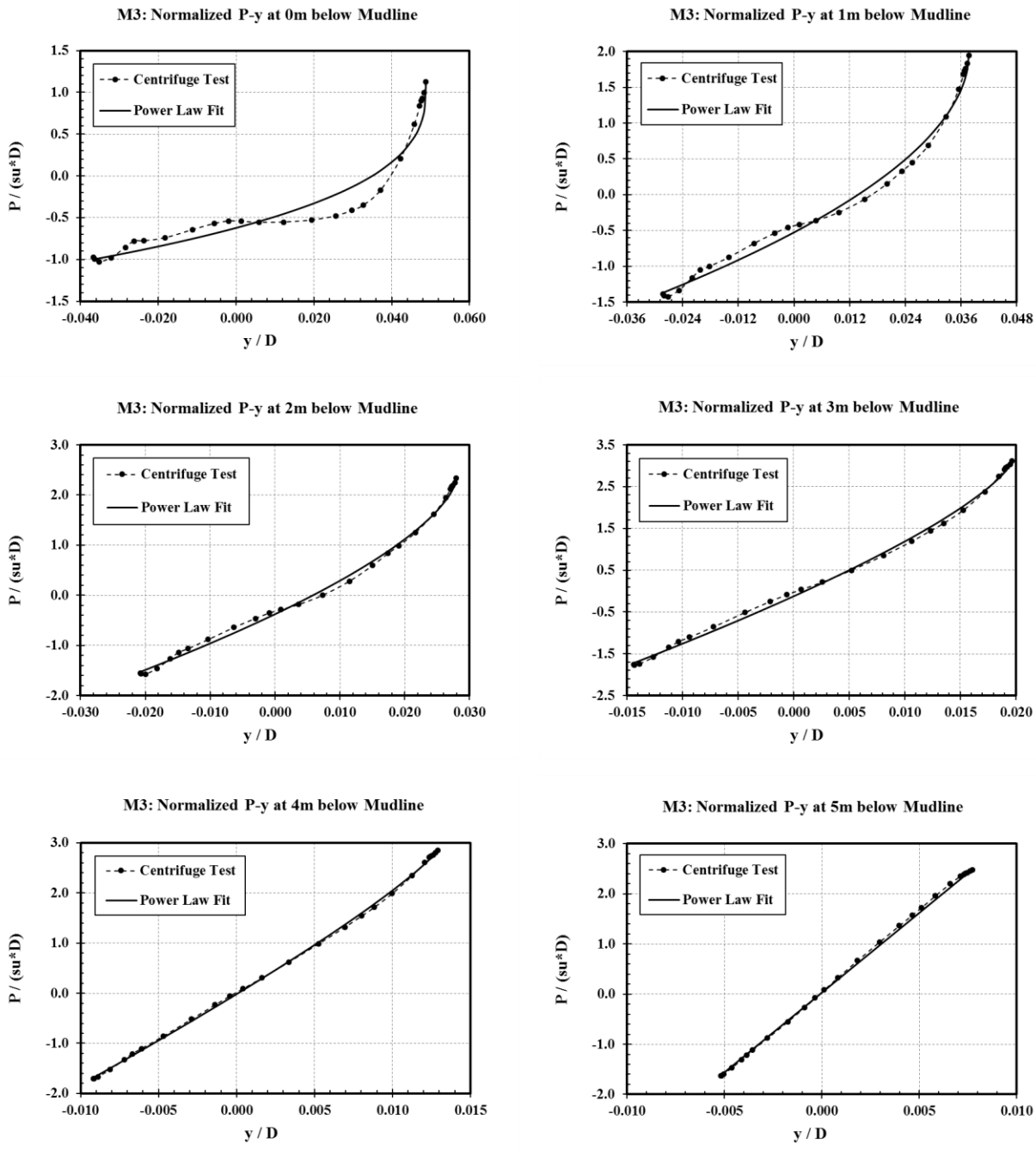


**Figure B.11: Stiff Clay Initial Unload curve fit for Test 3 (C3) M3 Motion.**

# APPENDIX C

## ANALYSIS OF LATERALLY LOADED PILE

The analysis solves the fourth order differential equation:

$$EI \frac{d^2y}{dz^2} + K_{sec} y = 0 \qquad \text{Eq. C. 1}$$

where E = elastic modulus of pile

I = moment of inertia of pile

y = lateral displacement of pile

z = depth

$k_{sec}$ = secant stiffness of soil spring

This equation is subject to the following boundary constraints for a pile of length L:

| | | |
|---|---|---|
| Imposed displacement δ at pile head: | y (0) = δ | Eq. C. 2 |
| Zero moment at pile head: | y'' (0) = 0 | Eq. C. 3 |
| Zero moment at pile tip: | y'' (L) = 0 | Eq. C. 4 |
| Zero displacement at pile tip: | y (L) = 0 | Eq. C. 5 |

Eq. C. 1 is solved with finite difference methods by discretizing the pile into n segments of length $\Delta z = \frac{L}{n}$, which will generate n + 1 equations. Equations 3 through n-2 have the form:

Equation i: $$y_{i-2} - 4\,y_{i-1} + \left(6 + K_{sec}\frac{\Delta z^4}{EI}\right) y_i - 4y_{i+1} + y_{i+2} = 0 \qquad \text{Eq. C. 6}$$

The four boundary constraints are provided through the following additional equations:

$$y_1 = \delta \qquad \text{Eq. C. 7}$$

$$y_1 - 2y_2 + y_3 = 0 \qquad \text{Eq. C. 8}$$

$$y_{n-2} - 2y_{n-1} + y_n = 0 \qquad \text{Eq. C. 9}$$

$$y_n = 0 \qquad \text{Eq. C. 10}$$

If one chooses to impose a force F rather than displacement a displacement at the pile head, Eq. C. 7 may be replaced with the following 3rd order finite difference equation:

$$-y_1 + 3y_2 - 3y_3 + y_4 = F\,\frac{\Delta z^3}{EI} \qquad \text{Eq. C. 11}$$

Eqns. C. 6 through C. 10 (or C. 8 through C. 11) comprise a non-singular matrix equation that can be solved directly through Gauss elimination.

Finally, bending moments at any location along the pile can be computed from:

$$M_i = EI\,(y_{i-1} - 2y_i + y_{i+1}) \qquad \text{Eq. C. 12}$$

Eqn. C. 6 is nonlinear due to the dependence of the secant stiffness $k_{sec}$ on displacement. The solution algorithm proceeds iteratively according to the following sequence:

1. Estimate a displacement distribution for iteration j, $y_j(z)$. For the first estimate, assume displacement varies linearly from $y = \delta$ at the pile head to $y = 0$ at the tip.
2. Compute secant stiffness along the depth of the pile using Eq. 2.
3. Construct the system of equations defined by Eqs. C. 7 - C. 10.
4. Solve for displacement for iteration j+1, $y_{j+1}(z)$.
5. Compute the maximum difference between bending moments in iterations j and j+1. If the difference is within tolerance, the solution has converged. If not, repeat Steps 1-5 with the updated displacement distribution $y_{j+1}(z)$. A tolerance of 1E-10 was used in this study.

It is noted that the pile head displacements (or forces) used in the back analysis are not absolute displacements, rather, they are the amplitude of the cyclic component of loading. In the analysis

of a given load cycle from the centrifuge tests, the cyclic component of displacement at the pile head was taken as: $\delta = (y_{max} - y_{min})$ Eq. C. 13

Where, $y_{max}$ and $y_{min}$ are the maximum and minimum measured displacements at the pile head. Similarly, the moments in Eqn. C. 12 denote the cyclic component of moments occurring in the pile. The computed cyclic moments should be compared to measured cyclic moments, which were computed from measured moments as follows:

$M_{cyc} = (M_{max} - M_{min})$ Eq. C. 14

# APPENDIX D

## P-Y Curves for Soft Clay Soil

*Test 2 (Motion 2)*

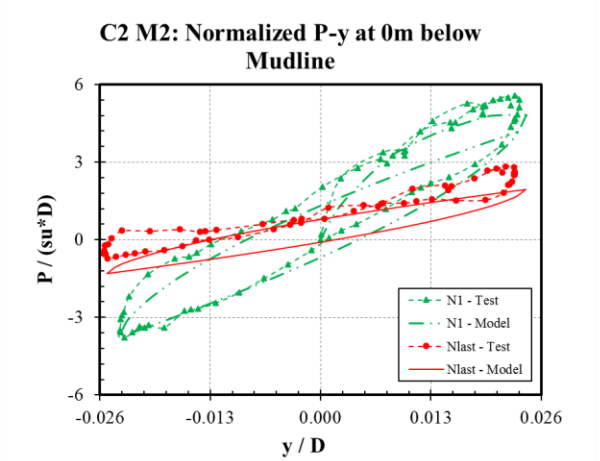


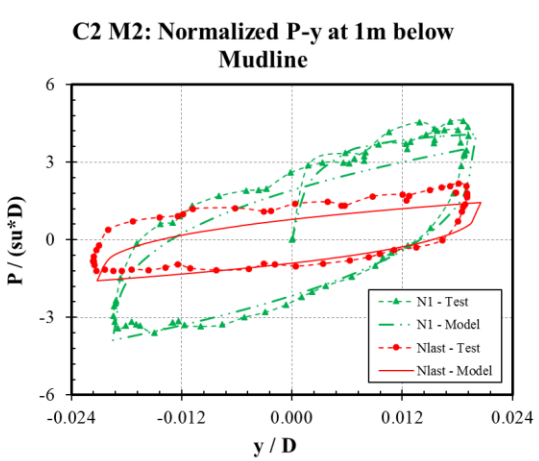


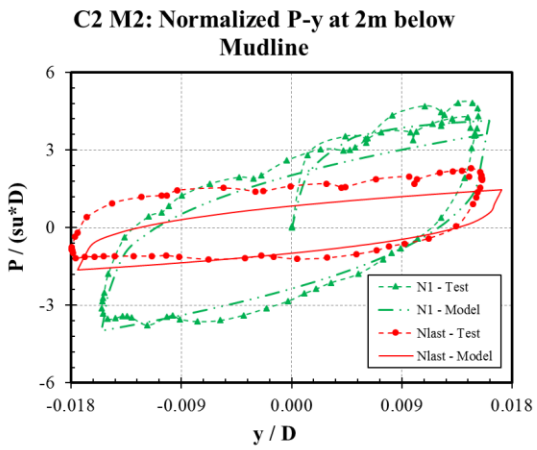


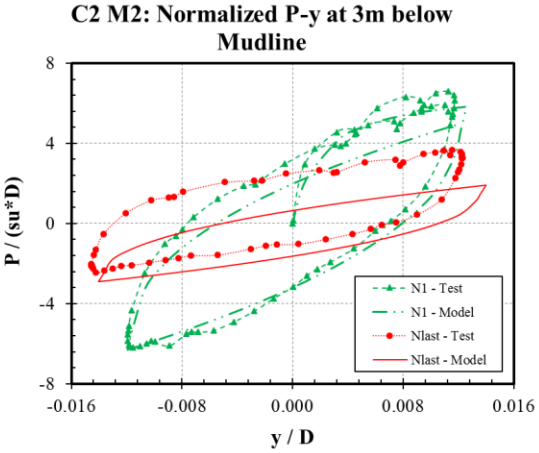


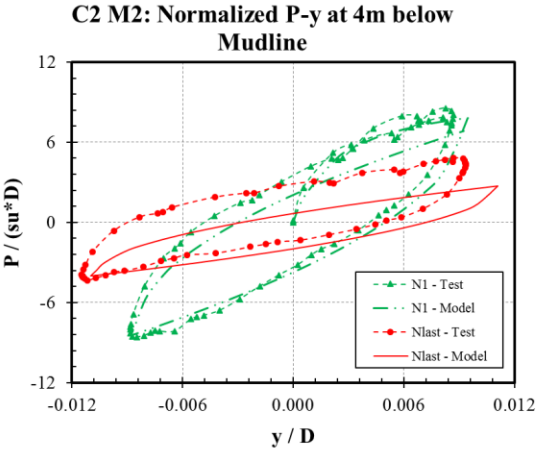


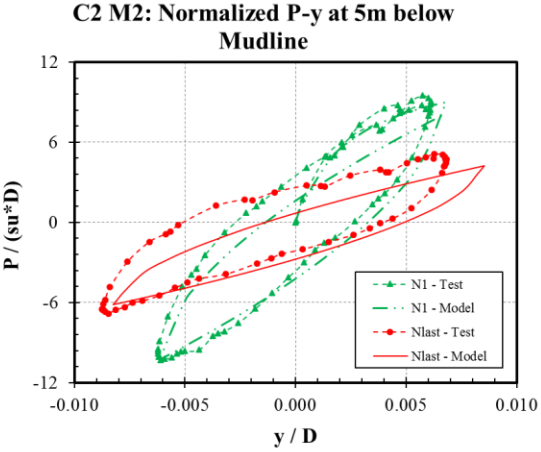

*Test 2 (Motion 3)*

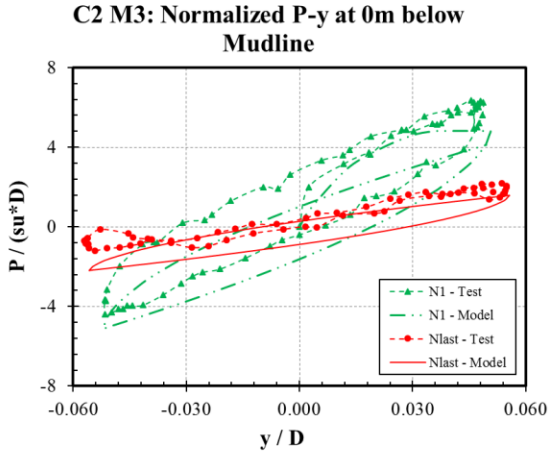


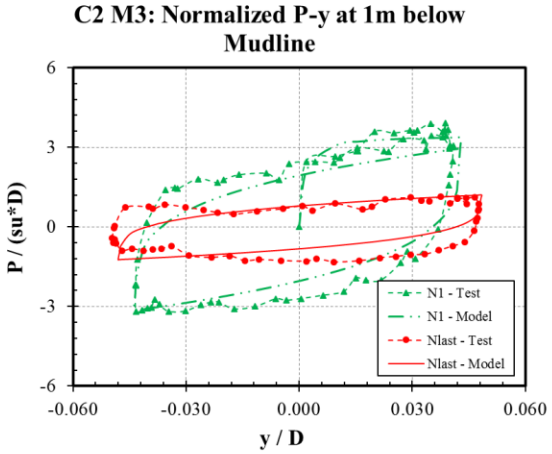


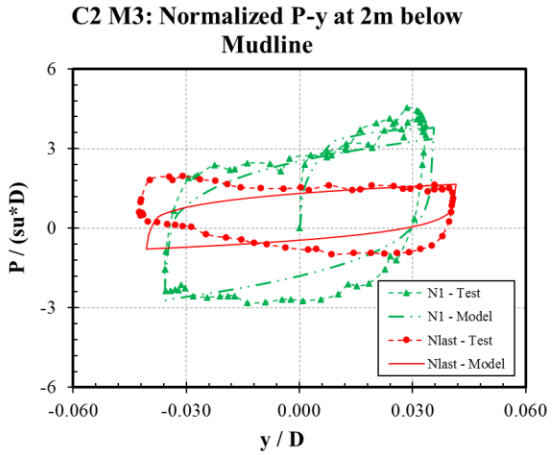


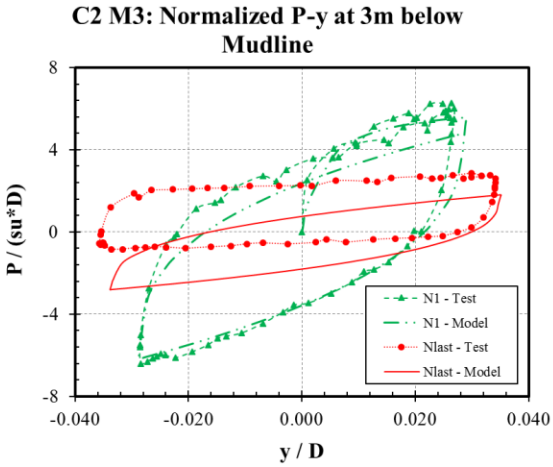


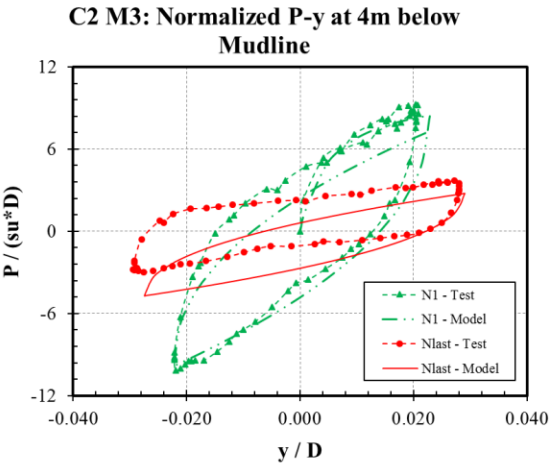


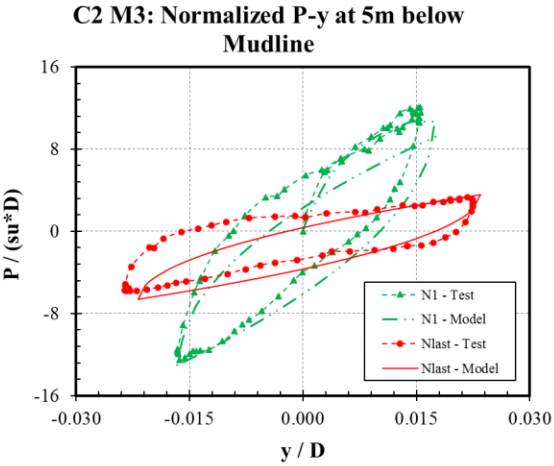

*Test 3 (Motion 1)*

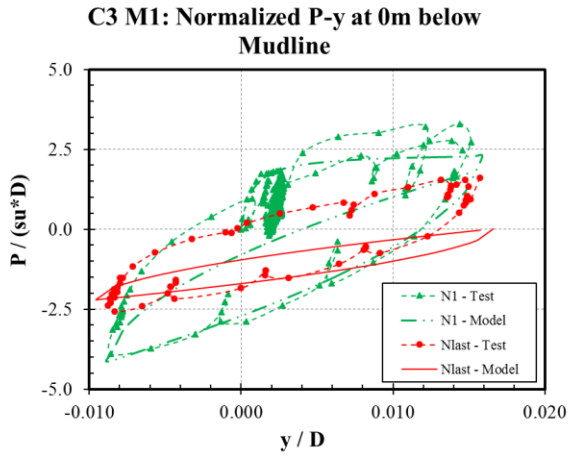


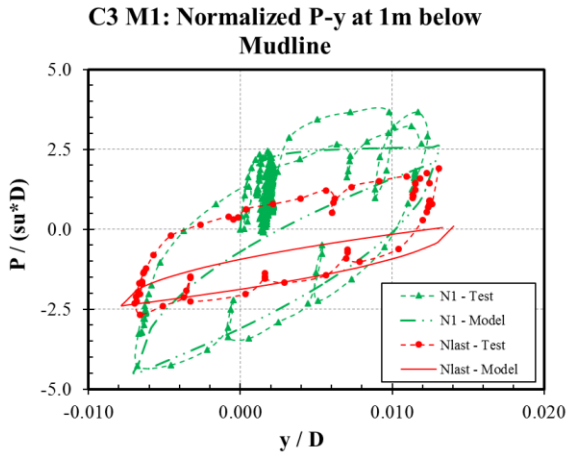


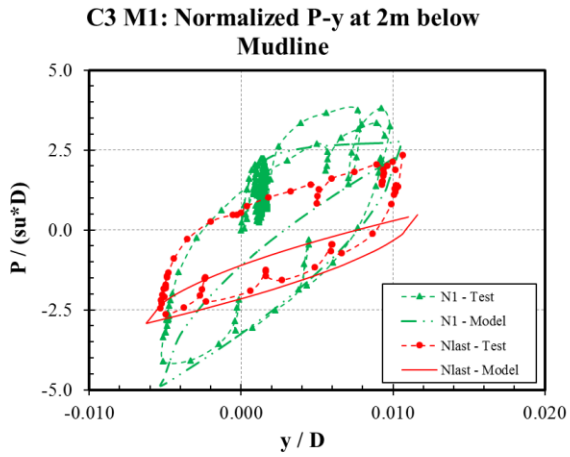


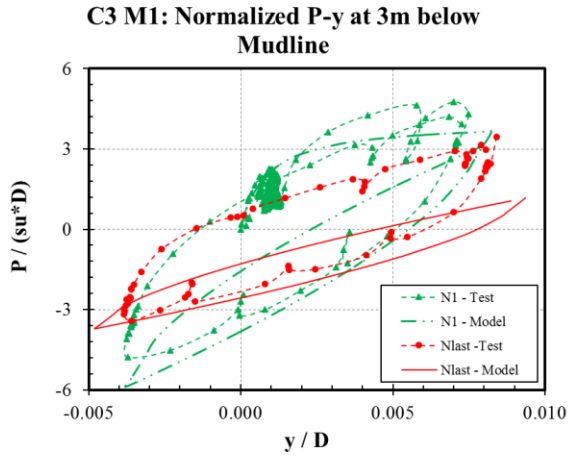


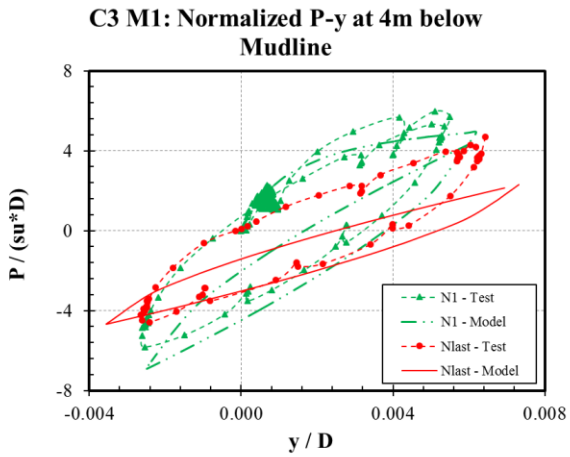


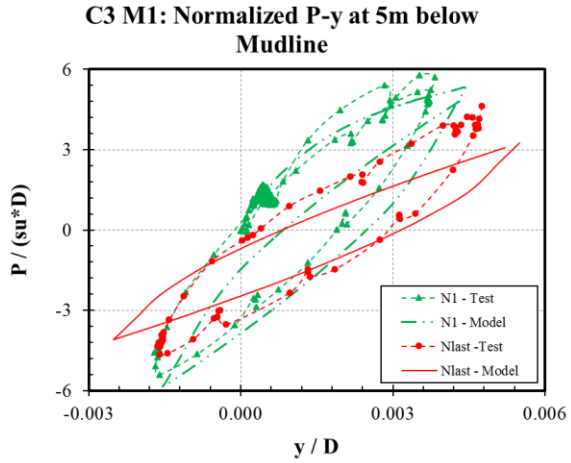

*Test 3 (Motion 2)*

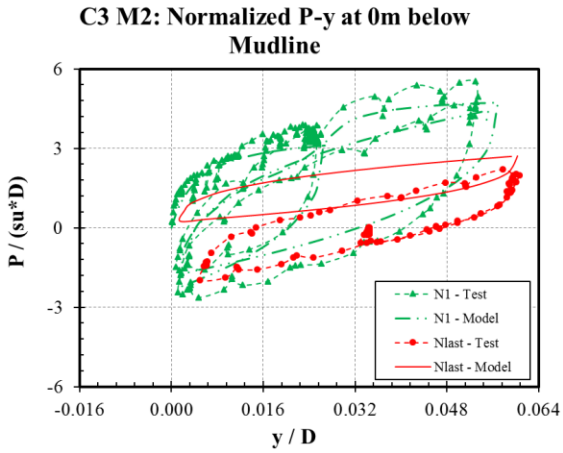


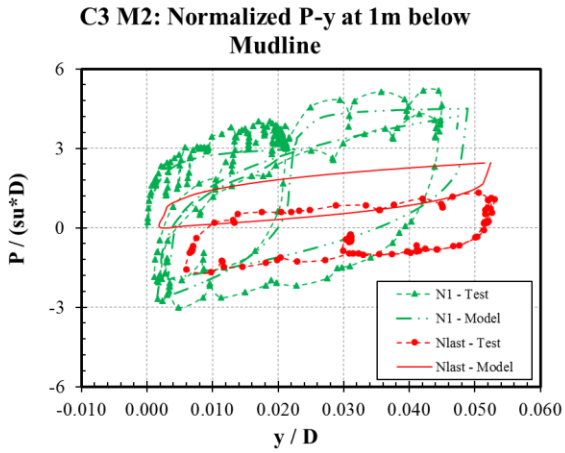


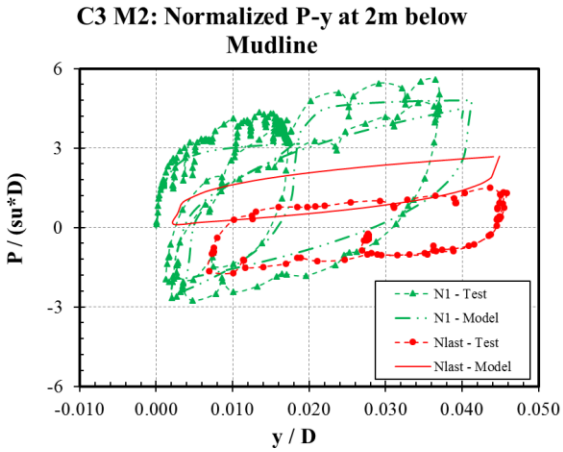


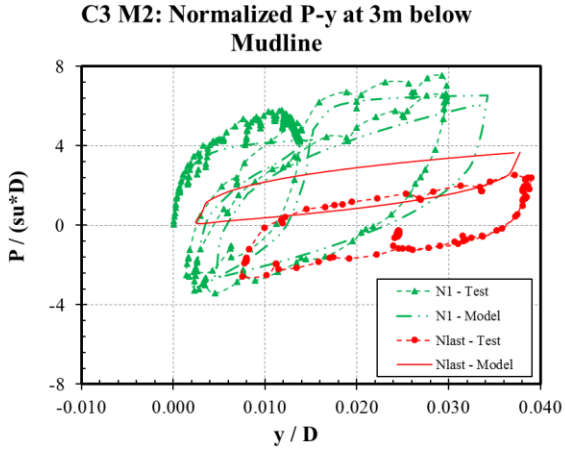


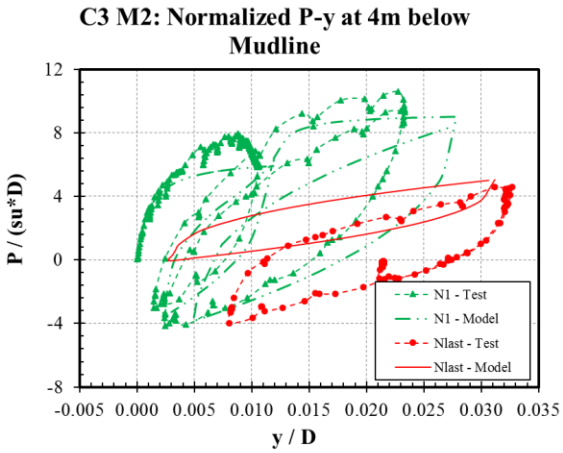


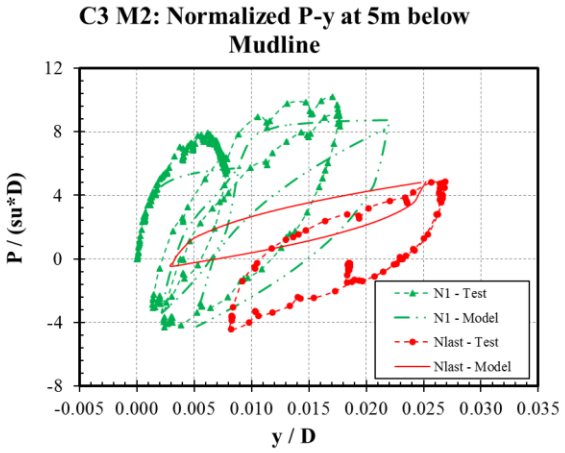

*Test 3 (Motion 3)*

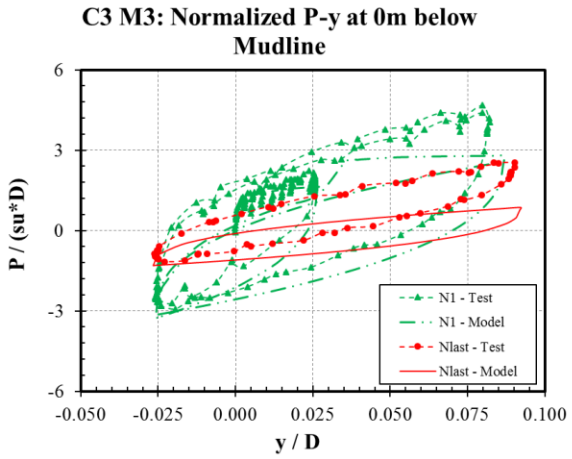


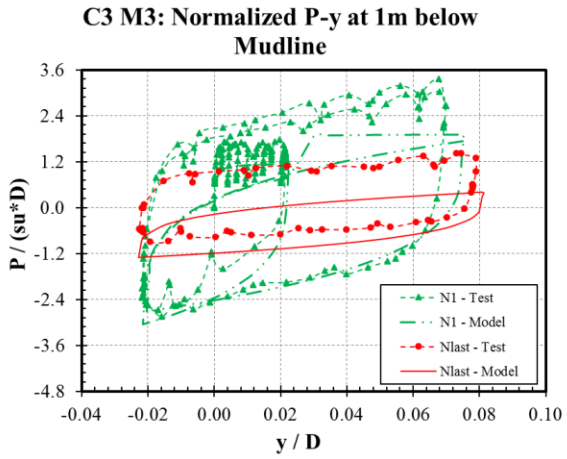


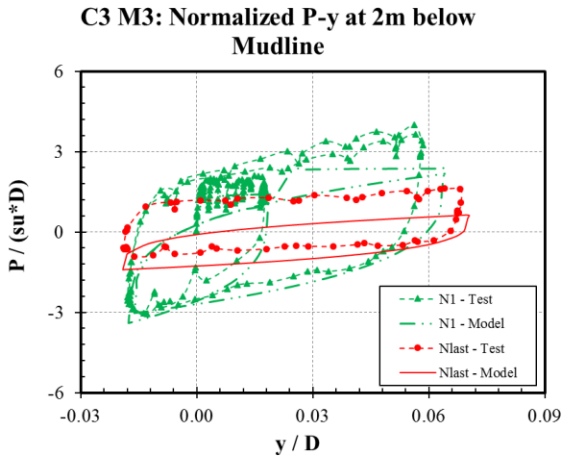


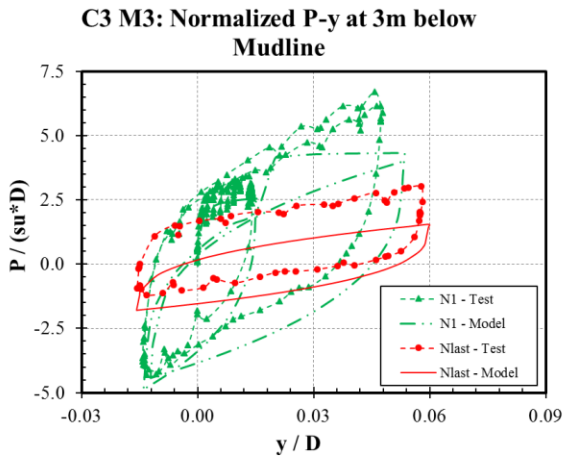


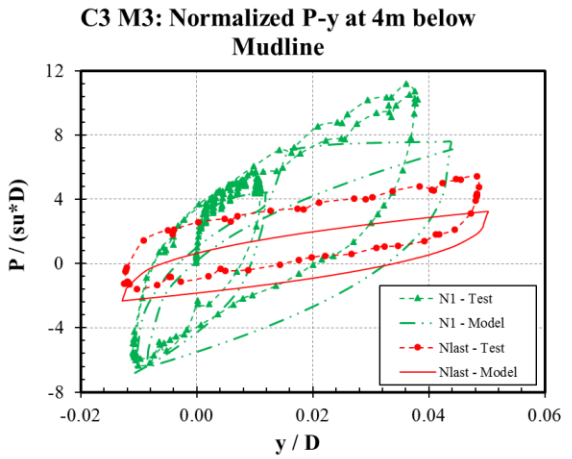


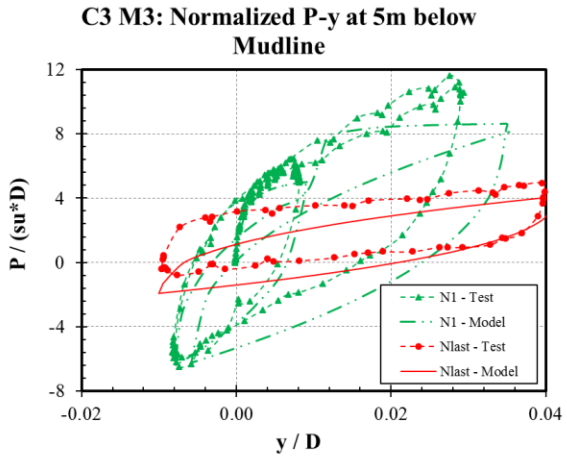

P-Y Curves for Stiff Clay Soil

*Test 2 (Motion 2)*

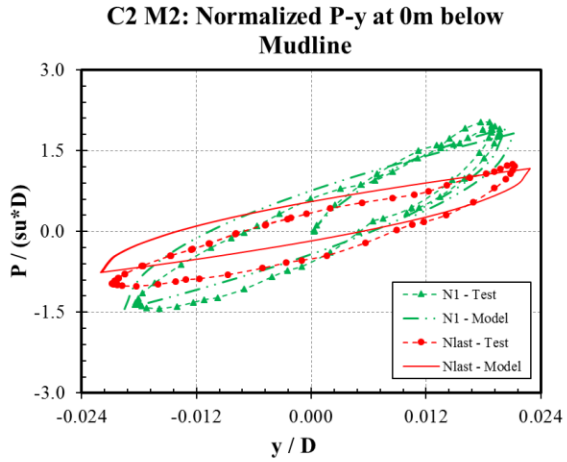


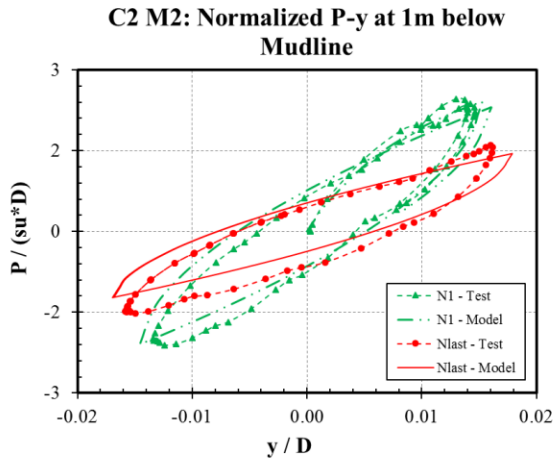


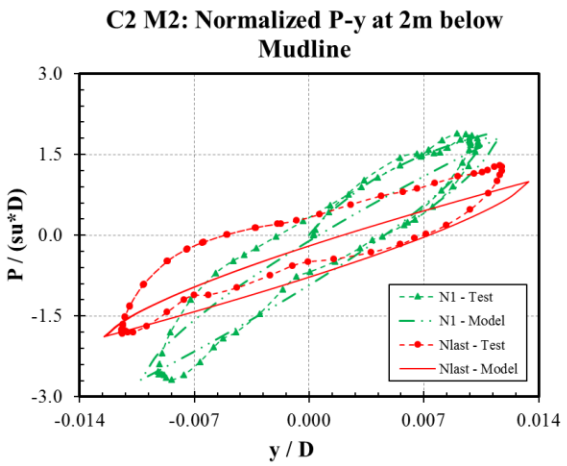


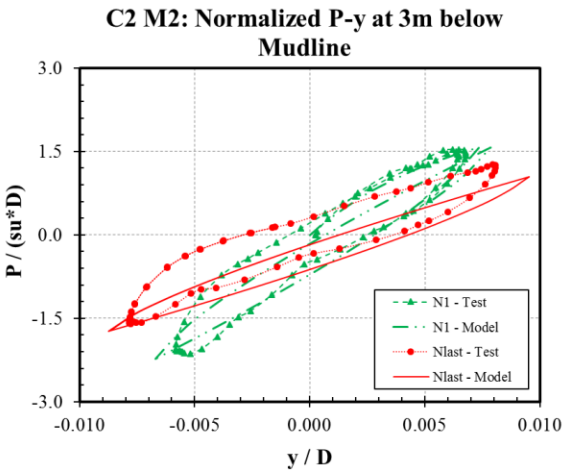


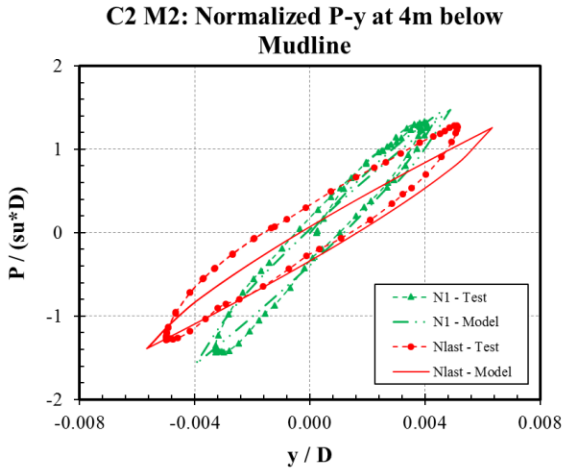


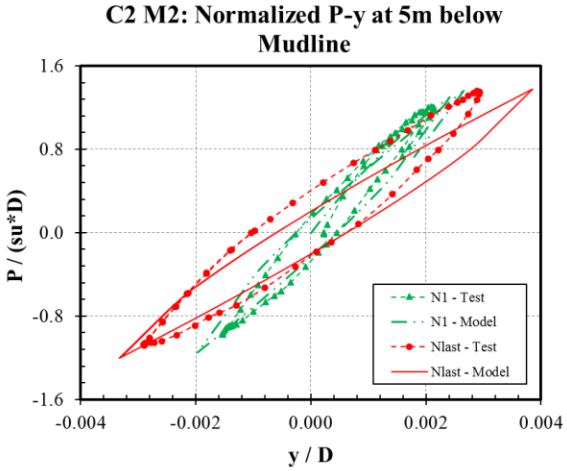

*Test 2 (Motion 3)*

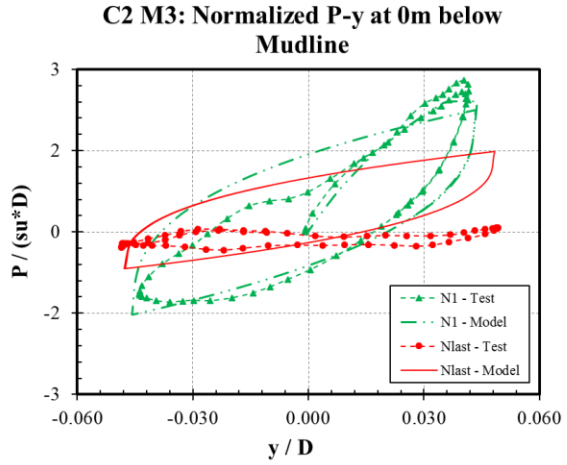


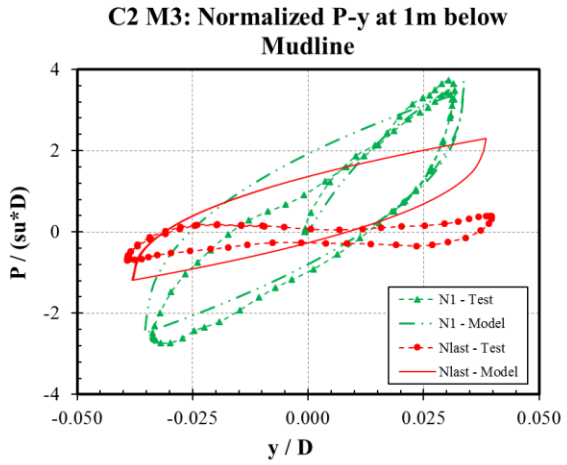


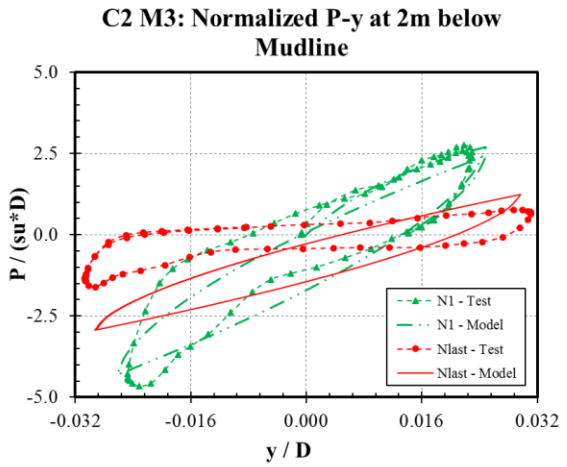


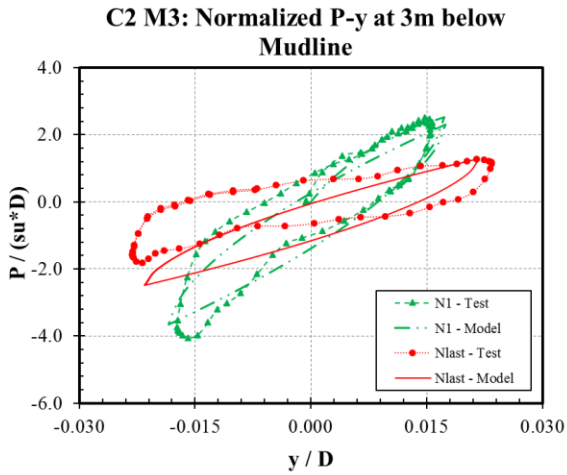


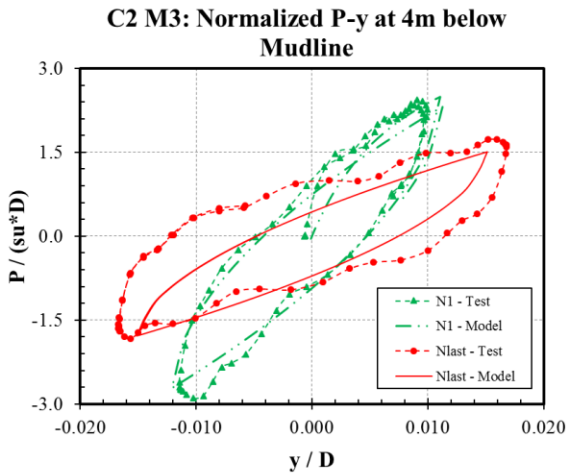


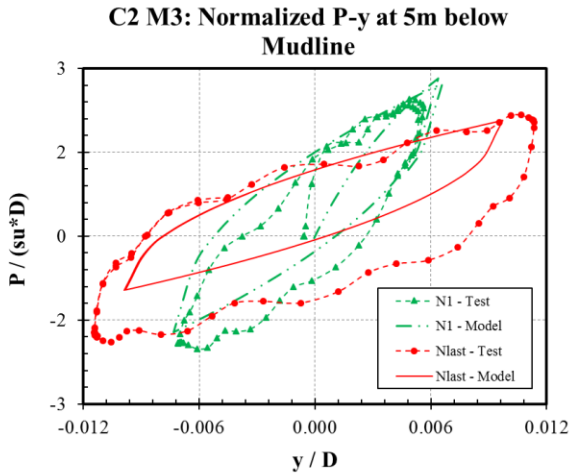

*Test 3 (Motion 1)*

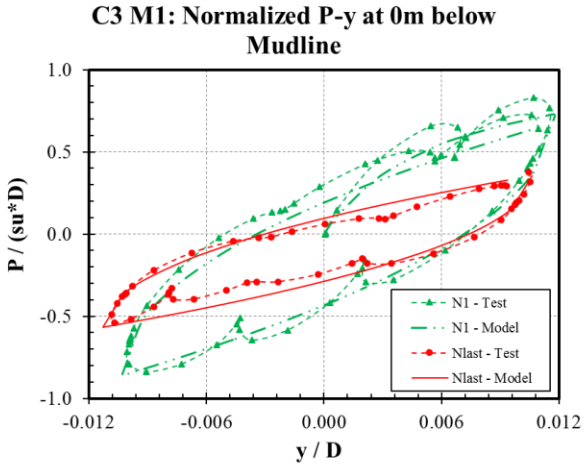


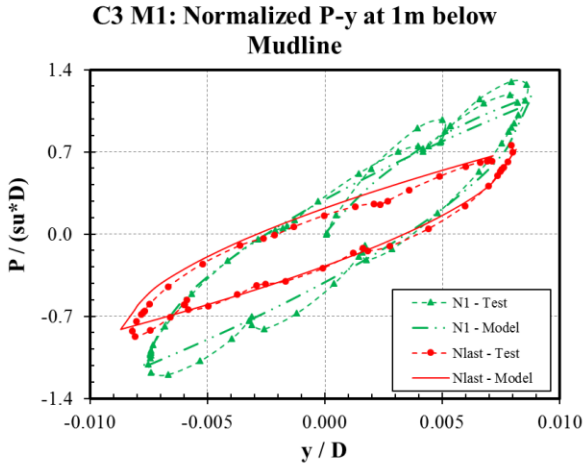


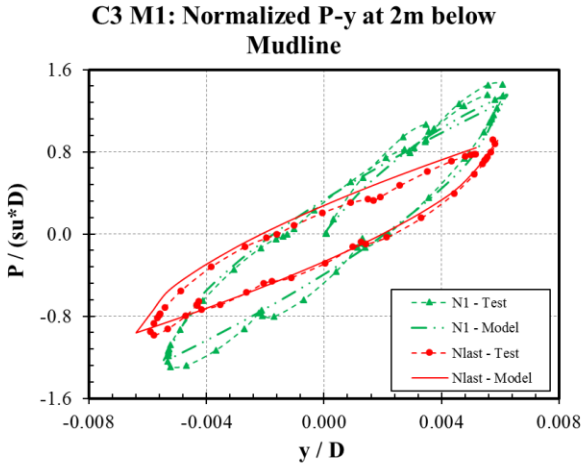


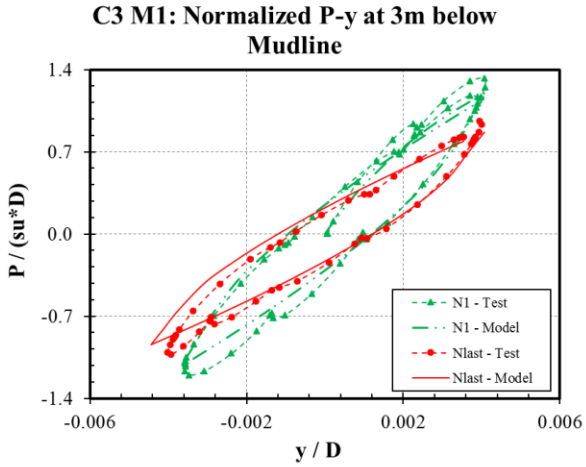


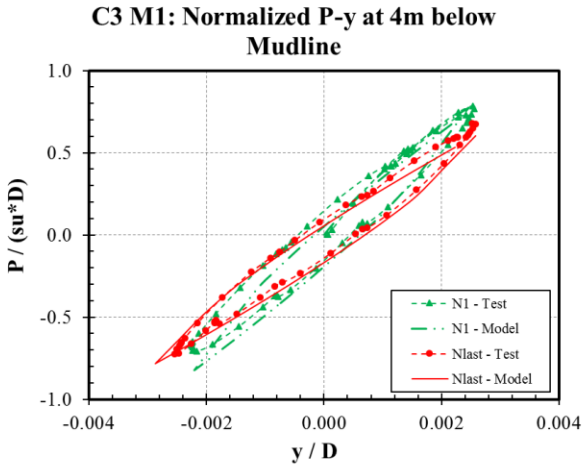


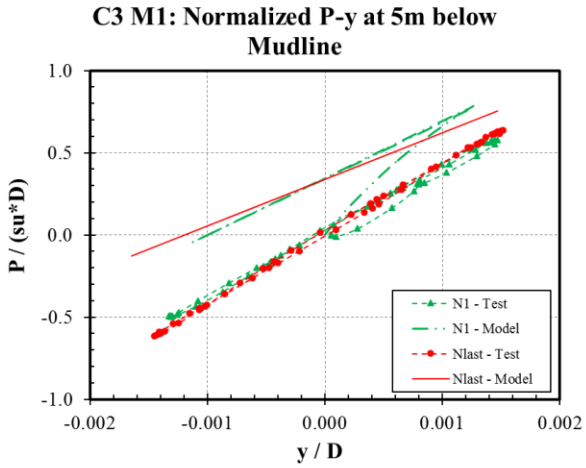

*Test 3 (Motion 2)*

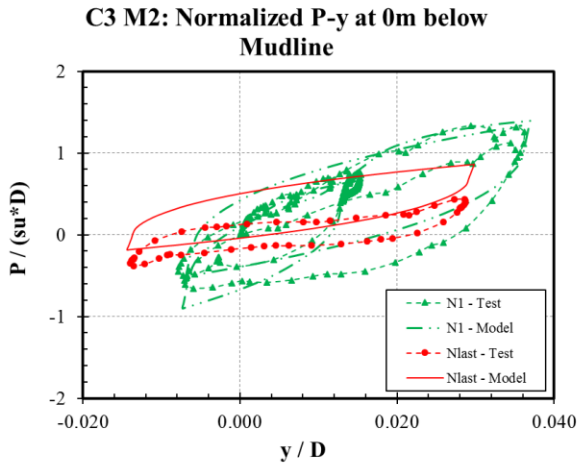


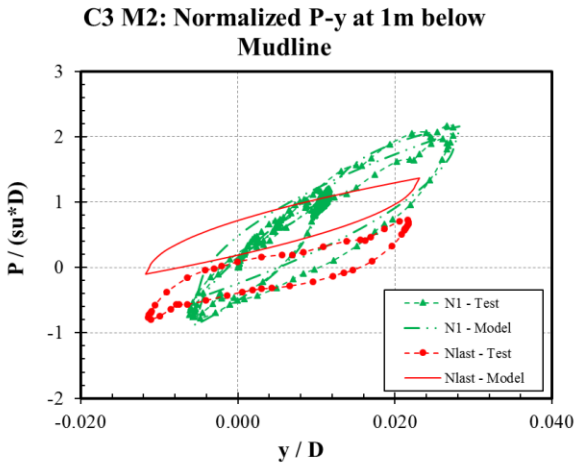


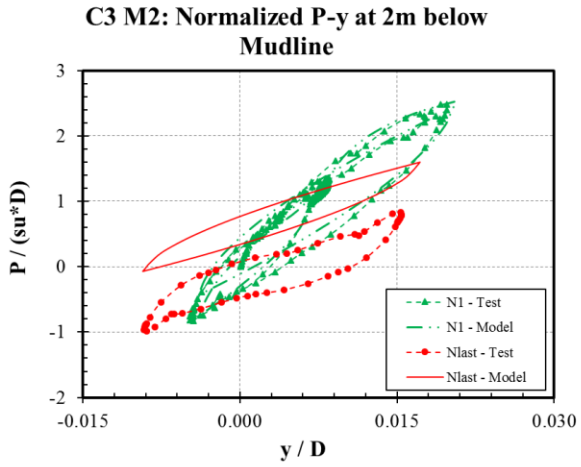


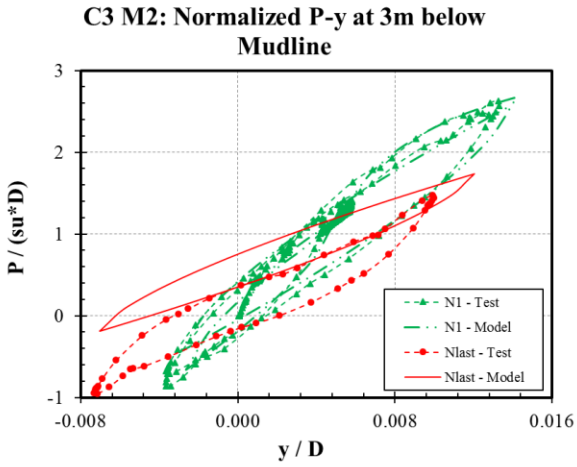


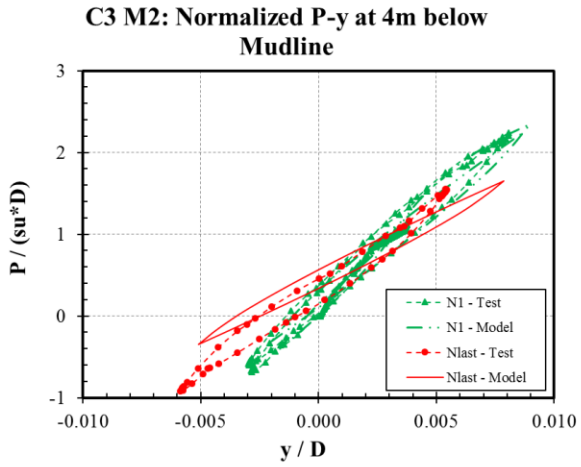


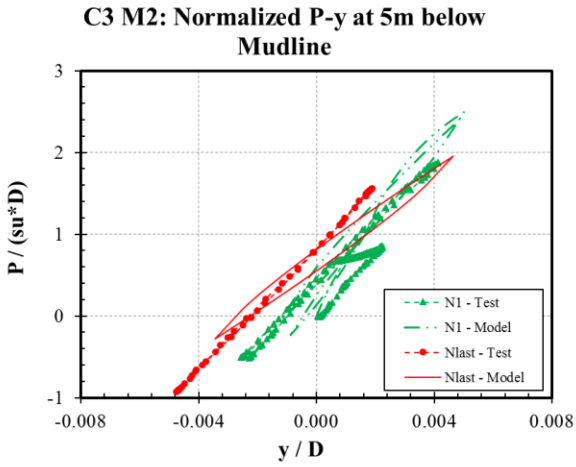

*Test 3 (Motion 3)*

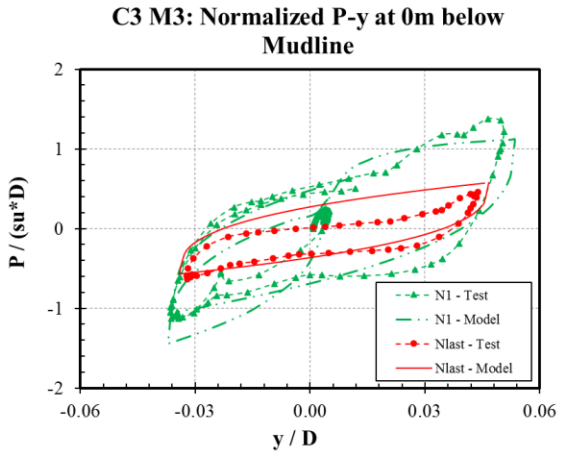


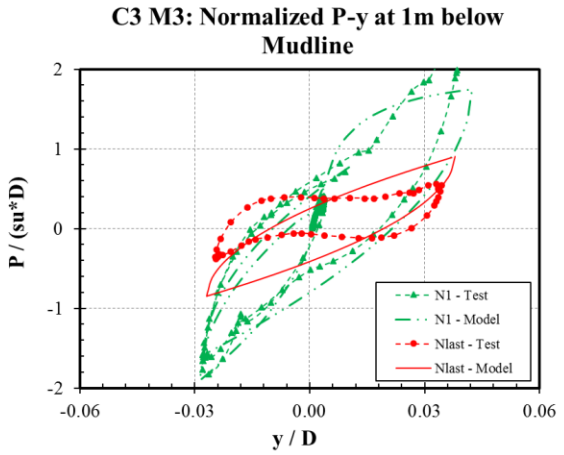


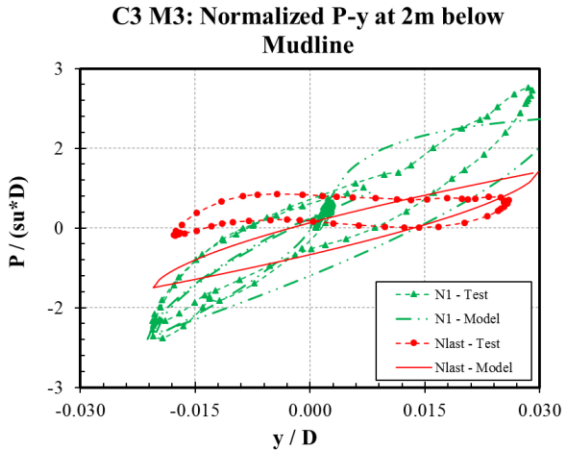


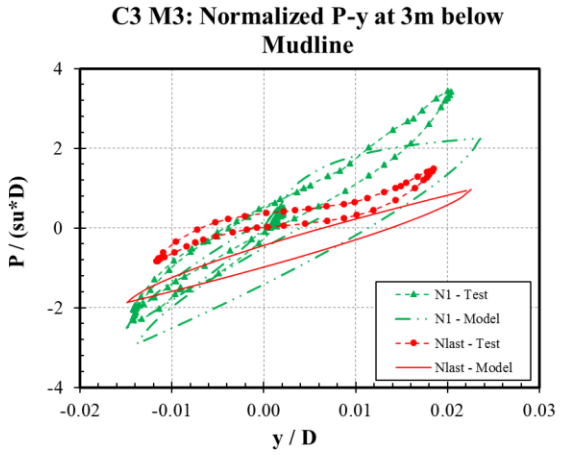


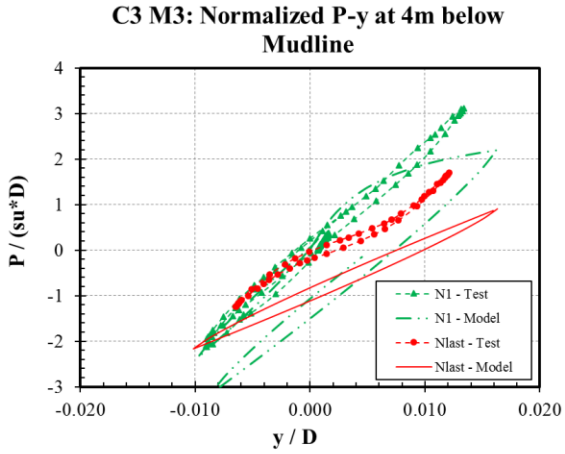


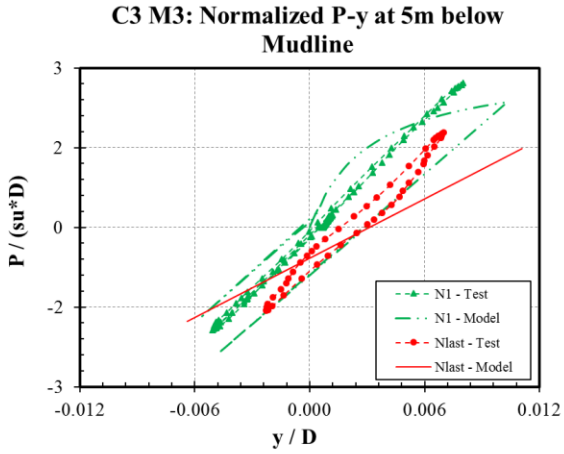

# APPENDIX E

## Bending Moment Profile Results for Soft Clay Soil

*Test 2 (Motion 2 and Motion 3)*

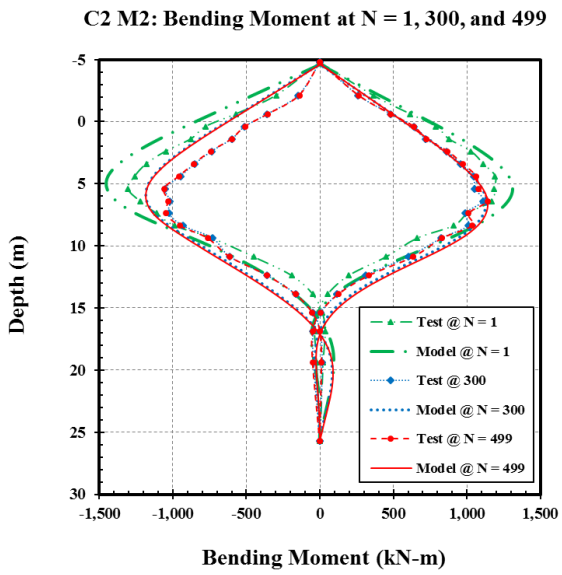


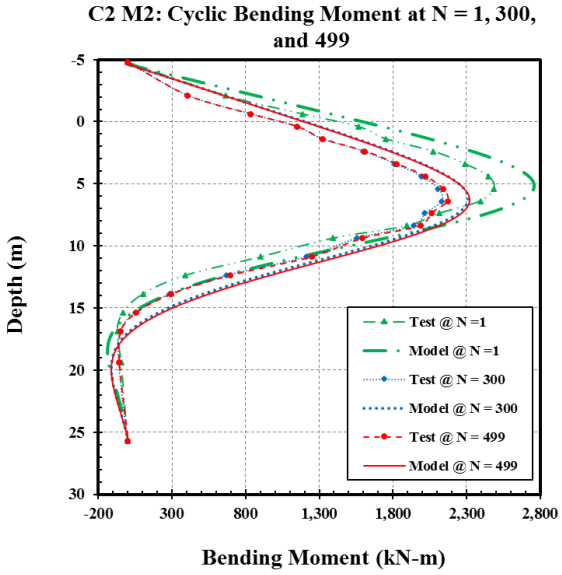


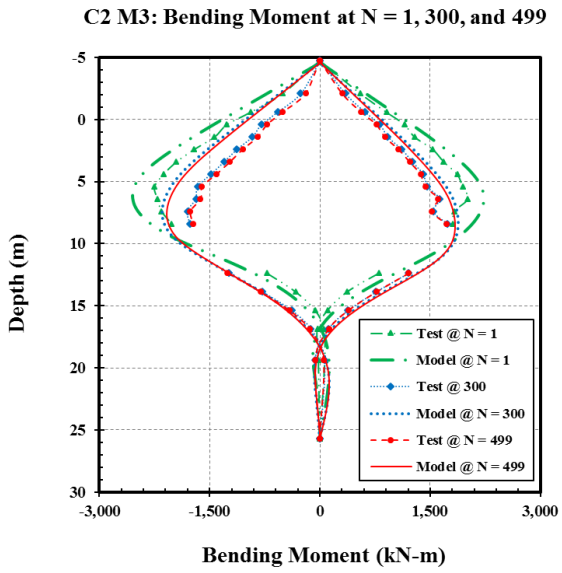


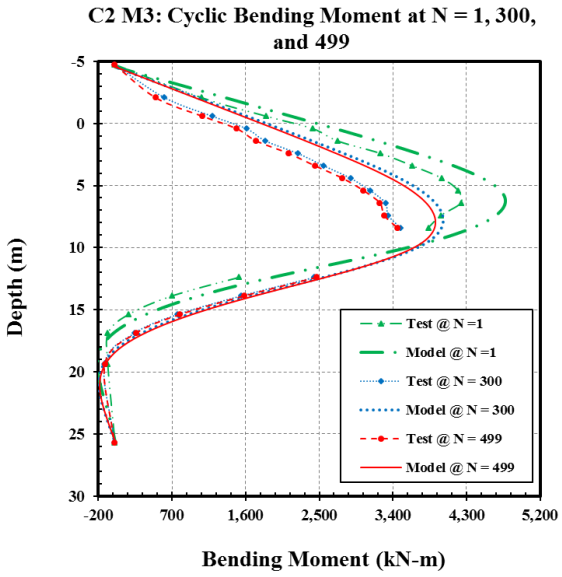

*Test 3 (Motion 1, Motion 2, and Motion 3)*

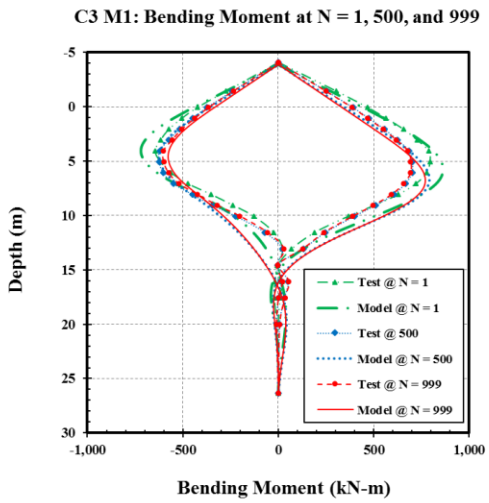


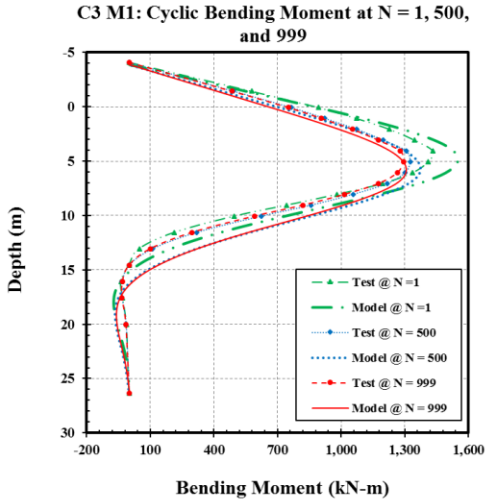


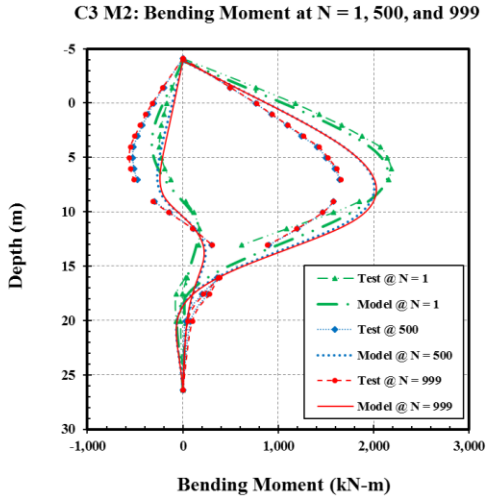


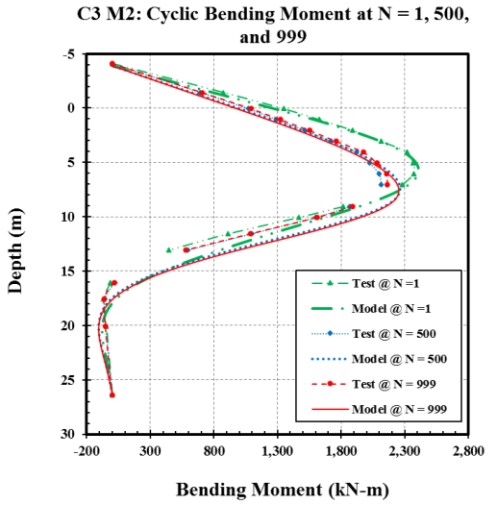


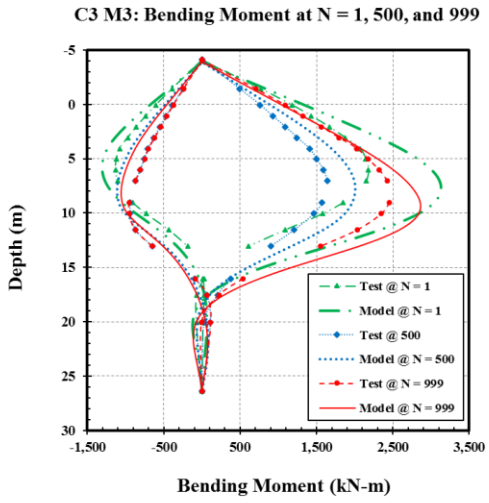


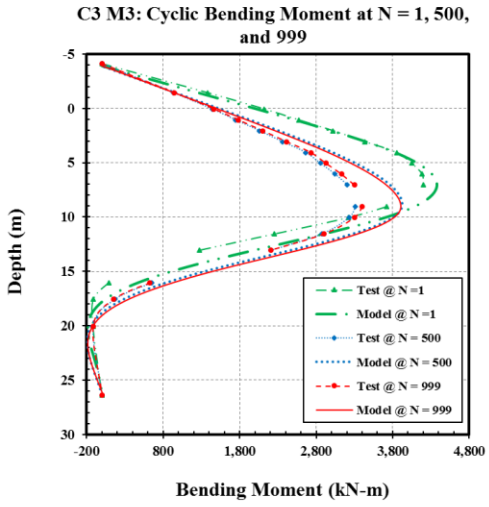

Bending Moment Profile Results for Stiff Clay Soil

*Test 2 (Motion 2 and Motion 3)*

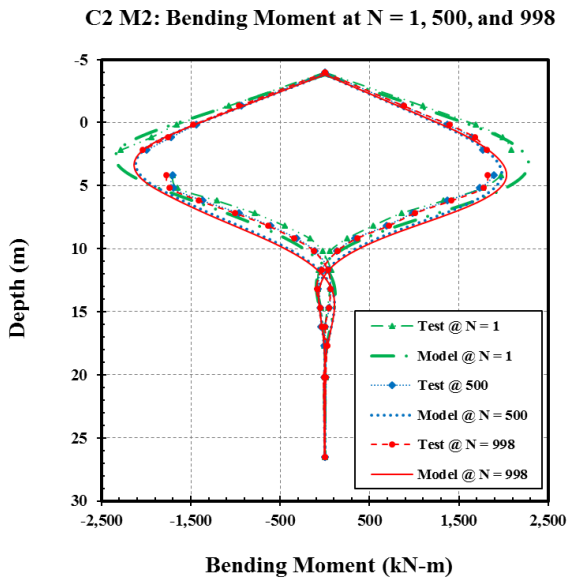


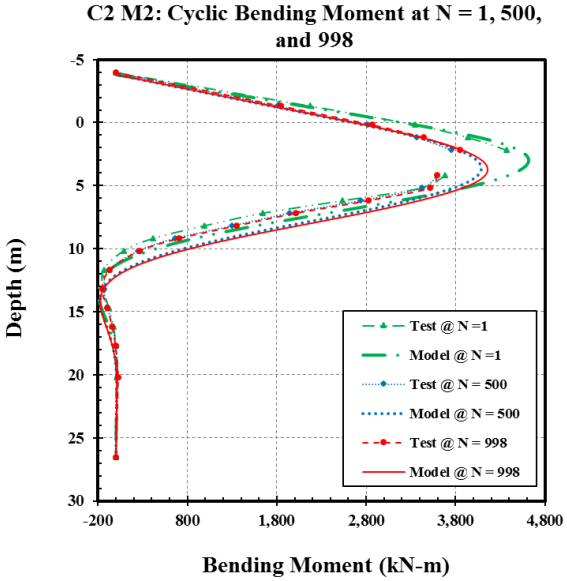


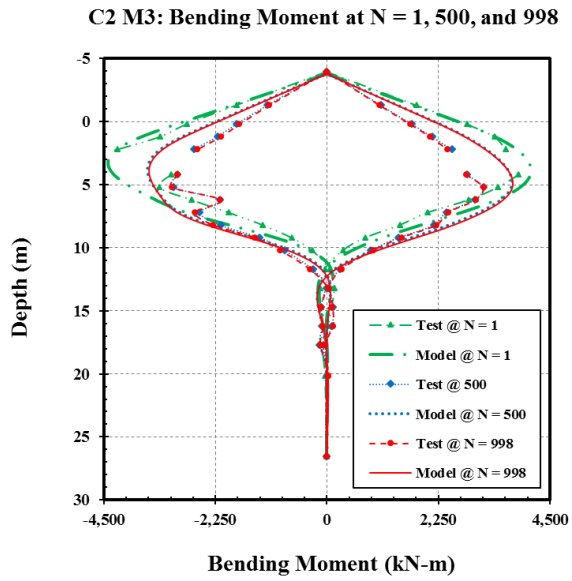


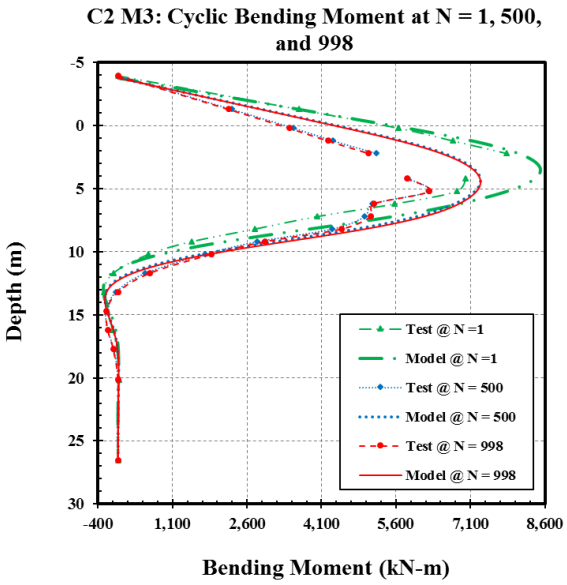

*Test 3 (Motion 1, Motion 2, and Motion 3)*